Development and study of high power tapered geometry superluminescent diodes

Yunus, Sharina

Award date:
2002

Awarding institution:
University of Bath

Development and Study of High Power Tapered Geometry Superluminescent Diodes

Submitted by

Sharina Yunus

For the degree of Doctor of Philosophy

of the University of Bath

2002

Copyright

Sharina Yunus

ProQuest LLC
789 East Eisenhower Parkway
P.O. Box 1346
Ann Arbor, MI 48106-1346

Summary

This thesis describes the development and study of high power tapered superluminescent diodes (TSLDs). A computationally efficient model for parallel stripe SLDs (PSLDs) is described and used to arrive at some of the design considerations for high power SLD design. Simulation results from the model show, that the key requirement to obtaining high powers from SLDs is low facet reflectivities (front and back). Hence a novel feature such as the two-dimensional etched deflector placed in the absorbing region and anti-reflection (A-R) coating on the front facet, is incorporated in the new TSLD structure. Experimental results show that a TSLDs with this combination yielded over 500mW quasi CW of output power. In addition, the effect of different taper flare angles on the angular intensity distribution is investigated. The measured output power from parallel stripe SLDs and taper SLDs are also compared demonstrating the superior efficiency of the taper SLDs especially at high levels of pumping.

Alternative method to reducing the front facet reflectivity, i.e. other than A-R coating, is also investigated. In this research the method of inclining the taper contact at an angle with respect to the normal of the facet is adopted due to its simple fabrication procedure. Experimental results show that output powers from angled contact SLDs (ATSLDs) is comparable to a similar TSLD with a single layer of A-R coating on the front facet. However, initial experimental result show that angled contact devices produce asymmetric near-field profiles. The ray model developed for ATSLDs demonstrates that this is the discriminating effect of the gain and the use of small numerical lens when measuring the near-field profiles of such devices. Simulation results from the model predict the trend of the near-field profiles quite well.

A computationally efficient model based on the ray analysis for parallel stripe, tapered and angled tapered SLDs, which incorporates the lateral and longitudinal variation of carriers is described and used to predict the near and far-field intensity distribution of these devices. The near-field and far-field profiles of PSLDs, TSLDs and ATSLDs measured at low and moderate current densities are shown to match quite well with those predicted by the model.

Contents

Chapter 3 Parallel Stripe Superluminescent Diodes

Chapter 4 Tapered Superluminescent Diodes

Chapter 7 Conclusions and Further Work

Appendix

List of Figures

Glossary

α_0	Gain constant
η	Effective refractive index of (vertical) waveguide mode
λ	Wavelength of light in free space
μ_p	Hole mobility
υ	Velocity of light in media
ρ_c	Sheet resistivity of cladding layer
τ_{sp}	Spontaneous emission recombination lifetime
Γ_v	Confinement factor of vertical waveguide mode
c	Speed of light in free space
d	Thickness of active layer
d_c	Thickness of the remaining cladding layer after etching
g	Gain of material
q	Electron charge
t	time
x	Dimension in Cartesian Coordinate System
y	"
z	"
B_r	Bimolecular recombination constant
D	Diffusion coefficient
E	Electric field vector
H	Magnetic field vector
I	Current
J	Current density
L	Length of device
L_c	Length of contact
N	Carrier density
N_c	Doping density of cladding layer
N_0	Doping density of active layer

P	Photon density of forward traveling photons
Q	Photon density of reverse traveling photons
R	Facet reflectivity
R_{L_c}	Front facet reflectivity
R_0	Back facet reflectivity
V	Volume

Chapter 1
Introduction

1.1 Introduction

In recent years superluminescent diodes (SLDs) have attracted wide attention as light sources for various applications. Unlike the laser diode, the superluminescent diode is an incoherent source and there are many applications in which an incoherent source is desirable. Some of the examples include short-haul optical fibre communication [1], fibre optic gyroscopes [2] and optical coherence tomography for medical tissue imaging [3]. In the examples mentioned above, Rayleigh backscattering noise which is caused by the interference between the signal light and the reflected light is a serious problem when a coherent light source such as a laser diode is used. Conversely, SLD's are suitable for these applications because such noise can be remarkably reduced due to the broad emission spectrum of the SLD.

The SLDs reported to date can be divided into two types: GaAs based SLDs with operating wavelength between 0.8μm – 0.98μm, [4], [5] and InP based SLDs operating around 1.3μm, [6], [7]. In general, the former have been developed for high power applications while the latter as light sources in systems using low-loss optical fibre communications. In optical applications it is desirable to increase the output power from the device. The past ten years especially has seen great demand for high power SLDs, in particular edge-emitting-superluminescent diodes (EE-SLDs). However, many of the conventional EE-SLDs yield low output powers. The difficulty in obtaining high output powers from EE-SLDs is that lasing often appears at high pumping conditions. The key requirement to obtaining high output powers from SLDs are low facet reflectivities. Various methods have been used by many research groups to achieve the desired low facet reflectivities. However, most

have used complex and often expensive fabrication techniques. It is the aim of this research to develop high output power EE-SLDs that are simple and cheap to fabricate.

A description of an EE-SLD is given in section 1.2 which highlights some of the difficulties in obtaining high power SLD operation. This is followed by a literature review of some of the various methods that have been used to obtain low facet reflectivities, which is discussed in section 1.3. In addition, literature review on tapered geometry devices is given in section 1.4, since devices with this geometric shape have been shown to yield high output powers. Finally a layout of the thesis is given in section 1.5.

1.2 Superluminescent Diodes

A typical structure of an EE-SLD is shown in Figure 1.1. The EE-SLD structure is similar to that of a stripe contact laser diode except that the stripe contact does not reach the full length of the diode chip, which effectively creates an unpumped absorbing region at the back. In a SLD the injected current is increased until amplification of spontaneous emission occurs (i.e. the initial step before lasing), but because there is high loss at one end of the device, no optical feedback takes place and lasing is suppressed. At low currents, the device operates as an Edge Emitting-LED (EE-LED). However at high currents the output power of the device increases dramatically, and the spectral width narrows considerably due to the onset of the optical gain in the media. Typical linewidths for SLDs are in the range of 30nm - 40nm in contrast to 60nm - 90nm spectral width usually associated with other conventional EE-LEDs. In general the characteristics of SLDs lie midway between that of a laser diode and an EE-LED. Some of the advantages of SLDs are less coherence and less susceptibility to thermal effects than laser diode.

Although the incoherent optical power output from SLDs can approach that of the coherent output from injection lasers, the required current density is substantially

higher, by around a factor of three times, necessitating high drive currents due to long device lengths. If the drive current is high enough the absorbing region can be optically pumped to transparency such that light in the absorbing region are not sufficiently absorbed but propagate through creating an optical feedback path. Therefore a slight increase in injection current (increase in gain) will cause the device to reach lasing threshold, which limits the available output power form the SLD mode operation.

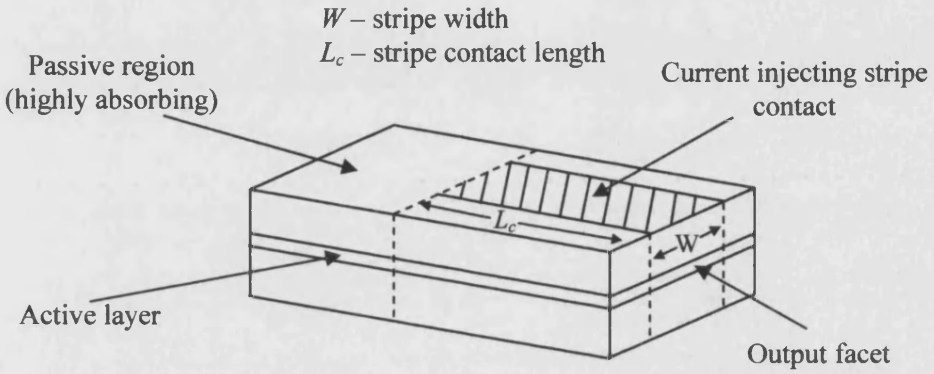

Figure 1.1: Illustrates a typical structure of an edge-emitting superluminescent diode (SLD).

In general to achieve high power SLD operation, the (effective) facet reflectivities (front and back) must be very small to suppress lasing at high injection currents and maintain low spectral modulation. Only by suppressing lasing can the optical gain be increased sufficiently to obtain very large amplification of spontaneous emission (ASE). It has been reported in [8] that facet reflectivities as low as 2.5×10^{-6} are needed for high power SLD operation. Although high quality anti-reflection coating as low as 2.5×10^{-4} [9], have been achieved it is however expensive and not routinely available.

Apart from low facet reflectivities there is also the need to overcome the limitation of optical (gain) saturation and catastrophic optical damage (COD) due to high optical densities at the facet. The saturation and COD problems has most commonly been resolved by using broad area devices but it is noted that the largest output powers have been achieved with tapered geometry devices [10], [11]. It was reported in [10], that tapered geometry devices have high power saturation.

1.3 Various Methods of Reducing Facet Reflectivities

1.3.1 SLD with Anti-Reflection Coating

Low facet reflectivities can be achieved by applying anti-reflection (A-R) coating on one or both facets of the SLD. A superluminescent diode made from essentially a laser structure has been reported [12]. The device, consist of a parallel ridge-waveguide region, which is index guided, with one facet A-R coated and a high reflectivity mirror at the other end. The disadvantage of this device is that very high quality A-R coatings ($R \sim 10^{-6}$) are needed to inhibit lasing. Furthermore, even with high quality A-R coating substantial modulation depth in the spectra at high currents was observed with this device.

1.3.2 SLD with Antireflective Window Structure

A parallel stripe SLD with an antireflective window structure has also been reported, [13]. This device incorporates a transparent window region at the rear side of the device as shown in Figure 1.2. The purpose of the antireflective window structure is to destroy optical feedback and prevent the device from reaching lasing threshold. Here the backward travelling light emitted from the edge of the active layer diverges in the transparent window region such that only a small percentage is reflected back from the A-R coated rear facet, into the active layer. 50mW at 450mA of input current has been reported for this device. The disadvantage of this device is that it requires complex fabrication procedure, which includes two epitaxial growth stages followed by MOCVD growth to incorporate the transparent window at the rear of the device.

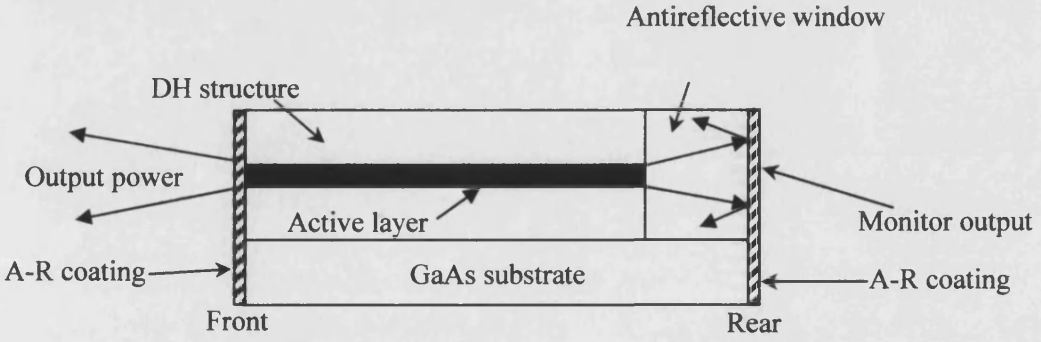

Figure 1.2: Side view of a parallel stripe SLD with an antireflective window structure.

1.3.3 SLDs with Absorbing Region

In these devices an absorbing region is integrated near the rear facet, which absorbs light propagating away from the output end and thus suppressing lasing oscillation. A visible SLD (λ = 670nm) that employs a tapered grounded absorber has been reported, [14]. This device displayed spectral modulation less than 10%.

More recently another device operating at 1.3μm has been reported to use a tapered grounded absorber [15]. In this device part of the tapered absorber region is inclined from the active-stripe axis, illustrated in Figure 1.3. It was mentioned earlier that at high levels of pumping the absorbing region can be optically pumped to transparency, which consequently creates an optical feedback path, making lasing a distinct possibility. Therefore, the inclination of part of the absorber region is employed to prevent light from coupling back into the active region.

In summary these devices [14], [15], delivered respectable amounts of output powers. However, much like the SLDs discussed earlier these devices required complex fabrication procedures to incorporate the tapered absorbing region.

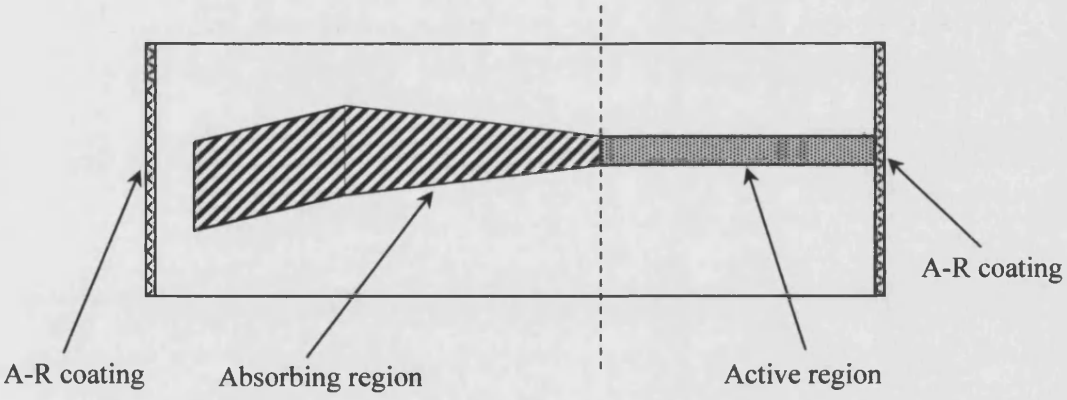

Figure 1.3: Top view of a SLD with a tapered grounded absorber with part of the taper region inclined at an angle.

1.3.4 SLDs with Angled Stripe Contacts

Apart from the need to reduce reflected light from the rear facet from re-entering the active layer, there is also the need to reduce the reflected light from the front facet. This is easily achieved by inclining the stripe contact at an angle θ with respect to the normal of the facet as shown in Figure 1.4. Greater than 15mW CW from a SLD inclined at an angle $\theta = 5°$ has been reported with negligible spectral modulation [10]. A similar device, a real refractive-index-guided SLD with $\theta = 5°$ demonstrated 100mW CW at 300mA with less than 3% spectral modulation [17]. However in both devices [10], [17], A-R coating on both facets were still needed to further reduce reflection and increase the output power.

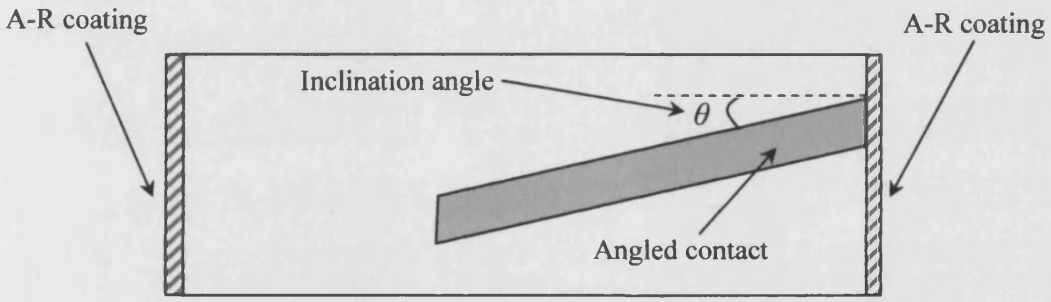

Figure 1.4: Top view of SLD inclined at an angle θ with respect to the normal of the facet.

1.4 High Power Amplifiers and SLDs

1.4.1 Broad Area Structures

The obvious and easiest method of increasing the overall output power is simply to increase the active area. Broad area semiconductor amplifiers yielding output powers as high as 3.3W CW at 7.0A when injected with a high power (400mW) Ti:saphire master oscillator has been reported [18]. However, to inhibit lasing, both facets were A-R coated ($R \sim 10^{-3}$). The disadvantage of this device is that, two external lenses are needed to couple light from the Ti:sapphire laser into the broad area amplifier. Hence, device operation is very easily affected by feedback from external reflections, making it prone to lasing.

1.4.2 Taper Structures

Tapered devices are devices that have a region (etched rib) where the width changes along the length of the device. Devices with this type of structure have an advantage over other high power sources. Firstly, tapered devices can be easily fabricated because fabrication of the etched rib is simple and a well established process that does not require any regrowth or other complex steps. Secondly the increase in area of a tapered device increases the saturation output power compared to a narrow device simply by increasing the active volume at the facet. Also, at higher output powers this increase in area decreases the optical power density at the facet thus reducing the effect of COD.

Taper geometry devices have demonstrated high powers, when incorporated into a wide variety of device configurations such as tapered amplifiers.

- ***Taper Amplifiers***

Research on tapered amplifiers has been carried out by a number of groups [10], [19]. These devices consist of a tapered gain region, which may or may not be index guided. Output powers as high as 4.5W CW at 7.0A when injected with a high power (150 mW) Ti: sapphire master oscillator has been reported [19]. Although the broad area amplifier [18], produced slightly higher output powers than the tapered amplifier for the same current density value, the former however required 400mW of injected power from the Ti:sapphire master oscillator. Similar to the broad area amplifier, A-R coatings ($R \sim 10^{-3}$) are required on both facets to prevent the device from reaching the lasing threshold.

A tapered amplifier with a monolithically integrated focussing lens has also been reported [9], illustrated in Figure 1.5. To reduce front facet reflections and avoid the use of A-R coatings the device was tilted by 7° with respect to the axis of the taper. Output powers greater than 1W CW has been demonstrated, and at powers up to 0.5W the output beam was focussed down to a spot of size 8μm x 3μm.

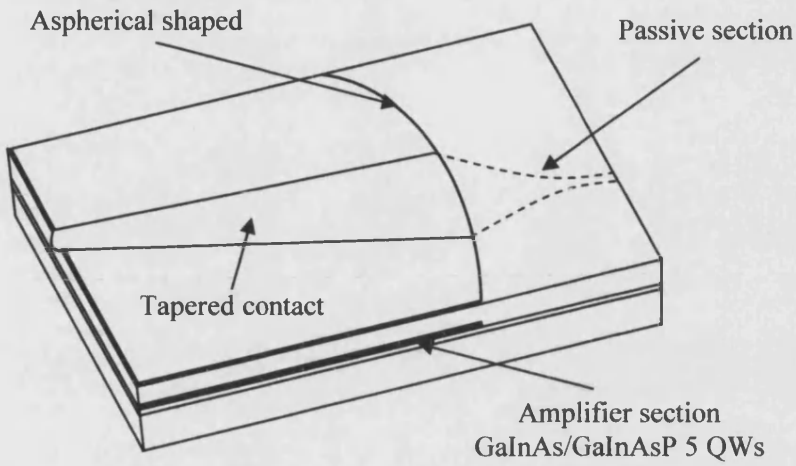

Figure 1.5: Schematic of tapered amplifier with an integrated focusing lens inclined at 7° with respect to the axis of the taper.

However, the disadvantage with this device, [10], is that it requires two epitaxial growth stages in order to integrate a passive output waveguide in which the beam is focussed. Furthermore, accurate control during crystal growth is also required to ensure that the focal point coincides with the output facet so that a circular beam is obtained.

- ***Taper Amplifiers seeded with EE- SLDs***

A tapered amplifier when seeded with a low power parallel EE-SLD has also been reported to produce output powers up to 470mW CW [11]. The disadvantage of this device is that the coupling efficiency of the SLD power into the amplifier is only about 16%. Another disadvantage is that the spectral peak of the amplifier does not coincide with the spectral peak of the SLD. Hence, it would be impossible to obtain maximum optical gain of the amplifier.

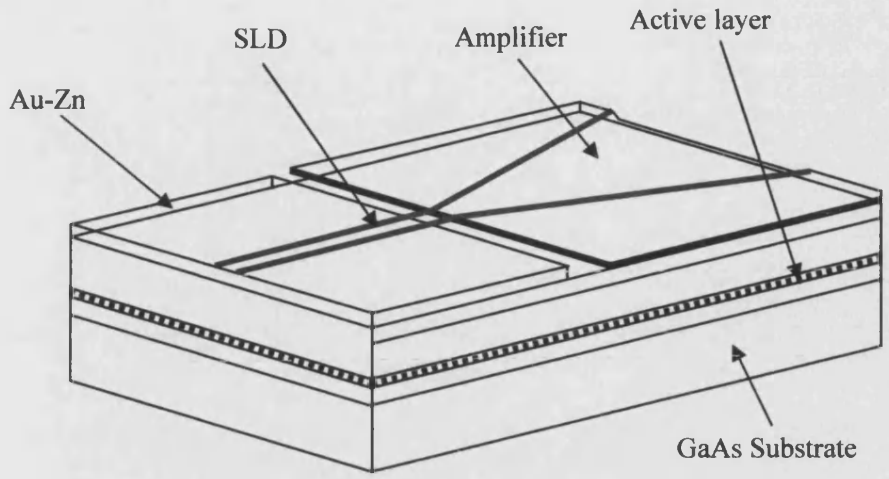

Figure 1.6: Schematic of the monolithic integration of a SLD with a tapered power amplifier.

More recently monolithic integration of a SLD with a tapered power amplifier has been demonstrated [20], shown in Figure 1.6. A 15μm wide isolating stripe, generated by "lift-off" of Au-Zn, separated contacts to the two devices so that injection currents to the devices were independent. The coupling efficiency from the SLD to the amplifier was estimated to be about 100%. Output powers over 80mW have been achieved at 1.5A of injection current for the amplifier and 150mA for the SLD. However, when the SLD is pumped further the device reached the lasing threshold since a lasing peak was observed in the spectrum. The disadvantage with this structure is that it requires the device to be mounted substrate side down to the heatsink which is not the standard procedure for good thermal contact and may affect the temperature of the device.

1.5 Thesis Layout

This thesis describes the development and study of high output power tapered geometry superluminescent diode (TSLDs). All the SLDs fabricated throughout the research work are edge-emitting and are of the rib structure type. In Chapter 2 a description of rib structure devices together with a discussion of the factors that influence the distribution of carrier in such a device are given. The distribution of carriers is of particular interest since one of the aims of the research work is to develop a theoretical model of tapered superluminescent diodes. In order to obtain a realistic model of such a device, the variation of the carrier distribution should be included, since in this type of device the distribution of carriers varies both laterally and longitudinally. In addition the rate equations which are used to model the TSLDs are introduced in Chapter 2.

Chapter 3 contains a theoretical study of parallel stripe SLDs. The problems encountered due to carrier depletion (hole-burning) at high levels of pumping, which limits the available output power from SLDs are discussed. Simulation results showing the effects of anti-reflection coating on the front facet and device contact length variation have on the electrical efficiency of the devices are presented. The significance of these results in terms of high power SLD design is also discussed.

In Chapter 4, a tapered superluminescent diode incorporating a novel two dimensional etched deflector for high power SLD operation is described. Experimental results of the characterisation of TSLDs are contained in this chapter. The effect of the two dimensional etched deflector, anti-reflection coating on the front facet and different taper flare angles on the performance of the devices are also investigated. Finally, the electrical efficiency of parallel stripe SLDs and TSLDs are presented and compared.

The possibilities of reducing the effective facet reflectivities and obtaining high output powers from TSLDs, by inclining the tapered contact at angle with respect to the normal of the facet are examined in Chapter 5. The experimental results of

angled TSLDs (ATSLDs) inclined at different angles are presented and discussed. This chapter also describes the asymmetry of the near-field intensity distribution obtained from ATSLDs and how they can be explained by a simple ray analysis. To test the validity of the ray analysis two different experiments were performed on the ATSLDs. The theoretical and experimental results are compared and presented.

In chapter 6, a comprehensive ray model, which includes the lateral and longitudinal distribution of carriers are described. The comprehensive ray model has been develop to predict the spatial characteristics of parallel, taper and angled taper SLDs. Simulations results of these devices are presented and compared with experimental results.

Finally, some conclusions to be drawn from the research work are presented in Chapter 7 along with suggestions for future work.

References

[1] *P. W. Shumate, J. L. Gimlett, M. Stern, M. B. Romeiser, and N. K. Cheung,* **'Transmission of 140 Mbits/s Signals over Single-Mode Fiber Using Surface- and edge-emitting 1.3μm LED's'**, Electronic Letters, Vol. 21, pp. 522 – 524, 1985.

[2] *W. K. Burns, C. L. Chen, and R. P. Moeller,* **'Fibre Optic Gyroscopics with Broad-Band Sources'**, Journal of Lightwave Technology, Vol. LT-1, pp. 98 – 105, 1983.

[3] *D. Huang,* **'Optical Coherence Tomography'**, Science, Vol. 254, pp. 1178 – 1181, 1987.

[4] *A. T. Semenov, V. R. Shidlovski, and S. A. Safin,* **'Wide Spectrum Single Quantum Well Superluminescent Diodes at 0.8 μm with Bent Optical Waveguide'**, Electronic Letters, Vol. 29, pp. 854 – 856, 1993.

[5] *C. F. Lin and C. S. Juang,* **'Superluminescent Diodes with Bent Waveguide'**, IEEE Photonic Technology Letters, Vol. 8, pp. 206 – 208, 1996.

[6] *N. S. Kwong, N. Bar-Chaim, and T. Chen T,* **'High-Power 1.3μm Superluminescent Diode'**, Applied Physics Letters, Vol. 54, pp. 298 – 300, 1989.

[7] *S. Kondo, H. Yasaka, Y. Noguchi, K. Magari, M. Sugo, and O. Mikami,* **'Very Wide Spectrum Multi Quantum Well Superluminescent Diode at 1.5μm'**, Electronic Letters, Vol. 28, pp. 132 – 133, 1992.

[8] *I. P. Kaminow, G. Eisenstein, L. W. Stulz, A. G. Dentai.,* **'Lateral Confinement InGaAsP Superluminescent Diode at 1.3 μm'**, IEEE Journal of Quantum Electronics, Vol. QE-19, No 1, pp. 78-82, 1993.

[9] *Gerard A. Alphonse, D. B. Gilbert, M. G. Harvey, and M. Ettenberg,* **'High Power Superluminescent Diodes'**, IEEE Journal of Quantum Electronics, Vol. QE-24, No 12, pp. 2454 – 2457, 1988.

[10] *I. Ladany, P. J. Zanzucchi, J. T. Andrews, J. Kane, E. DePiano,* **'Scandium Oxide Antireflection Coatings for Superluminescent LEDs'**, Applied Optics, Vol. 25, p. 472, 1986.

[11] *F. Koyama, K. Y. Liou, A. G. Dentai, T. Tanbun-ek, and C. A. Burrus,* **'Multiple-Quantum-Well GaInAs/GaInAsP Tapered Broad-Area Amplifiers with Monolithically Integrated Waveguide Lens for High-Power Applications'**, IEEE Photonics Technology Letters, Vol. 5, No. 8, pp. 916 – 919, 1993.

[12] *L. Goldberg and D. Mehuys,* **'High Power Superluminescent Diode Source'**, Electronics Letters, Vol. 30, No. 20, pp. 1682 – 1684, 1994.

[13] *I. P. Kaminow, G. Eisenstein, L. W. Stulz, and A. G. Dentai,* **'Lateral Confinement InGaAsP Superluminescent Diode at 1.3μm'**, IEEE Journal of Quantum Electronics, Vol. QE-19, No 1, pp. 78 – 81, 1983.

[14] *Kazuki Tateoka, Hiroki Naito, M. Yuri, M. Kume, K. Hamada, H. Shimizu, M. Kazumura, and I. Teramoto,* **'A high-Power GaAlAs Superluminescent Diode with an Antireflective Window Structure'**, IEEE Journal of Quantum Electronics, Vol. QE-27, No 6, pp. 1568 – 1573, 1991.

[15] *A. T. Semenov, V. R. Shidlovski, S. A. Safin, V. P. Konyaev and M. V. Zverkov,* **'Superluminescent Diodes for Visible (670 nm) Spectral Range Based on AlGaInP/GaInP Heterostructures with Tapered Grounded Absorber'**, Electronic Letters, Vol. 29 No. 6, pp. 530 – 532, 1993.

[16] *H. Okamoto, M. Wada, Y. Sakai. T. Hirono, Y. Kawaguchi, Y. Kondo, Y. Kadota, K. Kishi, and Y. Itaya,* **'A Narrow Beam 1.3-μm-Super Luminescent Diode Integrated with a Spot-Size Converter and a New Type Rear Absorbing Region'**, Journal of Lightwave Technology, Vol. 16, No. 10, pp. 1881 – 1887, 1998.

[17] *T. Takayama, O. Imafuji, Y. Kouchi, M. Yuri, A. Yoshikawa, and K. Itoh,* **'100-mW High Power Angled-Stripe Superluminescent Diodes with a New Real Refractive-Index-Guided Self-Aligned Structure'**, IEEE Journal of Quantum Electronics, Vol. QE-32, No 11, pp. 1981 – 1996, 1996.

[18] *L. Goldberg, D. Mehuys and D. C. Hall,* **'3.3 CW Diffraction limited Broad Area Semiconductor Amplifier'**, Electronics Letters, Vol. 28, No. 12, pp. 1082 – 1084, 1992.

[19] *D. Mehuys, L. Goldberg, R. Waarts, and D. F. Welch,* **'4.5W CW, Near-Diffraction-Limited Tapered-Stripe Semiconductor Optical Amplifier'**, Electronics Letters, Vol. 29, No. 2, pp. 219 – 221, 1993.

[20] *Y. Liu, Kun Liu, J. Song, Y. Chang, B. Kang, J. Yin, G. Du,* **'1.3μm Integrated Superluminescent Light Source'**, Optical Materials, No. 14, pp. 235 – 238, 2000.

Chapter 2
Carrier Distribution in Semiconductor Devices

2.1 Introduction

In optical applications it is desirable to limit the vertical and horizontal spread of carriers and optical emission from semiconductor (s/c) devices like lasers and superluminescent diodes (SLDs). Significant improvement in optical confinement in the vertical direction has been achieved with the development of the double heterostructure material, shown in Figure 2.1. In this type of material the injected carriers are confined by the potential barriers that exist at the higher band-gap interface and the light is confined by the waveguide that is created by the higher refractive index of the lower band-gap layer (active layer), discussed in detail in section 2.2 of this chapter. Conversely, horizontal (lateral) confinement of carriers and optical emission is achieved by restricting the flow of current in this direction.

Various methods have been used to restrict the lateral flow of current, leading to a variety of s/c device structures. However one of the simplest semiconductor device structures to fabricate is the rib waveguide double heterostructure (DH) device, illustrated in Figure 2.1. The rib structure restricts the flow of current in the lateral direction and consequently the lateral distribution of carriers. In a device with no deliberate lateral waveguide it is the lateral distribution of carriers that determines the width of the optical distribution. All the SLDs presented in this thesis are of the rib structure type and have no deliberate lateral waveguide.

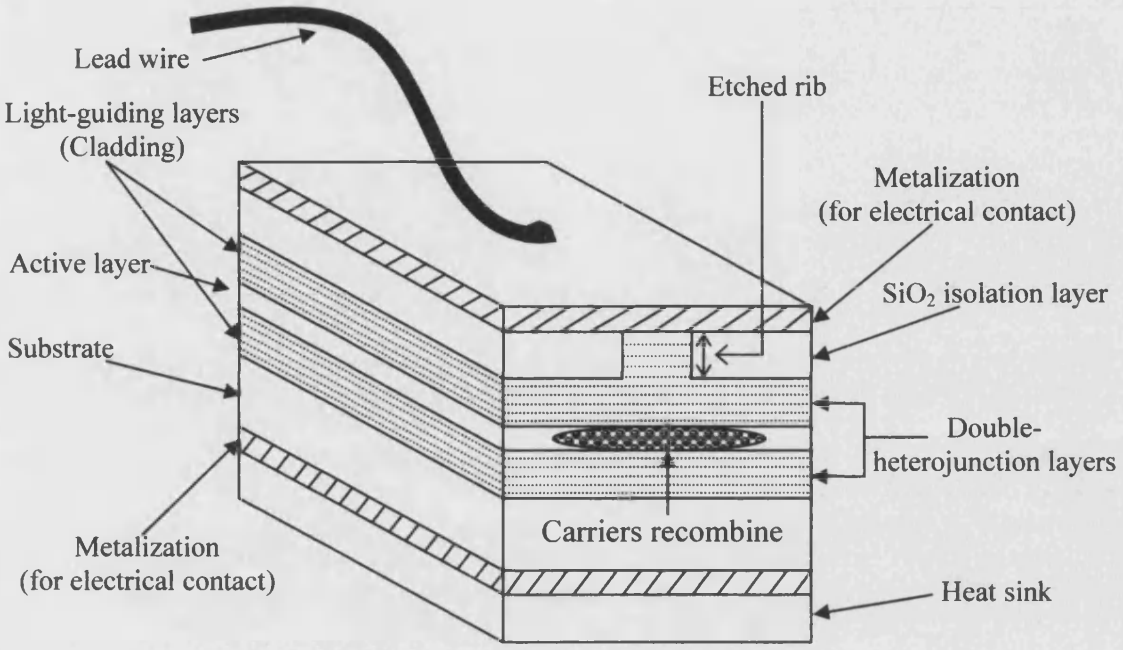

Figure 2.1: Schematic of a stripe ridge guide semiconductor device.

The distribution of carriers in s/c devices is of particular interest because one of the main aims of the research work is to develop a theoretical model for tapered geometry superluminescent diodes (TSLDs). As mentioned in Chapter 1, tapered geometry devices have rib width that changes along the length of the device. In this type of structure the lateral carrier density distribution profile changes as the rib width is narrowed. Hence, the operation and the output characteristics of these devices depend quite significantly on the distribution of carriers. Two processes determine the lateral distribution of carriers; the first is current spreading in the cladding layer and the second is carrier diffusion in the active layer [1]. Therefore, in order to obtain a reliable model of tapered geometry devices, parameters such as current spreading length and diffusion coefficient must be included. These parameters are obtained by using existing models on current spreading and carrier diffusion, along with appropriate measurement techniques.

This chapter is divided into three main sections. In section 2.2 a short discussion on current, carrier and optical confinement in rib structure s/c devices is given. While in section 2.3 the rate equation is introduced and discussed, since in developing a model for TSLDs the rate equation is used extensively. In section 2.4, the models and experimental techniques used to obtain the diffusion coefficient, current density profile and carrier density profile are explained. Finally, some concluding remarks are given at the end of this chapter.

2.2 Rib Waveguide Double Heterostructure Device

Figure 2.2 shows a typical example of the material layers in a double heterostructure rib geometry device. In an actual device a layer of highly doped n^{++}GaAs (substrate) layer exists below the $n^{-}Ga_{1-y}Al_yAs$ (cladding) layer. Similarly a layer of p^{++}GaAs (capping) exists on top of the p^{+} $Ga_{1-x}Al_xAs$ (cladding) layer. These two layers (capping and substrate) are not intrinsic to the operation of the device but allow good ohmic contact to be obtained. Contacting to GaAlAs layers is difficult because Al oxidises easily, which leads to very poor metal contact.

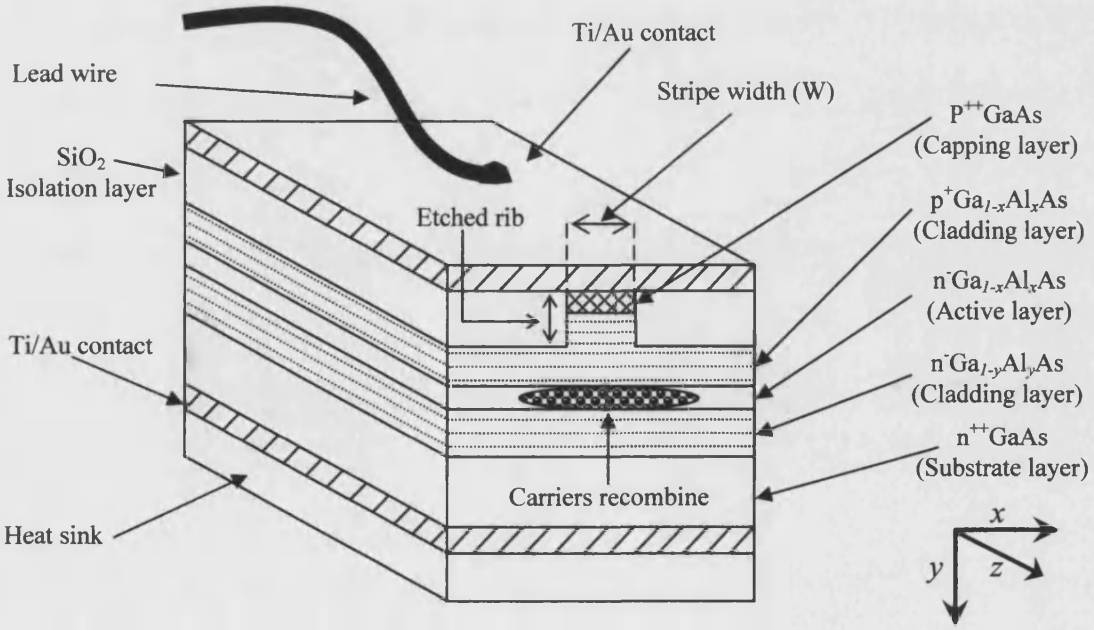

Figure 2.2: A diagram showing the typical material layers in a DH device.

In a double heterostructure device the undoped active layer of $Ga_{1-x}Al_xAs$ is sandwiched in between the n- and p-type cladding layers of $Ga_{1-y}Al_yAs$, and usually has a greater AlAs content than the active layer. The cladding layers are highly doped to reduce resistance to injection currents. More importantly the cladding layers have a much larger band-gap than the active layer, which provide excellent carrier confinement. In this situation holes and electrons are trapped in the active layer, and cannot cross the energy barrier to the n^- and p^- side layers respectively. This permits the successful recombination of electron with holes in the active layer, generating photons via spontaneous or stimulated emission.

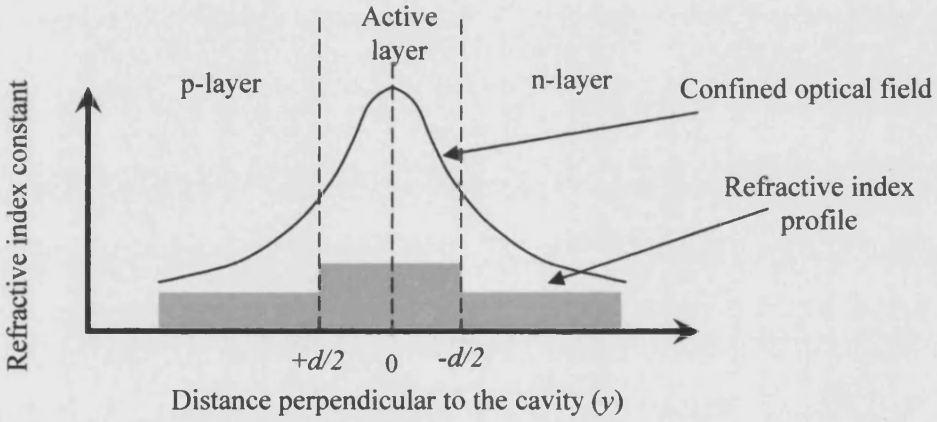

Figure 2.3: A diagram illustrating the variation in refractive index constant which is responsible for the confinement of the optical wave. *d* – width of active layer.

Furthermore, the relatively higher Al content on either side of the active layer produces a refractive index bump, illustrated in Figure 2.3. This variation in refractive index step helps confine much of the light vertically to a small region. In general the active layer thickness and the refractive index difference between the adjacent layers are designed to ensure that only a single mode can be sustained along the vertical axis. However as seen in Figure 2.3, the optical field is not just confined to the active layer but spreads also into the adjacent cladding layers. The characteristic of interest here is the ratio of the integral of the optical field distribution that is located in the central layer of the waveguide to the total integral of the distribution. This is equal to the confinement factor, Γ_v, which is defined as the

power that remains in the active layer divided by the total power, given in equation (2.1) (for a symmetric slab waveguide) [2].

$$\Gamma_V = \frac{\frac{1}{2}\int_{-d/2}^{+d/2}(\overline{E}\times\overline{H}^*)dy}{\frac{1}{2}\int_{-\infty}^{\infty}(\overline{E}\times\overline{H}^*)dy} \tag{2.1}$$

In equation (2.1), $\pm d/2$ is the total width of the active region, $\overline{E}$ is electric field and $\overline{H}$ is the magnetic field.

Apart from vertical confinement, the lateral (x) confinement of current is also equally important to ensure efficient device operation. The simplest method to obtain lateral confinement is by etching a rib. In order to form the rib the capping layer of GaAs is etched away outside the area of the stripe width, W, illustrated in Figure 2.2. The rib essentially limits the lateral spread of the injected current, which in turn restricts the lateral spread of carriers. As a consequence, the width of the optical emission laterally is reduced. However, it is important to highlight here that there are several factors that influence the spread of current in the lateral direction. These factors are discussed in greater detail in section 2.4 of this chapter.

Another consequence of etching a rib is that it creates a refractive index step between the area outside of the rib and the area underneath the rib (i.e. the deeper the etch depth the greater the refractive index step). Just as in the vertical (y) direction the device structure can also be designed to support only a single mode in the lateral direction. This can be achieved by creating a narrow rib width (~5 μm) with the appropriate lateral refractive index step. However all the SLDs used throughout this research are not index guided devices and therefore have a relatively shallow etch mainly for current confinement. In this type of device there exists a step difference in the gain (i.e. complex refractive index profile), underneath and outside the rib. In this case, it is gain guiding that produces the lateral mode profile.

2.3 Rate Equations

The rate equation provides a relationship between the injected carriers and the photons in the device. Solving the rate equations will give the spatial variation of photons and carriers in the device. In this section the rate equations, [3], are derived empirically by considering the conservation of charged carriers and photons in the device. First consider an optically active media (active layer) in which there is optical absorption or gain (when sufficient inversion population density exist), shown in Figure 2.4. In the derivation uniformity along x and y direction is assumed and only variation in the z direction is considered (i.e photons travel either in the +ve z direction or –ve z direction). It is also assumed that much of the optical field is confined to the active layer between $\pm d/2$. Let the photon density per unit effective volume of forward traveling photons (+ve z direction) in this active medium be P and the reverse traveling photons (-ve z direction) be Q. With reference to Figure 2.4, the net number of forward traveling photons in this volume at a given time Δt is

$$(P(z, t+\Delta t) - P(z, t)).\ \Delta V \tag{2.2}$$

where ΔV is the volume of the active media and $\Delta V = \Delta x.\ \Delta y.\ \Delta z$. Consider a density of photons, P, of unit cross sectional area passing through the active media with a uniform velocity v in the positive z direction. The number of photons entering and leaving this volume ΔV after a time Δt can be written as:-

Entering $P(z, t).\ \Delta x.\ \Delta y.v.\ \Delta t$ (2.3)

Leaving $P(z+\Delta z, t).\ \Delta x.\ \Delta y.v.\ \Delta t$ (2.4)

The change in net number of photons in the volume at a time Δt is

$$\{P(z+\Delta z, t) - P(z, t)\}.\ \Delta x.\ \Delta y.v.\ \Delta t \tag{2.5}$$

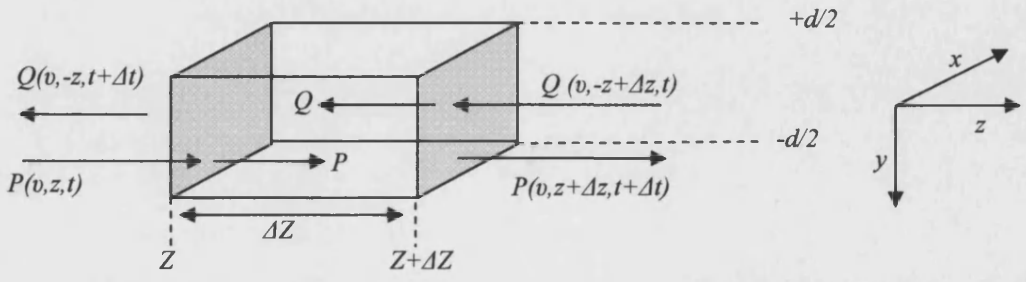

Figure 2.4: A diagram illustrating photons passing through a volume element of length Δz and unit cross sectional area.

Therefore the net number of photons in the active media after a time Δt is equal to the change in the net number of photons in the media plus the number of photons that are generated. In the active layer, photons are generated via two processes; spontaneous emission and simulated emission.

Spontaneous emission occurs at random and therefore gives incoherent radiation. Spontaneous emission also emits in all directions (isotropic radiation), in many different wavelengths, phase and polarization. Here for simplicity polarization and wavelength dependencies are ignored. Also since only the forward traveling photons are considered, only a fraction of the isotropic radiation actually contributes to the forward traveling photons. Let this fraction be represented by this symbol δ_f. Therefore contribution from spontaneous emission in the volume at a time Δt can be written as:-

$$\delta_f . \frac{N}{\tau_{sp}} . \Delta V . \Delta t \tag{2.6}$$

where N is the carrier density and τ_{sp} is the spontaneous emission recombination lifetime.

Contrary to spontaneous emission, stimulated emission gives coherent radiation because all photons released have identical phase, polarization, wavelength and direction. Therefore in the active layer, photons add in a constructive manner providing amplification. The net number of stimulated emission in the volume at a time Δt can be written as:-

$$\tilde{g}(N).P(z,t).\Delta t.\Delta V \tag{2.7}$$

where $\tilde{g}(N)$ is the gain of the material in units of time^{-1}.

Thus using equation (2.5), (2.6) and (2.7) the net number of forward traveling photons in the media after a time Δt is :-

$$P((z,t+\Delta t) - P(z,t)).\Delta x.\Delta y.\Delta z = (P(z,t) - P(z+\Delta z,t)).\ \Delta x.\Delta y.\ \Delta t.v + \tilde{g}\,(N)P(z,t) +$$

$$\delta_f . \frac{N}{\tau_{sp}} . \Delta x . \Delta y . \Delta z . \Delta t \tag{2.8}$$

Dividing equation (2.8) through by $\Delta x.\Delta y.\Delta z\ \Delta t$ and taking the limit of Δz tends to zero and Δt tends to zero gives the differential photon rate equation for the forward traveling photons, which is given below in equation (2.9).

$$\frac{dP}{dt} = -\upsilon\frac{dP}{dz} + \tilde{g}(N)P + \delta_f \frac{N}{\tau_{sp}} \tag{2.9}$$

The photon rate equation for the reverse traveling photons, represented by the notation Q, can be derived in a similar manner as in the case of forward traveling photons and is given in equation (2.10) below.

$$\frac{dQ}{dt} = \upsilon\frac{dQ}{dz} + \tilde{g}(N)Q + \delta_r \frac{N}{\tau_{sp}} \tag{2.10}$$

For solutions with no time variation $\frac{d}{dt} = 0$ (i.e. steady state solutions) [3], the photon rate equations for forward and reverse traveling photons can be written as:-

$$\frac{dP}{dz} = \frac{\tilde{g}(N)}{\upsilon}P + \delta_f \frac{N}{v.\tau_{sp}} \tag{2.11}$$

$$\frac{dQ}{dz} = -\frac{\tilde{g}(N)}{\upsilon}Q - \delta_r \frac{N}{v.\tau_{sp}} \tag{2.12}$$

where $\frac{\tilde{g}(N)}{\upsilon} = g(N)$ is the gain of the material in unit length^{-1} and δ_r represents the fraction of spontaneous emission in the reverse direction. Note, in the derivation of the photon rate equations phase effects were not considered (i.e. averaged over phase) since in the case of LEDs a spread of wavelengths exists.

The discussions have so far only considered the relationship between carrier inversion population and the photons generated in the media. However, a similar time dependent relationship can be derived between the carrier inversion population and the injected current density, given below in equation (A1.8). The full derivation for equation (A1.8) can be found in Appendix 1A [3].

$$\frac{\partial N}{dt}=\frac{J_0}{q.d}-\tilde{g}(N)[P+Q]-\frac{N}{\tau_{sp}} \tag{A1.8}$$

In equation (A1.8), q is the electron charge, d is the thickness of the active layer and J_0 is the injected current density. The steady state solution to equation (A1.8) takes the form [4]:

$$\frac{J_0}{qd}=\tilde{g}(N)[P+Q]+\frac{N}{\tau_{sp}} \tag{A1.9}$$

In the formulation of the ray model for TSLDs the steady state solution of the rate equations has been used to form the basis of the model. Discussion on the comprehensive ray model for TSLDs is given in Chapter 6 of this thesis.

2.4 Current Spreading and Carrier Diffusion

Figure 2.5 illustrates the flow of current in a typical rib structure s/c device. In this type of device, due to the rib, current that is injected is constricted at the edges and flows mainly in the centre region. However, once free from the restriction of the rib, the current spreads laterally in the cladding layer. This results in a current density distribution $J_y(x)$ as shown in Figure 2.5. At the boundary between the cladding and active layer the current flows vertically into the active layer. Finally, in the active layer the lateral movement of carriers takes place by diffusion.

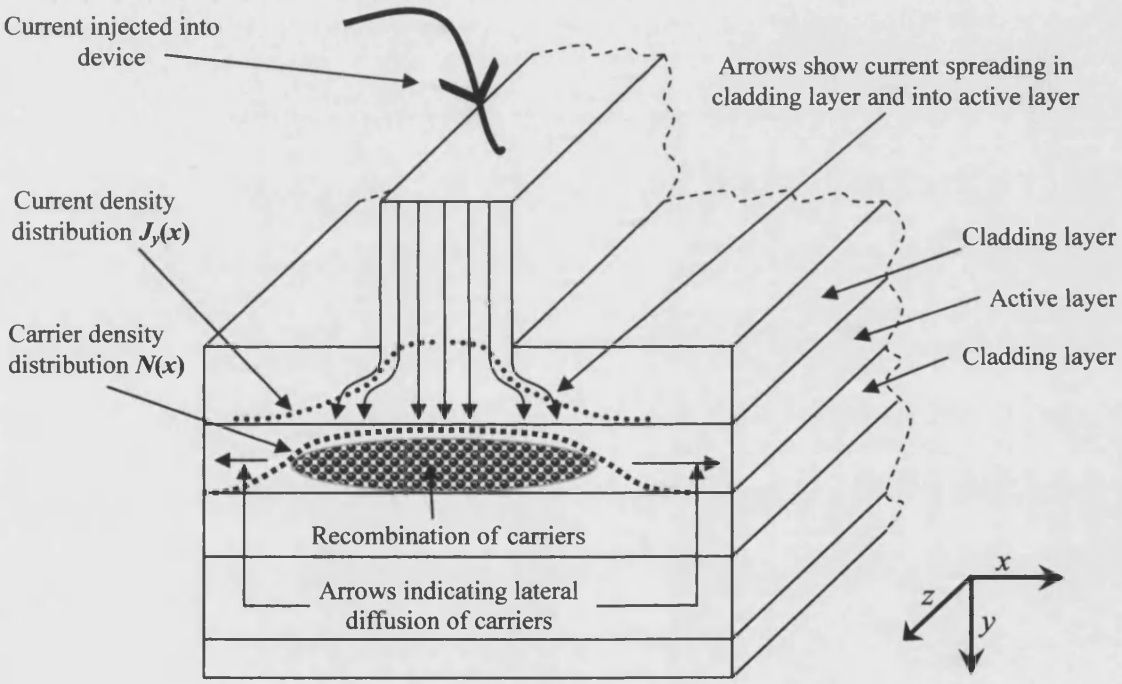

Figure 2.5: A diagram illustrating the process of current spreading in the cladding layer and carrier diffusion in the active layer for a rib geometry device.

In this research two existing models have been used to quantify current spreading and carrier diffusion. The first model by Yonezu et. al. [5], gives a relatively simplified treatment of current spreading which deals particularly with the edge leakage current that flows laterally in the cladding layer outside the area of the rib. The second model [6], deals particularly with the lateral spread of carriers caused by diffusion. The model, [6], employs the continuity equation [7], which in general

represents the conservation of carriers in the active layer. By using the calculated current density distribution, obtained from [5], the diffusion equation is solved, to give the carrier density distribution. However, the above is true if the diffusion coefficient, which is material dependent, is known. The diffusion coefficient is obtained by matching the calculated carrier density squared profile with the experimentally measured spontaneous emission profile.

Discussions on the current spreading model and the diffusion model are given in section 2.4.1 and 2.4.2 respectively. The experimental and simulation techniques used to obtain the diffusion coefficient and the carrier density squared profile is given in section 2.4.3.

2.4.1 *Current Spreading Model*

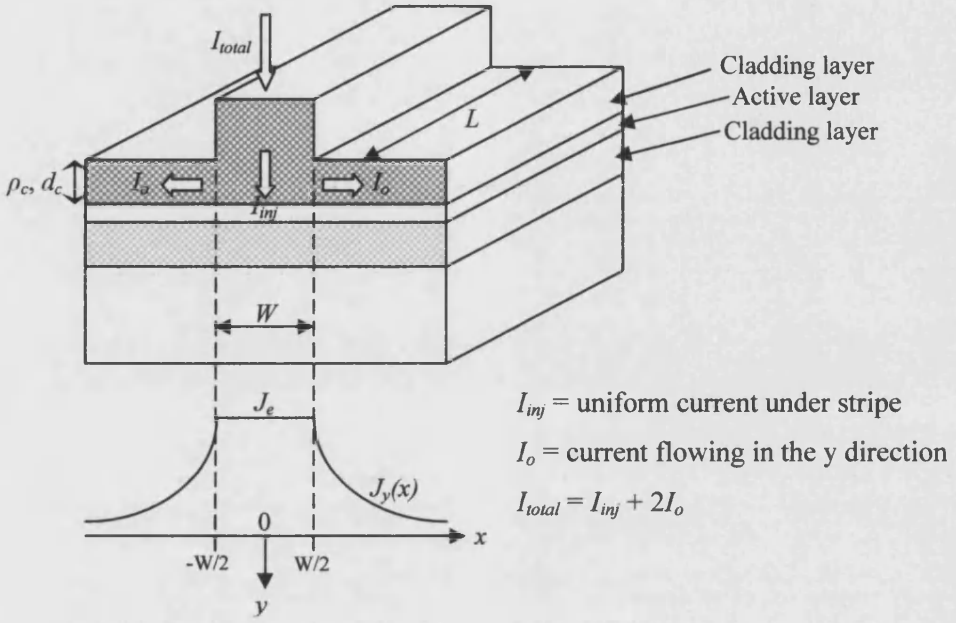

Figure 2.6: Current flow model for current spreading effect calculation.

In the model, [5], the distribution of current density across the junction $J_y(x)$ is obtained approximately by assuming constant current density J_e at the junction underneath the rib, illustrated in Figure 2.6. Outside the rib however, the current density varies with x and decreases as $|x|$ increases, these assumptions are represented by equation (2.13) and (2.14) (see Appendix A in [5] for full derivation)

$$J_e = J_{inj} = \frac{I_{inj}}{L.W} \qquad |x| < \frac{W}{2} \qquad (2.13)$$

$$J_y(x) = \frac{J_{inj}}{\left(1 + \frac{|x| - \frac{W}{2}}{\ell_0}\right)^2} \qquad |x| > \frac{W}{2} \qquad (2.14)$$

$$\ell_0 = \frac{2}{\beta \rho_y I_0}, \quad \beta = \frac{q}{nkT} \text{ and } \rho_y = \frac{\rho_c}{d_c.L}.$$

In the equations (2.13) and (2.14), I_0 is the current flowing in the x direction in the cladding layer, I_{inj} is the uniform current underneath stripe flowing into the active

layer, β is the exponent in the usual current-voltage equation of the diode, ℓ_0 is the spreading length of the injected current from the edge of the rib at $x = \pm W/2$, ρ_c is the resistivity of the cladding layer and d_c is the remaining thickness of the cladding layer after etching, L is the cavity length and W is the width of the rib. In some devices the cladding layers does not consist of one homogeneous layer with cladding thickness d_c and resistivity ρ_c. Sometimes there are more layers with different thickness (d_1, d_2, d_3) and different resisitivity (ρ_1, ρ_2, ρ_3). In such a case the variable d and ρ in all the equations is to be replaced by an effective cladding thickness d_{eff} and ρ_{eff}. These values can be calculated with the following equations:-

$$d = d_{eff} = d_1 + d_2 + d_3$$

$$\rho = \rho_{eff} = \frac{d_1 + d_2 + d_3}{\frac{d_1}{\rho_1} + \frac{d_2}{\rho_2} + \frac{d_3}{\rho_3}}$$

In brief, the important point to note from the model is that the current density distribution $J_y(x)$ and current spreading length ℓ_0, for a device of length L, depends on four parameters, which are:

1. d_c – remaining cladding layer thickness after etching
2. W – width of the rib
3. N_c – doping density of the cladding layer since $\rho_c = \frac{1}{q\mu_p N_c}$, μ_p - hole mobility
4. I_{total} – total current injected into the device

The parameter N_c is usually supplied by the GaAs material manufacturer.

- ***Simulations Results and Discussions***

A number of simulations was performed to study the effect each of these parameters W, d_c, N_c, and I_{total} have on the current spreading length, ℓ_0. Table 2.1 contains the dimensions of the devices used and the relevant parameters for which the simulation was made. The simulations were based on two different types of semiconductor materials, QT543R and QT503A. Both materials have been used throughout the research to fabricate the SLDs. Specification for these materials can be found in Appendix 2A. Note, in the actual simulation three out of the four parameters mentioned above are kept constant while one is varied. Figures 2.7, 2.8, 2.9 and 3.0 shows the different effect each of the four parameters mentioned above have on ℓ_0.

Device Parameters	QT543R	QT503A	Description/ unit
W	50	50	rib width (μm)
L	1000	1000	length of device (μm)
N_c	7.5×10^{17}	9.0×10^{17}	cladding layer doping density (cm^{-3})
d_c	1.0	0.85	remaining cladding layer thickness (μm)
μ_p	200	200	hole mobility (cm^2/Vs)
I_{total}	1.0	1.0	total injected current (A)

Table 2.1: Device dimensions and relevant parameters used in the simulations.

Figure 2.7 shows a graph of ℓ_0/W in percentage against W, which gives an indication of how much current has leaked out sideways for stripe widths varying from 5μm -50μm. The graph shows that in both materials (QT543R and QT503A) for stripe widths < 10μm, as much as 20-30% of the total current has leaked out sideways in the cladding layer. In narrow stripe devices ℓ_0 can be limited by reducing the doping density N_c, which effectively increases the resistivity of the cladding layers. The drawback with this method is that the resistance to injected current is also increased. Alternatively reducing d_c will help limit ℓ_0, but at the consequence of increasing the lateral refractive index step. This may or may not be

Figure 2.7: Graph of ℓ_0/W X 100(%) against W

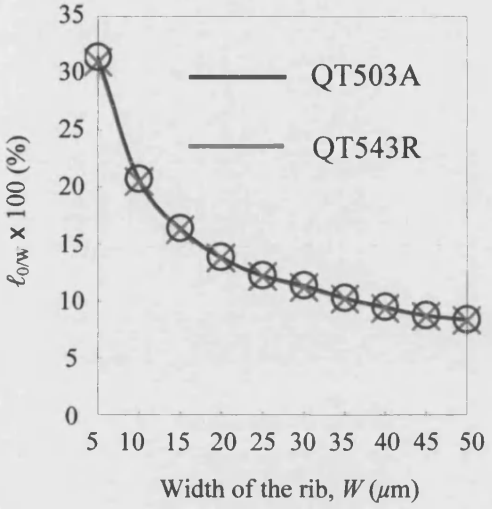

Fixed parameters	QT543R	QT503A
N_c	7.5 x 10^{17}	9.0 x 10^{17}
d_c	1.0μm	0.85μm
I_{total}	1.0A	1.0A

Figure 2.8: Graph of ℓ_0 against I_{total}

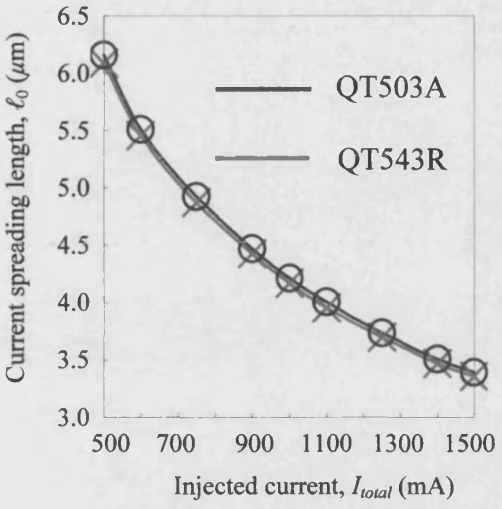

Fixed parameters	QT543R	QT503A
N_c	7.5 x 10^{17}	9.0 x 10^{17}
d_c	1.0μm	0.85μm
W	50μm	50μm

Figure 2.9: Graph of ℓ_0 against d_c

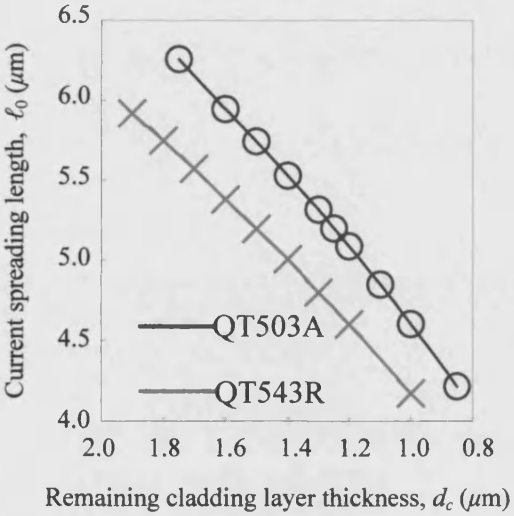

Fixed parameters	QT543R	QT503A
N_c	7.5 x 10^{17}	9.0 x 10^{17}
W	50μm	50μm
I_{total}	1.0A	1.0A

Figure 2.10: Graph of ℓ_0 against N_c

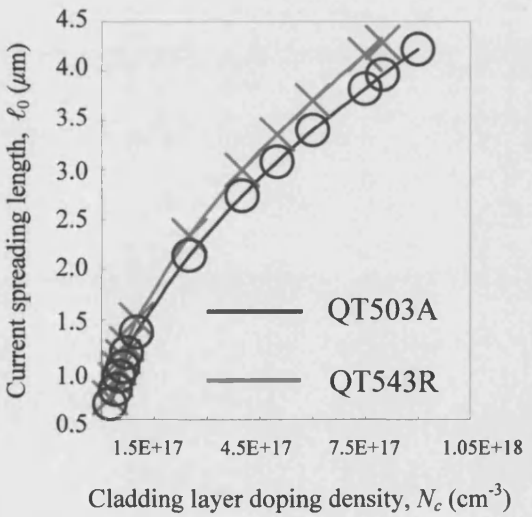

Fixed parameters	QT543R	QT503A
d_c	1.0μm	0.85μm
W	50μm	50μm
I_{total}	1.0A	1.0A

desirable depending on the particular application of the device. Conversely, the graph indicates that in broad area devices the loss of current flowing sideways is less.

Figure 2.8 shows a graph of ℓ_0 against the total injected current I_{total}. The graph shows a steady decline of ℓ_0 with increase in current. In both materials a 300% increase in injected current sees a 50% drop in current spreading length. This is due to the fact that the p-n junction is in forward biased condition and thus current is able to flow more easily across the junction into the active layer.

Figure 2.9 shows a graph of ℓ_0 against the remaining cladding layer thickness after etching d_c. As expected, in both materials ℓ_0 decreases as d_c is reduced. However, the graph shows that for the same value of d_c, current spreading is slightly less in material QT543R than in material QT503A. This is to be expected as the cladding layer resistivity is higher in QT543R than in QT503A since the value for N_c is lower in QT543R (see Table 2.1).

Figure 2.10 shows a graph of ℓ_0 against N_c. In this simulation N_c was varied between 1.0×10^{16} cm^{-3} up to 1.0×10^{18} cm^{-3} (i.e. going from higher to lower resistivity). Results show that for the same value of N_c current spreading is higher in material QT543R than in QT503A. This is not surprising since the cladding layer thickness d_c is slightly thicker in material QT543R.

In conclusion, with reference to Figure 2.9 and 2.10, simulation results show that for two devices with similar dimensions made from different materials, varying the parameter d_c and N_c had the most dramatic effect on the spreading length, ℓ_0.

2.4.2 The Continuity Equation

In general the continuity equation is simply an equation representing the conservation of carriers in the active layer. In this case, the active layer thickness, d, is smaller than the diffusion length. Hence the diffusion equation can be taken in the lateral (x) direction alone and along the vertical (y) direction is uniform. Also, at low currents stimulated emission is small and can be ignored. Furthermore, in GaAs auger recombination can be thought as negligible, leaving spontaneous recombination as the main carrier loss term. Thus the continuity equation [7] can be written as:-

$$D\frac{\partial^2 N(x)}{\partial x^2} - \underbrace{B_r[N_0 + N(x)]N(x)}_{A} = -\frac{J_y(x)}{qd} \tag{2.15}$$

D = diffusion coefficient
N_0 = doping density of the active layer
B_r = bimolecular recombination constant

In equation (2.15), ambipolar diffusion equation is assumed since both types of carriers are present. Usually the injected carrier density $N(x)$ is much bigger than the doping density, i.e. $N_0(N(x)>>N_0)$, hence N_0 in term A, which represents spontaneous emission, can be neglected. Given the current density distribution, $J_y(x)$, obtained from [5], the continuity equation can be solved to find the distribution of carriers $N(x)$. Note the diffusion equation was solved numerically due to the nonlinearity of the equation [6].

It is important to highlight here that $N(x)$ at every point along the length of the device can only be obtained if the diffusion parameter D is known. Although D is material dependent it is however not specified by the manufacturer. However this parameter can be obtained by matching the calculated carrier distribution profile with the experimentally measured spontaneous emission profile. The diffusion term D is adjusted until an approximate shape fit is achieved. The experimental technique used to measure the spontaneous emission profile is discussed in the following section.

2.4.3 Experimental Technique

It was mentioned in section 2.3 that light emitted from SLDs is generated from spontaneous and stimulated emission. If the current density in the device is very low then it can be assumed that the spontaneous emission rate is much larger than the stimulated emission rate. It is known from equation 2.15 that light generated through spontaneous emission is represented by the formulae $B_r N^2(x)$ if N_0 is negligible. Therefore under the condition when stimulated emission is insignificant the measured output light from the SLD can be said to be proportional to $N^2(x)$. Hence it is possible to compare the experimentally measured spontaneous intensity with $N^2(x)$.

The experimental set-up to measure the output light from SLDs is shown in Figure 2.11. The device is placed in front of an objective lens which is used to focus the light into an infra-red camera. In the measurement a short wave pass (SWP) filter was used to ensure that only the shortest wavelength light is measured (i.e. light generated near the output facet). Longer wavelength light originating from the back has gain and therefore gives a distorted profile at the facet. The intensity recorded should therefore be only from the spontaneous light generated very close to the output facet. This light gives the position of the carriers in the active layer.

Furthermore to ensure that accurate measurements are being taken the exposure time of the camera to the output light is kept to a minimum. This is to avoid camera burn-in effect, which causes the signal to rise slowly over a number of minutes until saturation.

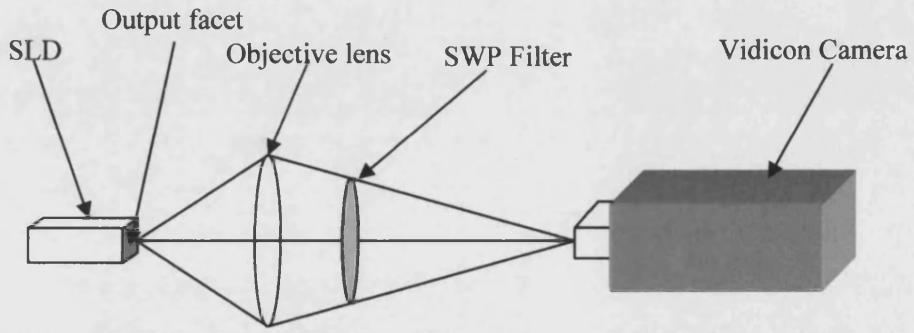

Figure 2.11: Diagram of apparatus used to measure spontaneous emission from SLDs.

2.4.4 *Simulation Techniques*

- ***First Test***

In order to test the validity of the models in predicting the carrier density profiles three simulation tests has been designed. In the first test only current spreading is considered and the effect of diffusion is ignored, i.e. $D = 0$. Therefore equation (2.15) can be written as (when $N_0 \approx 0$ for undoped active layer)

$$\frac{J_y(x)}{qd} = B_r(N^2(x)) \tag{2.16}$$

In this simulation parameters such as W, L, N_c and d_c are known and are listed in Table 2.2. Note, in the simulation d_c was allowed to vary up to ± 0.15μm from the measured value in order to obtain the best match profile.

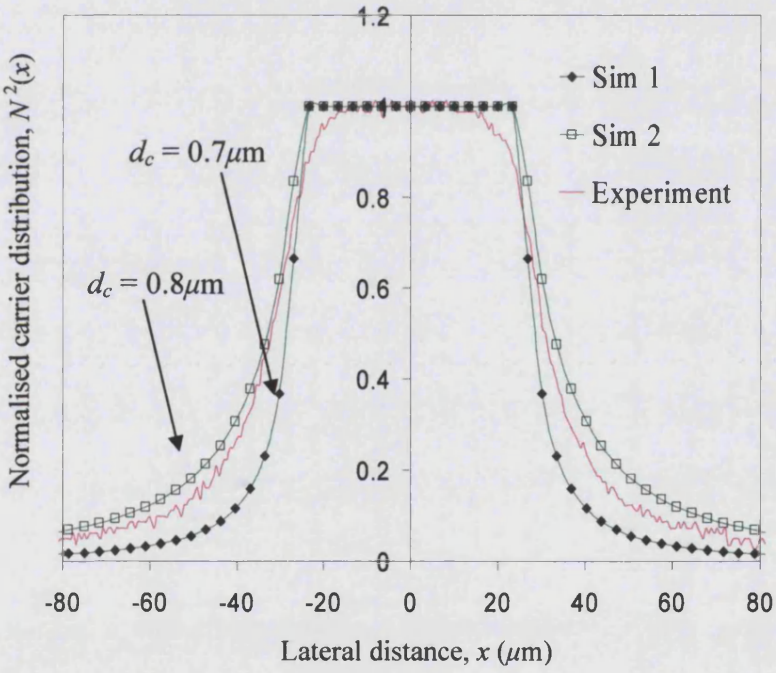

Material: QT503A
Device: UB1017

Table 2.2

W	50μm
L	1000μm
N_c	9.0 x 10^{17} cm^{-3}
d_c	0.85μm

Figure 2.12: Comparison of the measured $N^2(x)$ profile and the calculated $N^2(x)$ profiles by the current spreading model.

Results in Figure 2.12, show that a good match could not be obtained between the experimental and the calculated carrier profile. Although a reasonable match from the bottom half the profile was obtained for $d_c = 0.8\mu$m, a good match from the top half of the profile could not be obtained at all.

- ***Second Test***

In the second test current spreading is ignored and diffusion is the only contributor to the distribution of carrier in the active layer. Therefore in this case a rectangular current density distribution is assumed, which can be written as

$$J_y(x)=\begin{cases} J_0 & -\frac{W}{2} < x < \frac{W}{2} \\ 0 & \frac{W}{2} < x < -\frac{W}{2} \end{cases}$$

In this simulation the diffusion coefficient D, is adjusted until a match is obtained between the calculated and the experimentally measured profile. Parameters used in the simulation are given in Table 2.3.

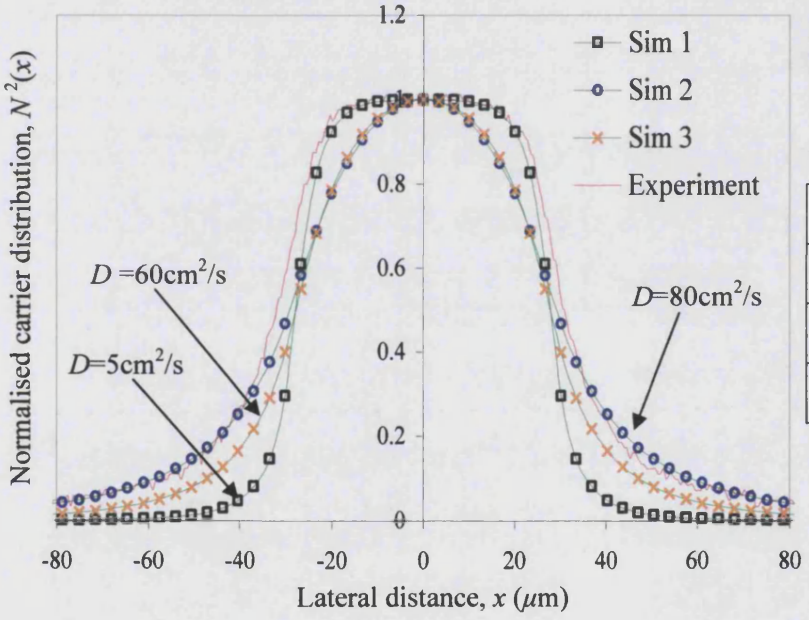

Material: QT503A
Device: UB1017

Table 2.3

W	50μm
L	1000μm
N_c	9.0 x 10^{17} cm^{-3}
d_c	0.85μm

Figure 2.13: Comparison of the measured $N^2(x)$ profile and the calculated $N^2(x)$ profiles using the diffusion equation.

From Figure 2.13 it can be seen that a good overall match between the measured and the calculated profile was not achieved. In the simulation a reasonable match from the bottom half of the profile was obtained for D = 80cm^2/s. Unfortunately, with this value of D (80cm^2/s) the top half of the calculated profile is too narrow compared to the experimental profile. Conversely, with D = 5cm^2/s a good match from the top half of the profile was obtained but the bottom half of the calculated profile is much narrower than the measured profile.

- ***Third Test***

So far the first two simulation techniques presented have not been successful in obtaining a good match between the measured and the calculated $N^2(x)$ profile. In the third test both effects (current spreading and carrier diffusion) are considered. The current density distribution $J_y(x)$ obtained from the current spreading model is substituted into the diffusion equation. The diffusion equation is then solved numerically [6], with D held as a constant. The simulation is then repeated for different values of D until a match between the measured and the calculated carrier density squared profile is obtained. Table 2.4 contains details of the devices measured.

Device	UB754	UB755	UB756	UB1027	UB1036	UB1037
Material	QT543R	QT543R	QT543R	QT503A	QT503A	QT503A
W (μm)	50	50	50	50	50	50
L (μm)	1000	1000	1000	1000	1000	1000
d_c (μm)	1.0	1.0	1.0	0.85	0.85	0.85
N_c (cm^{-3})	$7.5x10^{17}$	$7.5x10^{17}$	$7.5x10^{17}$	$9.0x10^{17}$	$9.0x10^{17}$	$9.0x10^{17}$

Table 2.4: Details of the measured devices.

Figures 2.14, 2.15, 2.16, 2.17, 2.18 and 2.19 shows the best match profiles for several parallel stripe SLDs made from material QT543R and QT503A. An overall good match between the measured and calculated $N^2(x)$ profile was obtained for all the devices listed in Table 2.4. The best matched profiles for devices made from material QT543R were obtained with D = 30cm^2/s and for devices made from material QT503A with D = 40cm^2/s. Accuracy of the diffusion coefficient measurement is of the order ± 5cm^2/s as changes in the diffusion coefficient smaller than this have a negligible effect on the carrier profile.

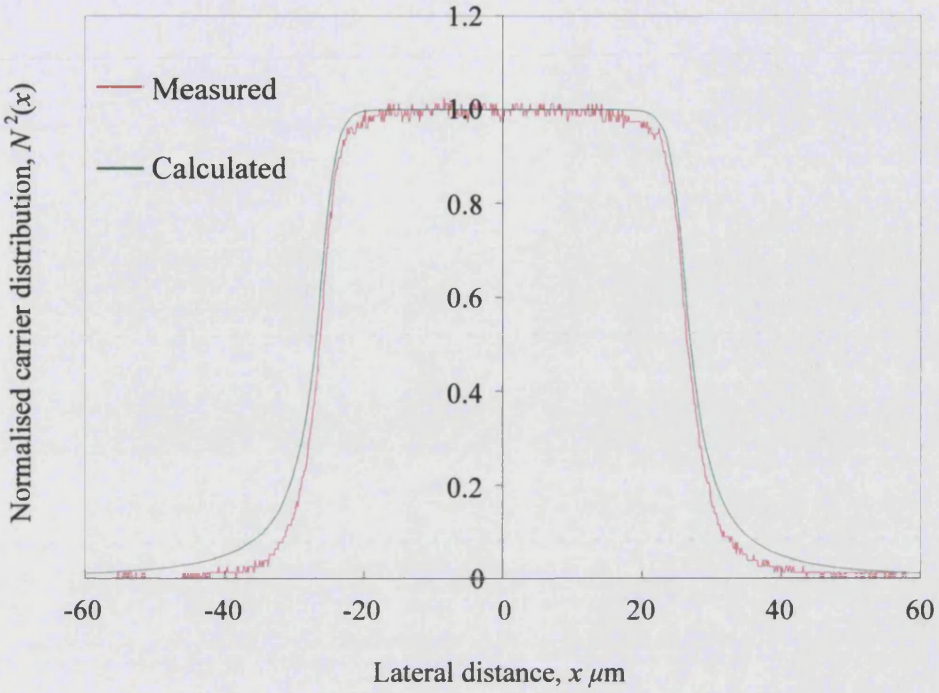

Figure 2.14: Comparison of the measured carrier density $N^2(x)$ profile of device UB754 at 0.5A and the calculated $N^2(x)$ profile.

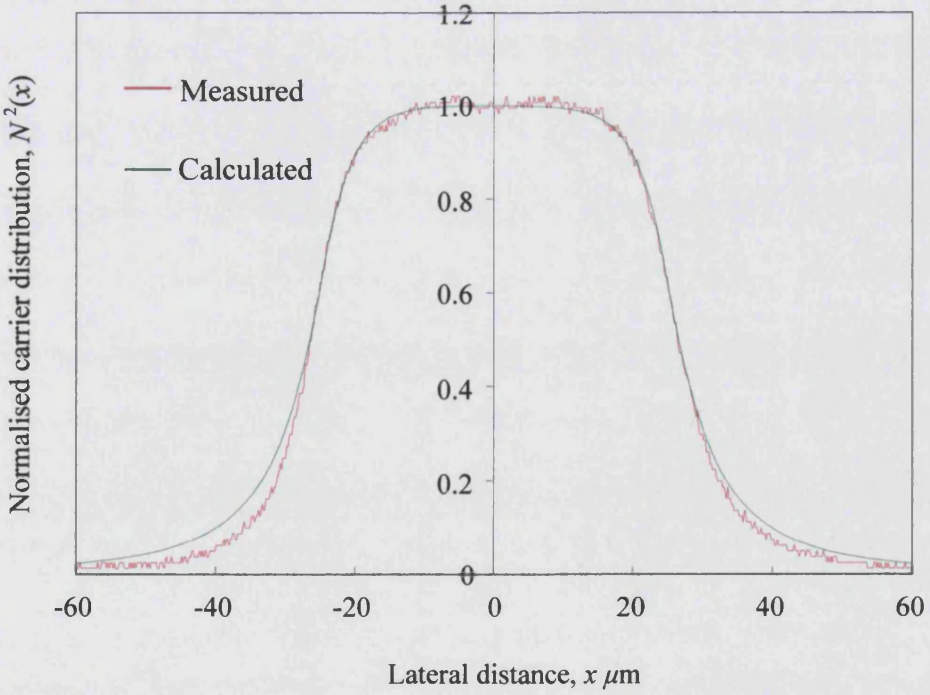

Figure 2.15: Comparison of the measured carrier density $N^2(x)$ profile of device UB1027 at 0.5A and the calculated $N^2(x)$ profile.

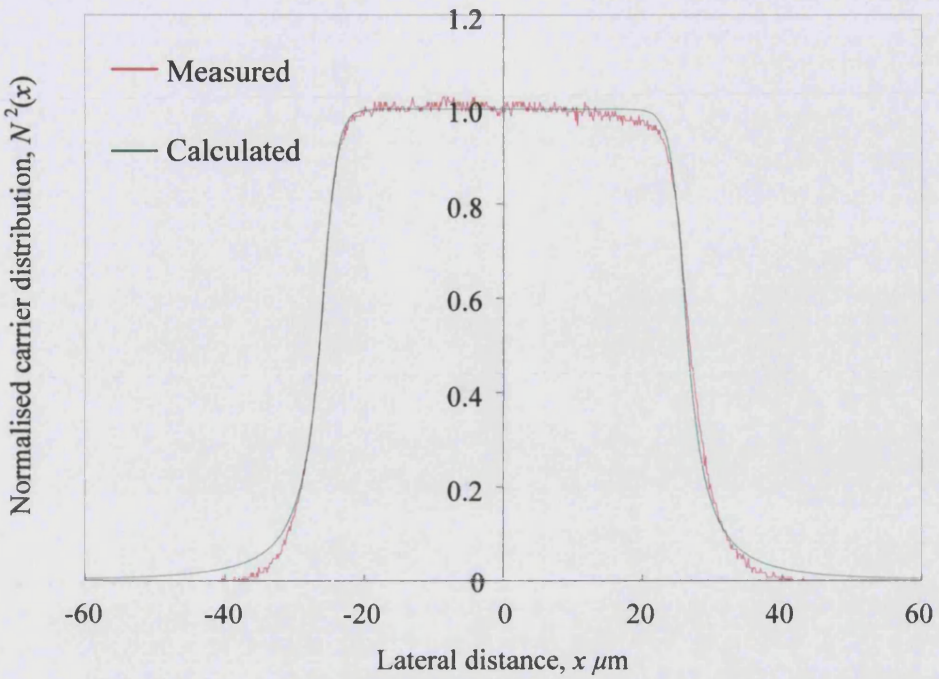

Figure 2.16: Comparison of the measured carrier density $N^2(x)$ profile of device UB755 at 1.0A and the calculated $N^2(x)$ profile.

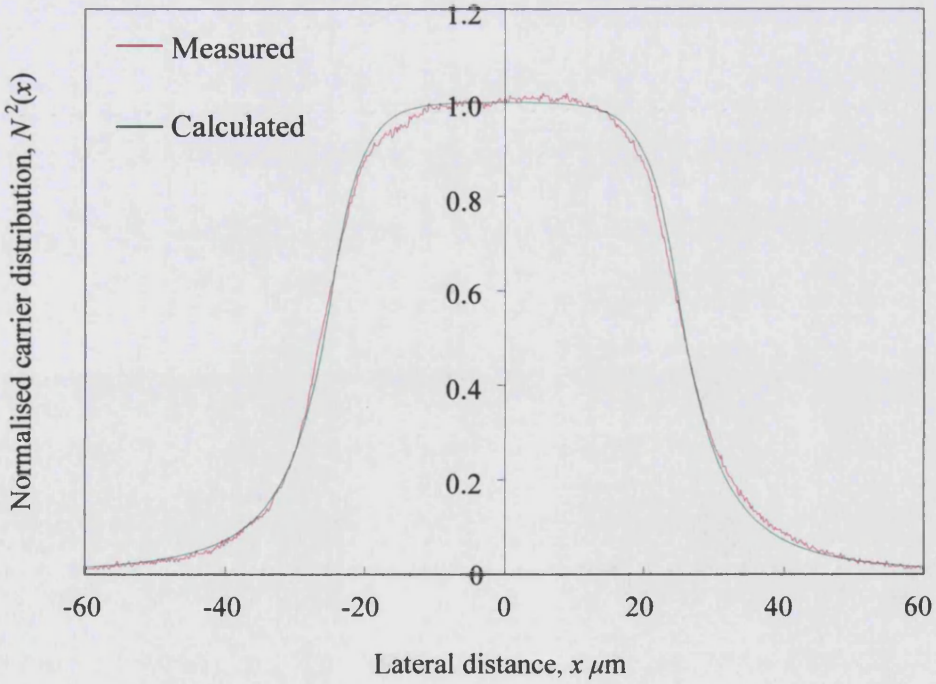

Figure 2.17: Comparison of the measured carrier density $N^2(x)$ profile of device UB1036 at 1.0A and the calculated $N^2(x)$ profile.

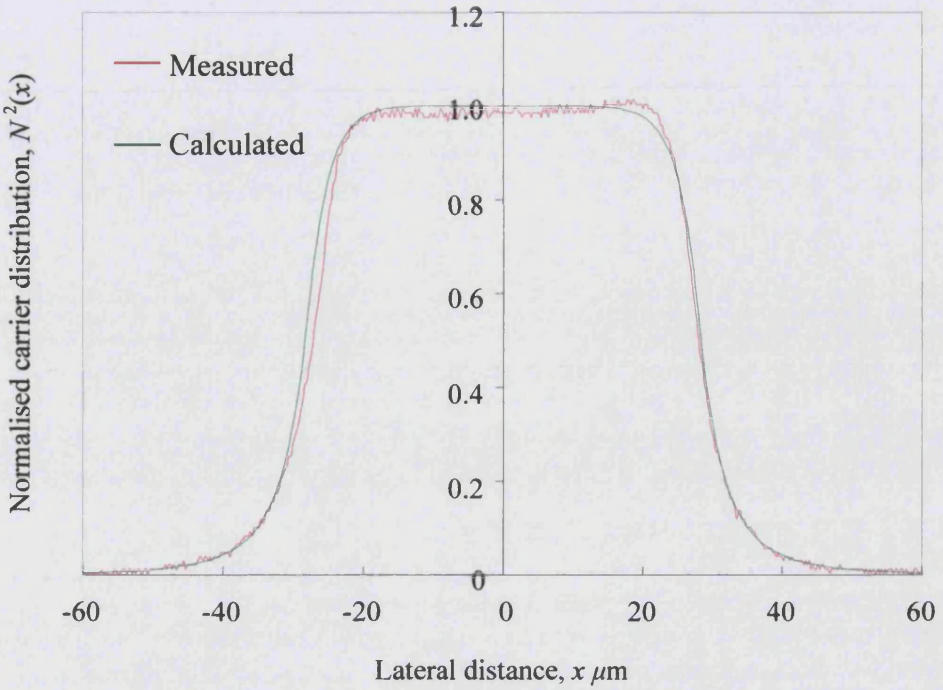

Figure 2.18: Comparison of the measured carrier density $N^2(x)$ profile of device UB756 at 1.5A and the calculated $N^2(x)$ profile.

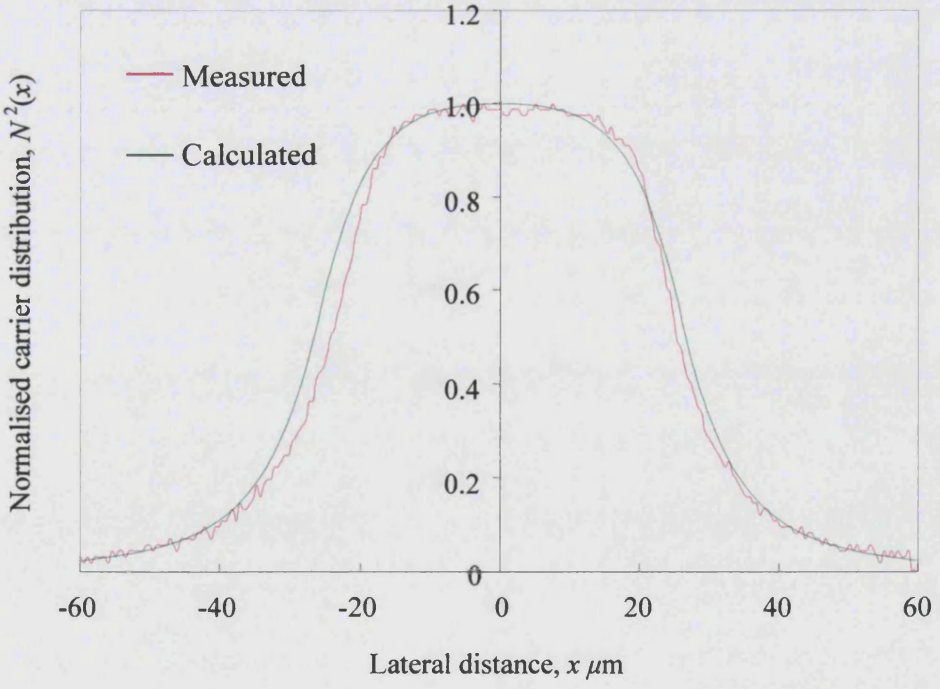

Figure 2.19: Comparison of the measured carrier density $N^2(x)$ profile of device UB1037 at 1.5A and the calculated $N^2(x)$ profile.

2.5 Concluding Remarks

A discussion on carrier and optical confinement in semiconductor rib structure devices has been given in section 2.2 since the SLDs presented in this thesis are of this type. This is followed by a discussion on the photon rate equations in section 2.3, which is used in the formulation of the ray model for TSLDs in Chapter 5 and 6. In particular the distribution of carriers in s/c rib structure devices, determined by current spreading and carrier diffusion, has been discussed in section 2.4. The distribution of carriers is of interest since in TSLDs there is a lateral (x) and longitudinal (z) variation of carriers. Therefore to model such devices it is essential to be able to accurately predict the carrier density profile $N(x)$ at every z. In order to predict the carrier density profiles two existing models has been used [5], [6]. Results presented in section 2.4 have shown that both factors (current spreading and carrier diffusion), must be considered to obtain the best match profile between experiment and those predicted by the model.

References

[1] *G. H. B. Thompson*, **'Physics of Semiconductor Devices'**, John Wiley and Sons, Great Britain, p305, 1980.

[2] *I. Middlemast*, **'A Comprehensive Model of Superluminescent Diodes'**, PhD thesis, University of Bath, 1986.

[3] *J. Sarma*, **Lecture Notes**, University of Bath, 2000.

[4] *G. P. Aggrawal*, **'Semiconductor Lasers'**, Kluwer Academic, 2nd ed. 1993.

[5] *H. Yonezu, I. Sakuma, K. Kobayashi, T. Kamejima, M. Ueno and Y. Nannichi*, **'A GaAs-Al_xGa_{1-x} Double Heterostructure Planar Stripe Laser'**, Japanese Journal of Applied Physics, Vol. 12, No. 10, pp. 1585-1592, 1973.

[6] *F. Causa, J. Sarma, R. Balasubramanyam*, **'A New Method for Computing Nonlinear Carrier Diffusion in Semiconductor Optical Devices'**, IEEE Transactions Electron Devices, Vol. 46, No. 6, pp. 1135 – 1139, 1999

[7] *N. S. Brooks*, **'Design and Development of Tapered Geometry Semiconductor Optical Sources'**, PhD thesis, University of Bath, 1998.

.

Chapter 3

Parallel Stripe Superluminescent Diodes

3.1 Introduction

The primary objective of this chapter is to present the results of a theoretical study of parallel stripe superluminescent diodes (PSLDs). In particular to examine the effects of hole-burning that occurs at high levels of pumping. Findings from the theoretical study will contribute towards improving methods of increasing the available output power from SLDs. The chapter begins with a description of the mathematical model used to analyse such structures. The model has been developed using the steady state rate equations, which was introduced in the previous chapter in section 2.3. Simulation results from the model are then presented and discussed. The effects of various parameters such as facet reflectivities and length of device are shown and the significance of these results in terms of high power superluminescent design is discussed. Finally comparisons of the experimental results from fabricated PSLDs with those predicted from the model are presented.

3.2 Description of the Model

The theoretical study of the parallel stripe superluminescent diode (SLD) structure, Figure 3.1, which is considered in this model, is restricted to a one dimensional (longitudinal) analysis. In order to maintain the one dimensional analysis several simplifying approximations were made. The approximation amounts to neglecting the effects of current spreading and carrier diffusion. However, the complication introduced by optically induced carrier depletion (hole-burning) is included in the model. In general such an analysis is computationally expensive. This is because a self consistent solution to the rate equations [1] must be found at every step along the

length of the device. In order to reduce the excessive computational time, a quasi-analytic approach based on a constant carrier analysis first introduced by Streifer [2] for the analysis of laser diodes, but subsequently applied by Adams [3] to SLDs, was applied for this work. The large saving in computation time is achieved because the rate equations, assuming constant carrier, have relatively simple analytic solutions. The numerical computation is then reduced to evaluating an algebraic equation to self-consistently determine the value for the assumed constant carrier density distribution. The important point to note here is that the numerical computation now solves a set of algebraic equation rather than a set of coupled (non-linear) differential equations, which involves directly solving the rate equations.

A further feature of this model that has been included is the evaluation of the longitudinal distribution of the carrier density distribution. In an actual device the longitudinal distribution of carriers is not constant, although initially in the model this was assumed to be constant. Consequently, the constant carrier method allows the value of the carrier density that is consistent with the actual photon density in the device to be found relatively fast, which is then used to find the longitudinal distribution of carriers. This new feature enables a direct visualization of the hole-burning effects, which occurs when the photon density in the device is large. More importantly, this permits the consideration of design features to reduce hole-burning effects in order to achieve a more efficient device operational characteristic and thus increase the available output power from the device.

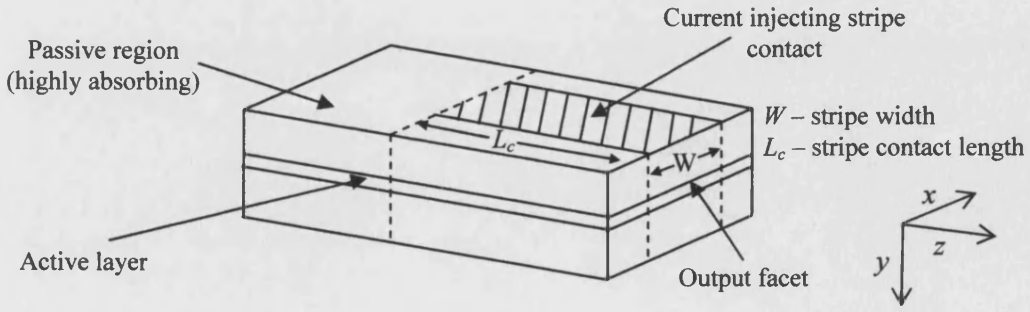

Figure 3.1: Schematic diagram of a parallel stripe SLD with a passive absorber at the back.

The numerical procedure followed to find the longitudinal distribution of photons and carriers in parallel stripe SLDs using the constant carrier method is given in Figure 3.2. First, the set of first ordinary differential equations (A3.1), (A3.2), which are coupled via the charge conservation equation (A3.10) are solved as shown in Appendix 3A.

$$\frac{dP}{dz}=\frac{\tilde{g}(N)}{\upsilon}\cdot P+\frac{\delta_f}{\upsilon}\cdot\frac{N}{\tau_{sp}} \tag{A3.1}$$

$$\frac{dQ}{dz}=-\frac{\tilde{g}(N)}{\upsilon}\cdot Q-\frac{\delta_r(\lambda)}{\upsilon}\cdot\frac{N}{\tau_{sp}} \tag{A3.2}$$

$$\frac{J_0}{qd}=\tilde{g}(N)[P(z,N)+Q(z,N)]+\frac{N}{\tau_{sp}} \tag{A3.10}$$

The analytic solution for these equations takes the form, [4]:

$$P(z,\overline{N})=P_0\exp(\overline{g}z)+(\exp(\overline{g}z)-1)\overline{P}_{sp} \tag{A3.17}$$

$$Q(z,\overline{N})=Q_0\exp(-\overline{g}z)+(\exp(-\overline{g}z)-1)\overline{Q}_{sp} \tag{A3.18}$$

where $\overline{N}$ is the constant carrier density, P_0 and Q_0 are constants associated to the spontaneous emission in the device, τ_{sp} is the spontaneous emission recombination lifetime, and $\overline{g}$ is given by:

$$\overline{g}=\frac{\tilde{g}(\overline{N})}{\upsilon}=\Gamma_v\cdot\frac{\alpha_0(\overline{N}-N_T)}{\upsilon} \tag{3.1}$$

where $\tilde{g}(\overline{N})$ is the material gain, Γ_v is the optical field confinement factor in the vertical direction, N_T = 1.55 x 10^{18} cm^{-3} [1] is the transparency carrier density for GaAs, and α_0 is the gain constant. The initial value for $\overline{N}$ is arbitrarily set at 1.0 x 10^{18} cm^{-3} for the first iteration, which is just below the value for N_T. The material gain obtained is then used to calculate $\overline{P}_{sp}$ and $\overline{Q}_{sp}$ which is given by:

$$\overline{P}_{sp}=\frac{\delta_f}{\upsilon\overline{g}}\cdot\frac{\overline{N}}{\tau_{sp}} \tag{A3.8}$$

$$\overline{Q}_{sp}=\frac{\delta_r}{\upsilon\overline{g}}\cdot\frac{\overline{N}}{\tau_{sp}} \tag{A3.9}$$

where $\delta_{f/r}$ is the fraction of spontaneous emission considered to contribute to the forward and reverse traveling photons.

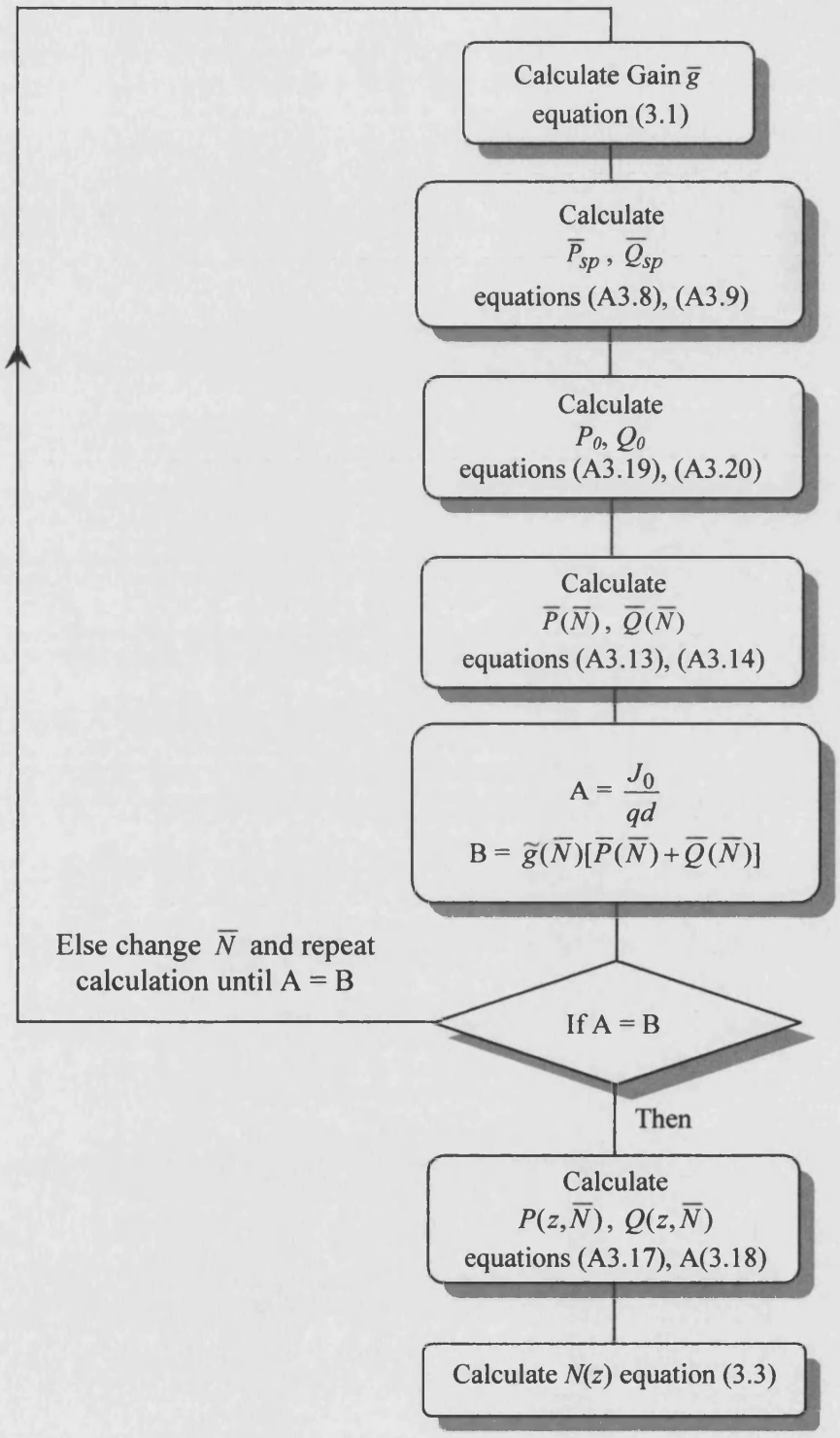

Figure 3.2: Flow diagram of the numerical procedure to find the self-consistent value for the assumed constant carrier distribution.

Next the values for $\overline{P}_{sp}$ and $\overline{Q}_{sp}$ obtained are used to calculate for P_0 and Q_0, which satisfy the boundary conditions at $z = 0$ and $z = L_c$ (see Figure A3.1 in Appendix 3A), given by:

$$P_0 = \frac{1}{(1 - R_0 R_{L_c} G_{L_c}^{\,2})}[P_I + R_0 R_{L_c} G_{L_c}(G_{L_c} - 1)\overline{P}_{sp} + R_0(G_{L_c} - 1)\overline{Q}_{sp}] \qquad \text{(A3.19)}$$

$$Q_0 = R_{L_c} G_{L_c}^{\,2} P_0 + R_{L_c} G_{L_c}(G_{L_c} - 1)\overline{P}sp + (G_{L_c} - 1)\overline{Q}_{sp} \qquad \text{(A3.20)}$$

$$G_{L_c} = \exp(\overline{g} L_c)$$

where P_I is a constant related to the photon density at $z = 0$ taken to be equal to one, and R_0 and R_L are facet reflectivities at $z = 0$ and $z = L$ respectively. Finally the values for $\overline{P}(\overline{N})$ and $\overline{Q}(\overline{N})$ are calculated and substituted into the charge conservation equation (A3.12), given below.

$$\underbrace{\frac{J_0}{qd}}_{A} = \underbrace{\frac{\overline{N}}{\tau_{sp}} + \widetilde{g}(\overline{N})[\overline{P}(\overline{N}) + \overline{Q}(\overline{N})]}_{B} \qquad \text{(A3.12)}$$

where

$$J_0 = \frac{I_{inj}}{W.L_c} \qquad \text{(3.2)}$$

and

$$\overline{P}(\overline{N}) = \frac{1}{L_c}\int_0^{L_c} P(z,\overline{N})\,dz \qquad \text{(A3.13)}$$

$$\overline{Q}(\overline{N}) = \frac{1}{L_c}\int_0^{L_c} Q(z,\overline{N})\,dz \qquad \text{(A3.14)}$$

In the equations above J_0 is the current density taken to be constant along the length, I_{inj} is the injected current, W is the width and L_c is the length of the stripe contact. In the model the current density is assumed to be constant throughout the rectangular striped contact region and to remain so throughout the different layers of the double heterostructure material. Therefore for a given current, I_{inj}, term A in equation (A3.12) is a constant. In the simulation new values for $\overline{P}(\overline{N})$ and $\overline{Q}(\overline{N})$ are calculated with different values of $\overline{N}$ until term B equals to that of term A in

equation (A3.12). Having found the self consistent value of $\overline{N}$, it is then substituted into equations (A3.17) and (A3.18) to give the photon distribution $P(z,\overline{N})$ and $Q(z,\overline{N})$ at several points along the length. These values are then stored and is subsequently used to calculate the variable carrier distribution N(z) given by:

$$N(z) = \left[\frac{J_0}{qd} - \tilde{g}(\overline{N})(P(z,\overline{N}) + Q(z,\overline{N}))\right] \bullet \tau_{sp} \tag{3.3}$$

3.3 Simulation Results - Theoretical

A number of PSLDs have been simulated to study the longitudinal distribution of photons and carriers in the device. A diagram to explain the notation used in this section is shown in Figure 3.3. In all the simulations the devices had stripe width W = 50μm. Table 3.1 contains the relevant parameters used in the simulation. The simulation results are divided into two main categories; i) the longitudinal distribution of photons and carriers at low and high current densities and ii) the light output characteristic from the cleaved end face R_{L_c} and from the other end of the stripe R_0.

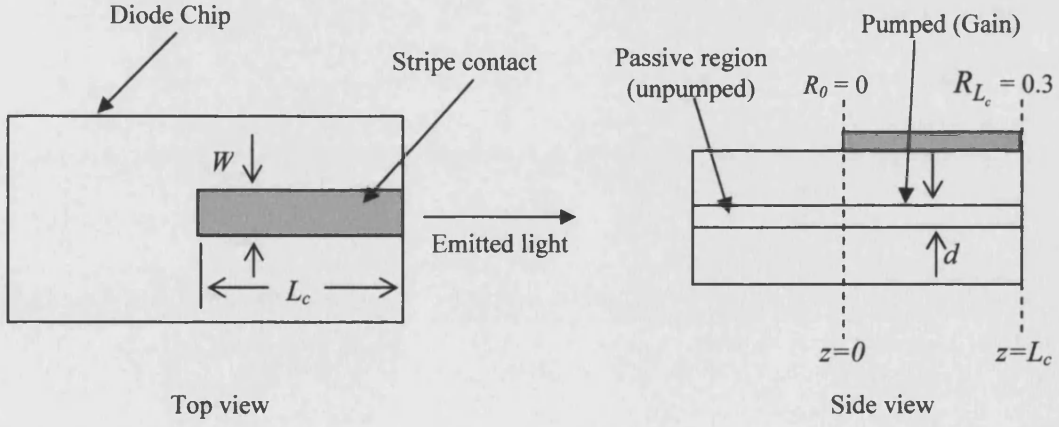

Figure 3.3: Schematic diagram of a parallel stripe SLD from the top and side, showing the notations used in this section.

Abbreviation	Parameter	Value
R_{L_c}	front facet reflectivity	0.3
R_0	back facet reflectivity	0.0
B_r	bimolecular recombination constant	1.0×10^{-10} cm^2s^{-1}
Γ_v	Vertical confinement factor	0.74
D	active layer thickness	0.3μm

Table 3.1: Relevant parameters used in the simulation

3.3.1 Longitudinal Photon and Carrier Distribution

Figure 3.4 shows a plot of the photon density distribution of forward 'P' and reverse 'Q' traveling photons for low current density, J_0 = 1100A/cm^2. The carrier density distribution is also plotted on the same graph for comparison. The vertical scale of the graph is arbitrarily normalized so that the maximum photon and carrier density becomes unity. A rough approximated value for the carrier density $\overline{N}$ can be obtained from equation (2.16) given in Chapter 2. Ignoring the effects of current spreading and carrier diffusion such that $J_y(x) = J_0$ and $D = 0$, equation (2.16) is rearranged to give:

$$\overline{N} = \sqrt{\frac{J_0}{qdB_r}} \tag{3.4}$$

and from equation (A3.3) the material gain can be written as:

$$\tilde{g}(\overline{N}) = \alpha_0 \left(\sqrt{\frac{J_0}{qdB_r}} - N_T \right) \tag{3.5}$$

Hence in the case for J_0 = 1100 A/cm^2, the material gain $\tilde{g}(\overline{N})$ = -4.44cm^{-1}, which means that the active medium is slightly lossy. It can be seen from Figure 3.4 that there is a build up of photon density in the direction of travel for both forward 'P' and reverse 'Q' traveling photons. This build up is attributed to the summation of the photons that are spontaneously emitted along the longitudinal direction. It is however not due to the amplification of spontaneous emission in the medium since

$\tilde{g}(\overline{N})$ is negative. Note that the carrier density distribution is flat at low current densities.

Figure 3.5 shows a plot of photon and carrier distribution for high current density, J_0 = 6000A/cm^2 with $\tilde{g}(\overline{N})$ = 220cm^{-1}. The plot shows that the photon density distribution inside the device at high current densities is very asymmetric. The photon density at $z = L_c$ for the forward traveling photons 'P' is very much smaller than the photon density for the reverse traveling photons 'Q' at z = 0. This is a natural consequence of the boundary condition of the SLD since the front facet reflectivity, R_{L_c} = 0.3 provides a much larger initial value for 'Q' at $z = L_c$ than for 'P' at z = 0 with R_0 = 0. As a result the reverse traveling photons 'Q' attains a much larger value than 'P', due to amplification of spontaneous emission, as it reaches z = 0. The growth of the reverse traveling photons 'Q' becomes so large that it significantly depletes the carriers in the rear of the SLD as shown by the carrier distribution plot. As a consequence the material gain is also reduced since it is a function of the carrier inversion population. Hence, it is evident from the simulation that the growth rate of the forward traveling photons at high current densities is greatly reduced due to hole-burning effect.

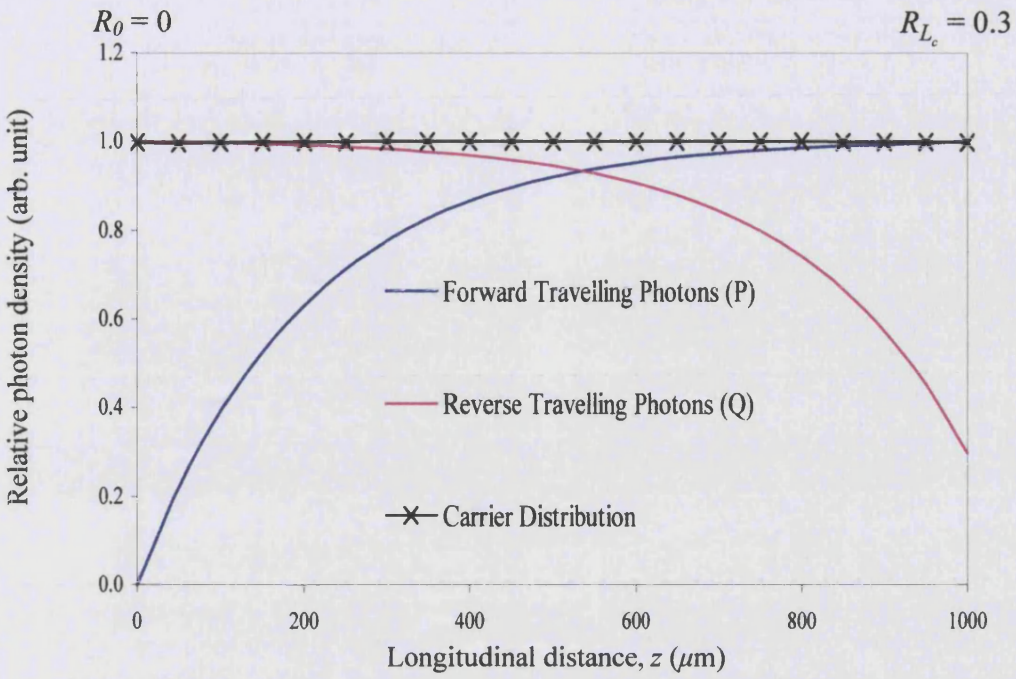

Figure 3.4: Carrier and photon density distribution of forward and reverse traveling photons in the PSLD for low current density, $J_0 = 1100\text{A/cm}^2$. $W = 50\mu\text{m}$ and $L_c = 1000\mu\text{m}$.

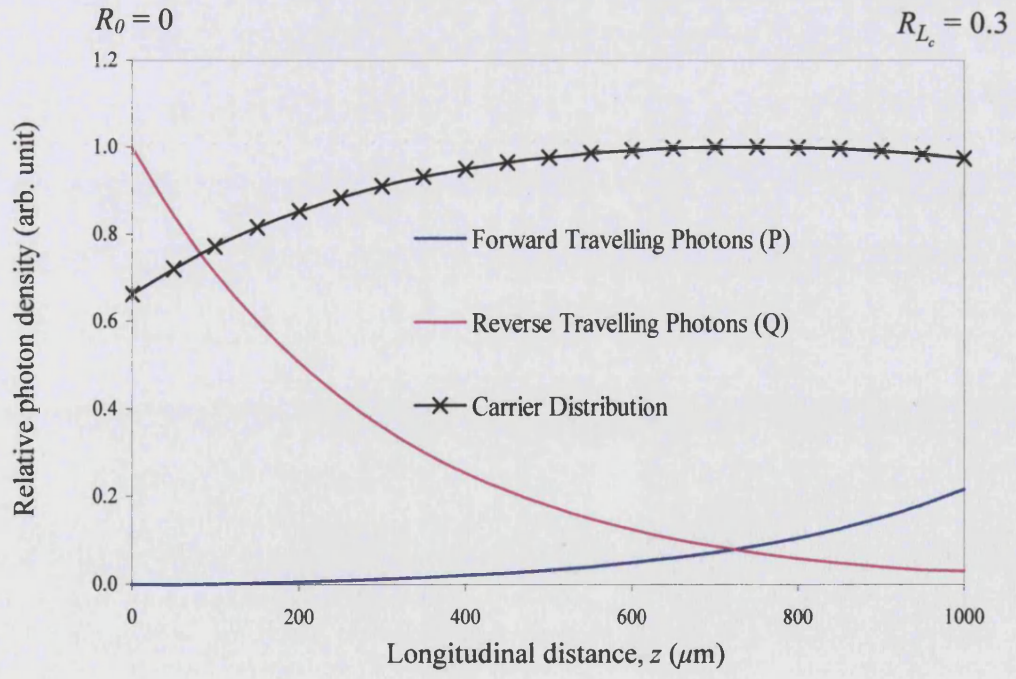

Figure 3.5: Carrier and photon density distribution of forward and reverse traveling photons in the PSLD for high current density, $J_0 = 6000\text{A/cm}^2$. $W = 50\mu\text{m}$ and $L_c = 1000\mu\text{m}$.

3.3.2 Light-Current Characteristic

The photon density distribution inside the SLD is essentially of academic concern however the output power that can be collected from the output facet is also of interest. Figure 3.6 and 3.7 shows a comparison of the output power from the cleaved end facet with the power that is lost from the rear end facet, versus current density for two different lengths L_c. Simulations were made for the case $R_0 = 0$ and $R_{L_c} = 0.3$. The plot shows that the amount of power that escapes uselessly into the back passive region is much greater than that is accessible at the cleaved end facet. A SLD with $L_c = 1000\mu m$ at $J_0 = 8000 A/cm^2$ delivers ~ 60mW at the cleaved end but losses almost 20 times as much power into the back passive region. Even for a shorter SLD with $L_c = 500\mu m$ at $J_0 = 14000 A/cm^2$, the ratio is still about 1 to 10, shown in Figure 3.7.

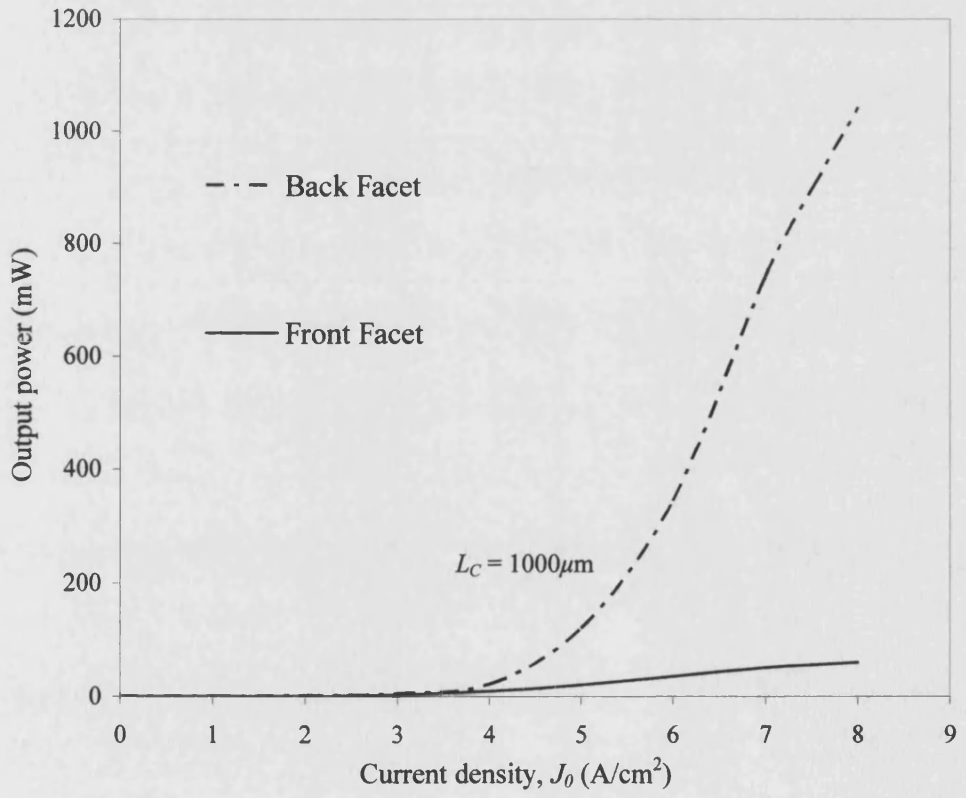

Figure 3.6: Output power from the cleaved end facet and from the back end facet for device with $W = 50\mu m$ and $L_c = 1000\mu m$. $R_0 = 0$ and $R_{L_c} = 0.3$.

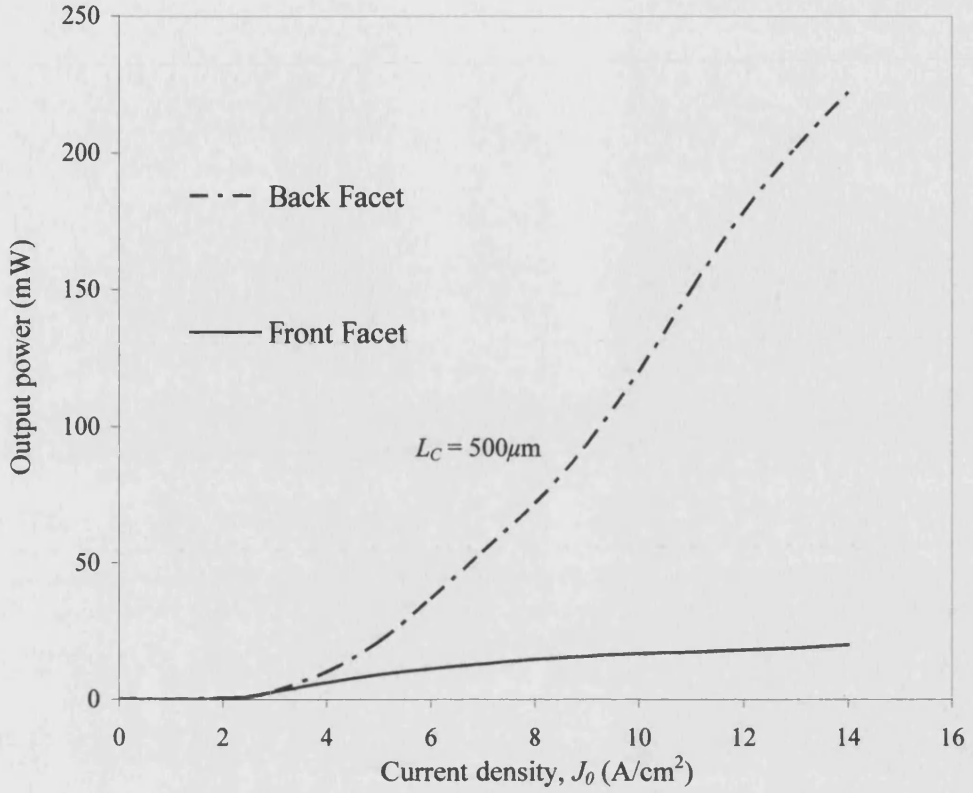

Figure 3.7: Output power from the cleaved end facet and from the back end facet for device with $W = 50\mu m$ and $L_c = 500\ \mu m$. $R_0 = 0$ and $R_{L_c} = 0.3$.

3.4 High Power SLD Design Consideration

In its simplest configuration the stripe SLD has almost zero reflectivity at its far end at $z = 0$ and finite reflectivity at $z = L_c$, at its output end. However, simulation results of the photon and carrier distribution given in Figure 3.5 show that the reflected power from the front facet ($z = L_c$), in particular at high levels of current density causes severe carrier depletion to occur at the rear of the device. Consequently, the growth of the forward traveling photons that delivers the output power is very much reduced. Also, the light-current characteristic given in Figure 3.6 show that a device with high reflectivity at the output end causes more power to reflect back into the device and is dumped uselessly into the back passive region than is available at the output. Therefore operating the SLD with a cleaved output end, with $R_{L_c} = 0.3$, results in the least favorable design.

Hence, it is evident from the simulation results shown in section 3.3 that a more efficient SLD operational characteristic could be achieved if a highly reflecting mirror could be placed at $z = 0$ (i.e. back end facet R_0) and the front end reflectivity R_{L_c} almost zero. However the drawback with this method, as has been discussed in Chapter 1 in section 1.3, is that very high quality multilayer A-R coatings ($R \sim 10^{-6}$) at the front facet are needed to inhibit lasing. Unfortunately, multilayer A-R coatings require complex and often expensive fabrication techniques.

Conversely, high output powers can be obtained from SLDs if facet reflectivities of both front and back (real or effective), could be reduced and optical feedback into the device suppressed. The simplest method to reduce reflectivity at the back end, R_0, is by terminating the stripe contact before it reaches the edge of the chip [5], thereby creating an absorbing region. However, it is worth mentioning here that at high levels of electrical pumping the absorbing region can be optically pumped to transparency and lasing does occur with self sustained oscillations as seen in tandem laser structures [6]. Some of the simplest method that have been used to reduce the front end facet reflectivity is by applying anti-reflection coating [7] or by inclining

the stripe contact at angle with respect to the normal of the output facet [8]. In this section, the effect of reducing the front facet reflectivity, R_{L_c}, has on the operational characteristic of the SLD is investigated. Simulation results are shown in Figure 3.8 and 3.9 respectively. In addition, the effect of changing the length of the device is also investigated and results are shown in Figure 3.10.

Figure 3.8 shows a plot of photon and carrier distribution for high current density, $J_0 = 6000\text{A/cm}^2$ with front facet reflectivity $R_{Lc} = 0.01$. Simulation was for a device with $W = 50\mu\text{m}$ and $L_c = 1000\mu\text{m}$. The plot shows that the photon distribution in the device is now more symmetric compared to the photon distribution plotted in Figure 3.5. More importantly the carrier density distribution after the reduction of the front facet reflectivity is flat without a dip at the rear of the device, which is characteristic of hole-burning effect.

Figure 3.9 shows the corresponding output power versus current density before and after the reduction of R_{Lc}, for a device with $W = 50\mu\text{m}$ and $L_c = 1000\mu\text{m}$. At low current densities there is little difference between the device with $R_{Lc} = 0.3$ and the device with $R_{Lc} = 0.01$. However, at high current densities the output power from the device with $R_{Lc} = 0.01$ is increased by as much as four times compared to the device with $R_{Lc} = 0.3$. A comparison of the carrier density distribution plot in Figure 3.5 and in Figure 3.7, for $J_0 = 6000\text{A/cm}^2$, confirms that the rise in output power arises from the reduction in carrier depletion at the rear of the device. This method of increasing the output power is by far the simplest with no extra drive current needed.

It is also possible to combine the reduction in output facet reflectivity with an increase in stripe length to obtain an even larger increase in output power. Figure 3.10 shows a plot of output power versus stripe contact length L_c, of a device with $W = 50\mu\text{m}$ for $J_0 = 6000\text{A/cm}^2$.

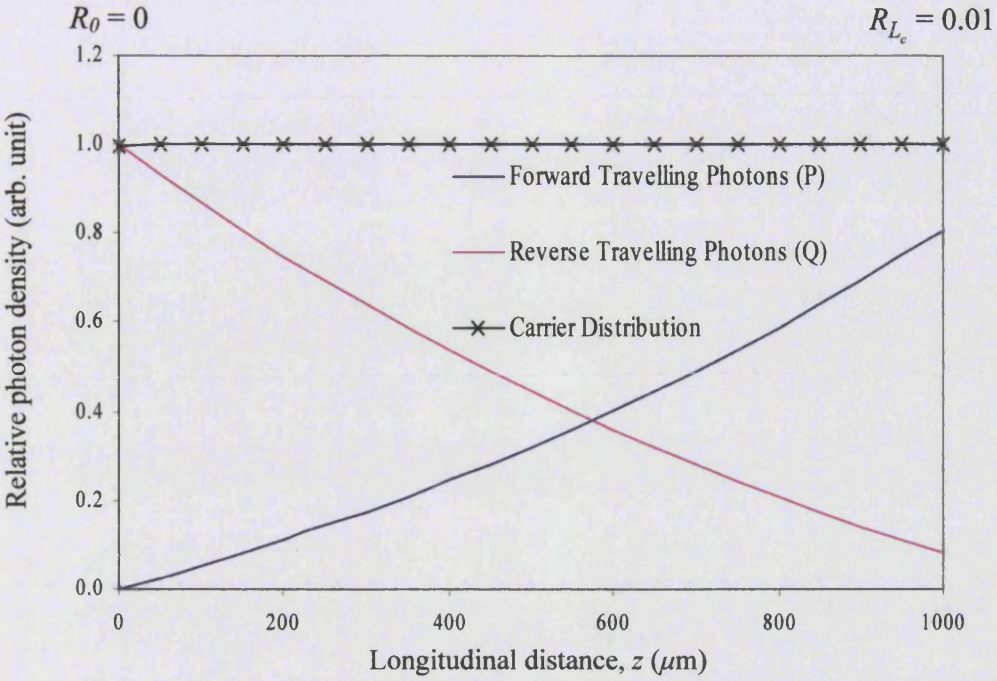

Figure 3.8: Carrier and photon density distribution of forward and reverse traveling photons in the PSLD for $J_0 = 6000$A/cm^2 with $R_{L_C} = 0.01$. $W = 50\mu$m and $L_c = 1000\mu$m

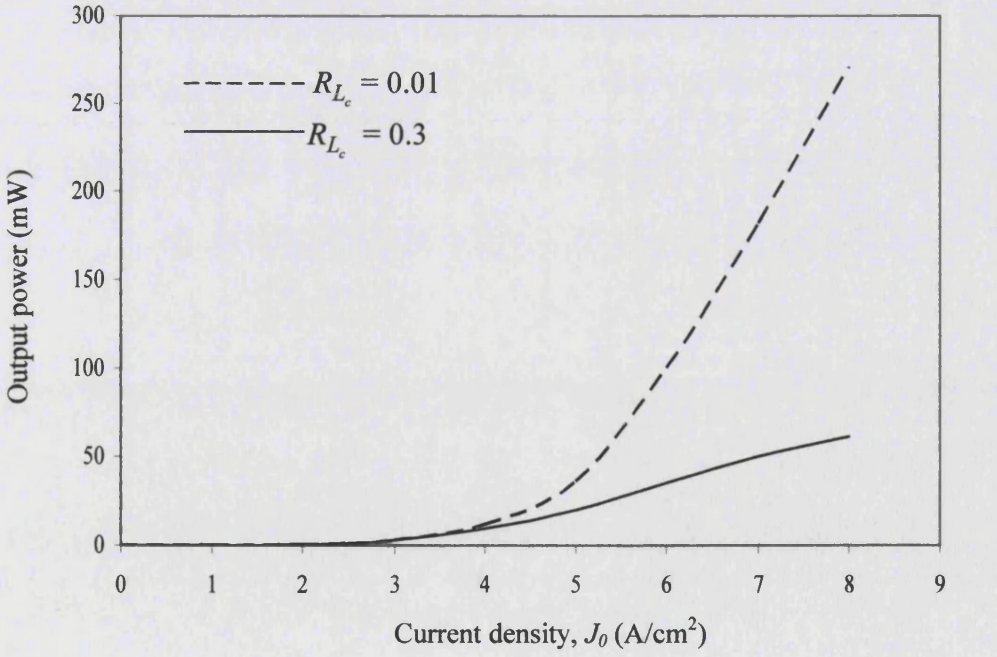

Figure 3.9: Output power versus current density for $R_{L_C} = 0.3$ and $R_{L_C} = 0.01$. $W = 50\mu$m and $L_c = 1000\mu$m.

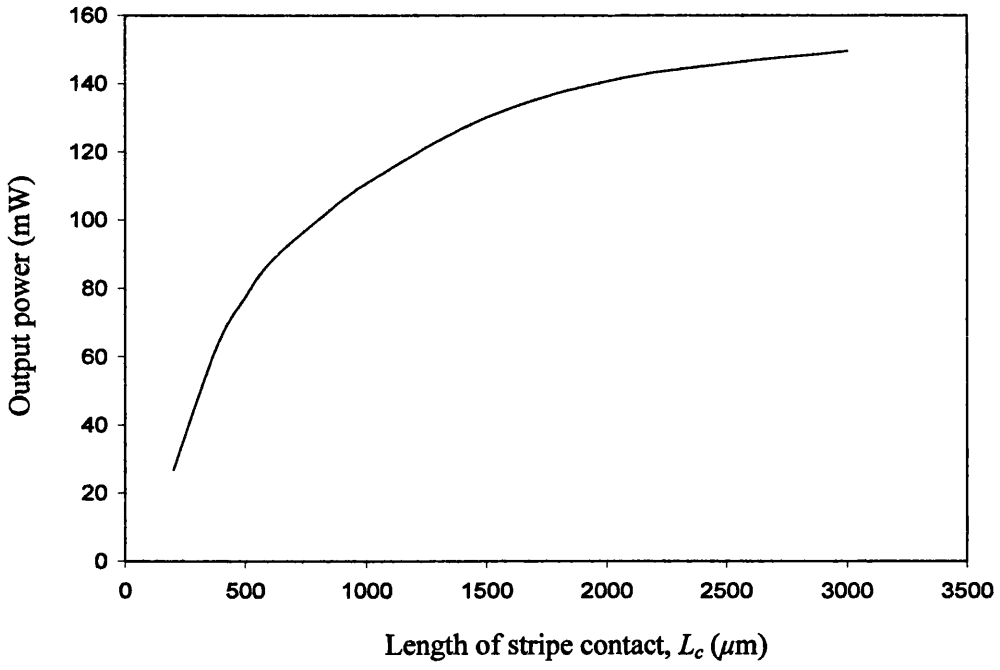

Figure 3.10: Plot of output power versus contact length L_c, for $R_0 = 0$ and $R_{L_c} = 0.01$. $W = 50\mu$m and $J_0 = 6000$A/cm^2.

3.5 Experimental Results

The light-current (L-I) characteristics of a number of PSLDs were measured. Devices were made from semiconductor bulk material QT503A. The specification for this material can be found in Appendix 2A. The devices all had 1000μm long stripe contact with 50μm wide output facets. Devices were mounted p side down on copper heat sinks and were measured with 4μs pulses and a 250:1 duty cycle. The experimental technique used to measure the light-current characteristic of the devices are detailed in Appendix 3B.

Figure 3.11 shows a comparison of the measured output power versus current density for devices UB1036 and UB1037 with those predicted from theory. It can be seen from the plot that a reasonable match has been obtained. However the theoretical curves have higher slope efficiency than the experimental curves. This could be due to the fact that current spreading, carrier diffusion and loss terms such as nonradiative recombination was not included in the model.

It was shown in Figure 3.9 that when the output facet reflectivity is reduced from 0.3 to 0.01 an increase in output power by as much as four times was observed. Hence, a single layer of anti-reflection (A-R) coating of about 2% was applied to the output facet of UB1037. The light-current characteristic of this device was re-measured and compared with that before A-R coating. The curves plotted in Figure 3.12 show that as much as four times increase in output power has been obtained at about J_0 = 5000A/cm2 after A-R coating compared to before A-R coating.

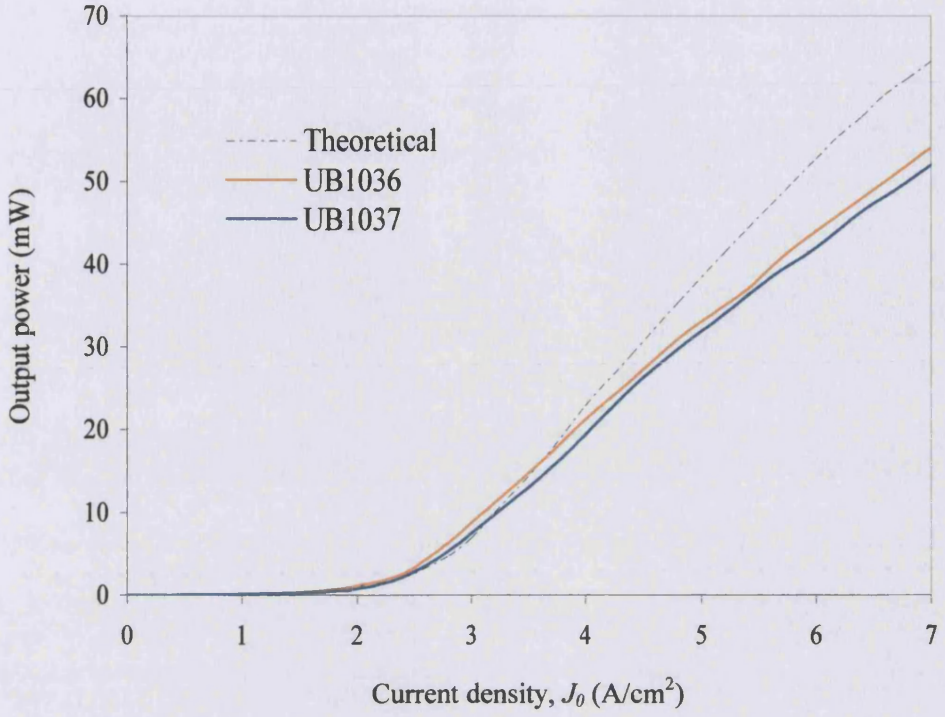

Figure 3.11: A comparison of the calculated and measured L-I characteristic of UB1036 and UB1037, before A-R coating.

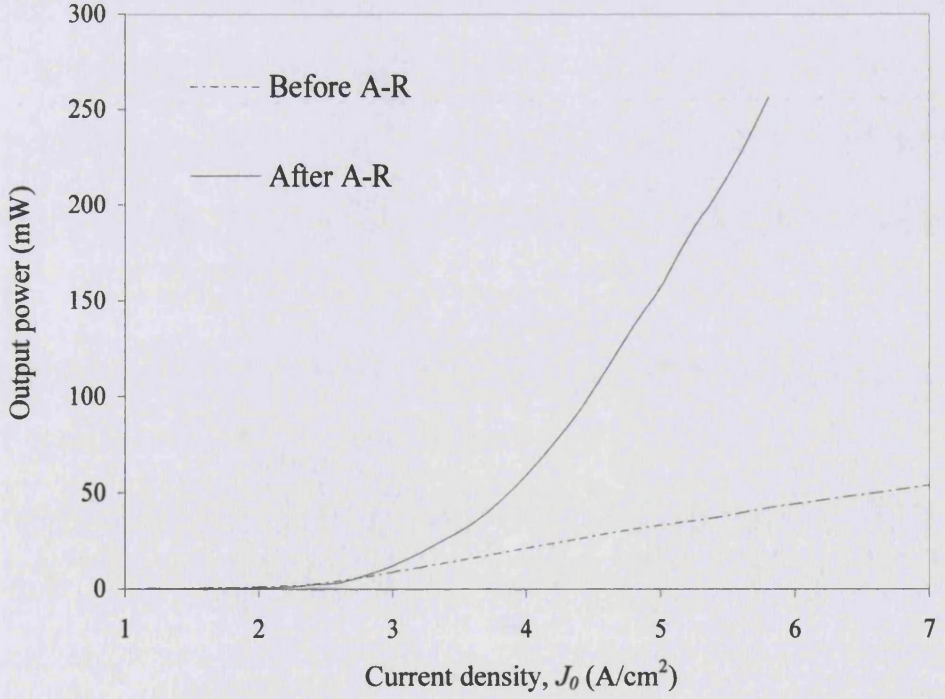

Figure 3.12: A comparison of the L-I characteristic of UB1037 before and after A-R coating.

3.6 Conclusions

A simple one dimensional model, using the constant N method, of parallel stripe SLDs that simulates the L-I characteristic and photon distribution has been developed. Also, the model has been extended to include optically induced carrier depletion. This new feature has not only enabled a direct visualisation of the longitudinal distribution of carriers but also hole-burning effects that occur at high levels of pumping. Furthermore, it has been possible to simulate SLDs with different values of front facet reflectivities to investigate the effect this had on the longitudinal distribution of carriers in the device.

Simulation results given in Figure 3.6 and 3.7, show that the amount of power that escapes uselessly into the back passive region is far greater than that is accessible at the output facet for an SLD with a finite front facet reflectivity. In addition, with reference to Figure 3.5, at high levels of pumping, the reflected power severely depletes the carrier at the rear of the device. This in turns limits the available output power from the device. Simulation and experimental results have shown that this problem is easily overcome by reducing the front facet reflectivity, i.e. applying anti-reflection coating on the front facet. This technique has not only reduced the effect of carrier depletion but also increased the output power many times over. However, it is important to note that reduced front facet reflectivity alone is not enough to ensure efficient SLD operation. The back facet reflectivity must also be low enough to prevent optical feedback from occurring, since power reflected back and forth can cause the device to break into laser oscillation.

In conclusion, the key requirement to obtaining high output powers from SLDs is low facet reflectivities both front and back. However, achieving low facet reflectivities is a challenging task, although high quality A-R coatings of the order of 10^{-6} has been achieved, it however involves complicated and expensive fabrication techniques. Thus, alternative methods to reduce facet reflectivities (front and back) that are simple and cost effective have been investigated and are presented in the following chapter.

References

[1] H. *Kressel and J. K. Butler*, **'Semiconductor Lasers and Heterojunction LEDs'**, New York: Academic, p. 556, 1977.

[2] *W. Streifer, D. R. Scifres and R. D. Burnham*, **'Analysis of Gain Induced Waveguiding in Stripe Geometry Diode Lasers'**, IEEE Journal of Quantum Electron, Vol. QE-14, No. 6, p. 418, June 1978.

[3] *M. J. Adams and M. Osinski*, **'Longitudinal Mode Competition in Semiconductor Lasers. Rate Equations Revisited'**, IEE Proceedings, Vol. 129, No. 6, p. 271, 1982.

[4] *M. C. Amann and J. Boeck*, **'High Efficiency Superluminescent Diodes for Optical-Fibre Transmission'**, Electron. Letters, Vol. 15, pp. 41-43, 1974.

[5] *T. P. Lee, C. A. Burrus. Jr., B. I. Miller*, **'A Stripe-Geometry Double-Heterostructure Amplified-Spontaneous-Emission (Superluminescent) Diode'**, Journal of Quantum Electron, Vol. QE-9, p. 820, 1973.

[6] *N. G. Basov*, **'Dynamics of Injection Lasers'**, IEEE Journal of Quantum Electron., Vol-QE4, p. 855.

[7] I. *P. Kaminow, G. Eisenstein, L. W. Stutz, P. P. Dentai*, **'Lateral Confinement InGaAsP Diode at 1.3μ'**, IEEE Journal of Quantum Electron., Vol QE-19, pp. 78-81, 1983.

Chapter 4
Tapered Superluminescent Diodes

4.1 Introduction

It was concluded in Chapter 3 that the key requirement to obtaining high output powers from superluminescent diodes (SLDs) is low facet reflectivities (front and back). High facet reflectivities both front and back in SLDs accentuate optical feedback, which results in lasing to occur. Removing only the back facet reflectivity will eliminate optical feedback but unfortunately problem still remains. Simulation results presented in section 3.2 of Chapter 3 have shown that devices with high front facet reflectivity, especially at high levels of pumping, suffer from severe depletion of carriers at the rear of the device. As a result gain is reduced and consequently the available output power from the device is limited. Therefore, for high power SLD operation, low facet reflectivities of both facets must be maintained to avoid the problems mentioned above.

Many research groups in the past have used complex and often expensive fabrication techniques to achieve the required low facet reflectivities. In this chapter a new structure for high power SLD operation which incorporates a two-dimensional etched deflector is described. This new design meets the above requirement but has an additional advantage over other SLD designs mentioned in Chapter 1, as it is cheap and simple to fabricate. Also to note from the literature review (Chapter 1), is that high output powers have been obtained form tapered geometry devices. It was reported in [1], [2] that devices with these structures demonstrate high output power saturation compared to broad area devices. The desirable feature mentioned above lead to the design and development of tapered geometry SLDs (TSLDs).

The experimental results of the characterisation of TSLDs are contained in this chapter. The effect of the etched deflector, anti-reflection coating and different taper flare angles on the performance of the device are presented and discussed. Finally, the light-current characteristic of parallel stripe SLDs and tapered SLDs are compared.

4.2 Tapered SLD Structure with Novel Etched Deflector

A number of TSLDs with deflectors were fabricated from bulk material QT543R. The specification for this material can be found in Appendix 2A. The taper is in the form of a shallow ridge produced by ion-beam etching (etch depth = 0.9μm) which is designed to reduce current spreading but produces only negligibly small lateral index guide. Deflectors were etched through the active layer and lower cladding layer to a depth of 6μm. Figure 4.1 shows a schematic of one of these devices.

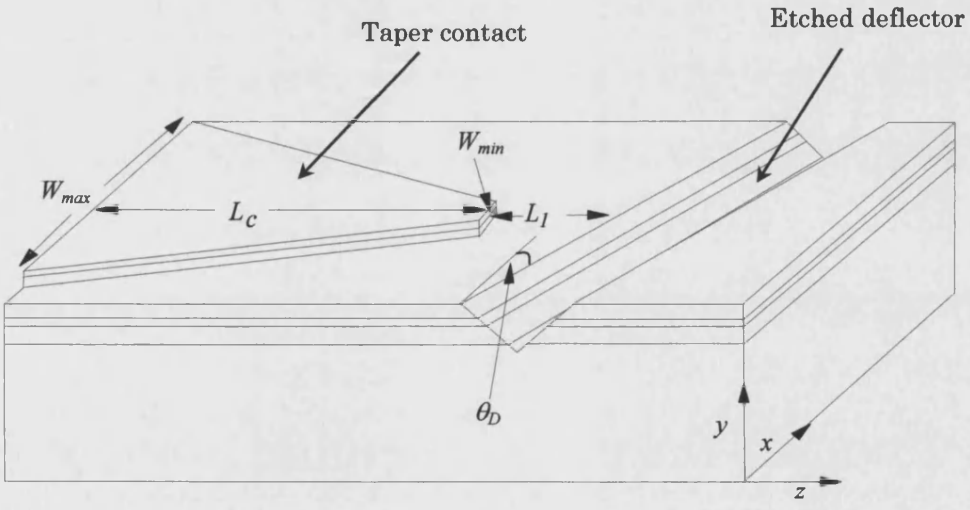

Figure 4.1: Schematic diagram of the TSLD with a 'V' groove etched deflector incorporated in the rear of the device.

Figure 4.2a and 4.2b illustrates how the deflector works. The 'V' groove etched deflector as shown in Figure 4.2a is inclined at an angle, $\theta_D = 10°$ to the horizontal (x) axis. This is to prevent any reflections that occur due to changes of index between the cladding layer/substrate boundary, or from the substrate/metal boundary, from re-entering the active region. The 'V' groove deflector is also inclined at an angle 45° to the vertical axis (y) axis, Figure 4.2b. This is to deflect photons away from the transverse (y direction) multi-layer waveguide and into the substrate where it is efficiently absorbed. Details of the deflector fabrication can be found in Appendix 4A.

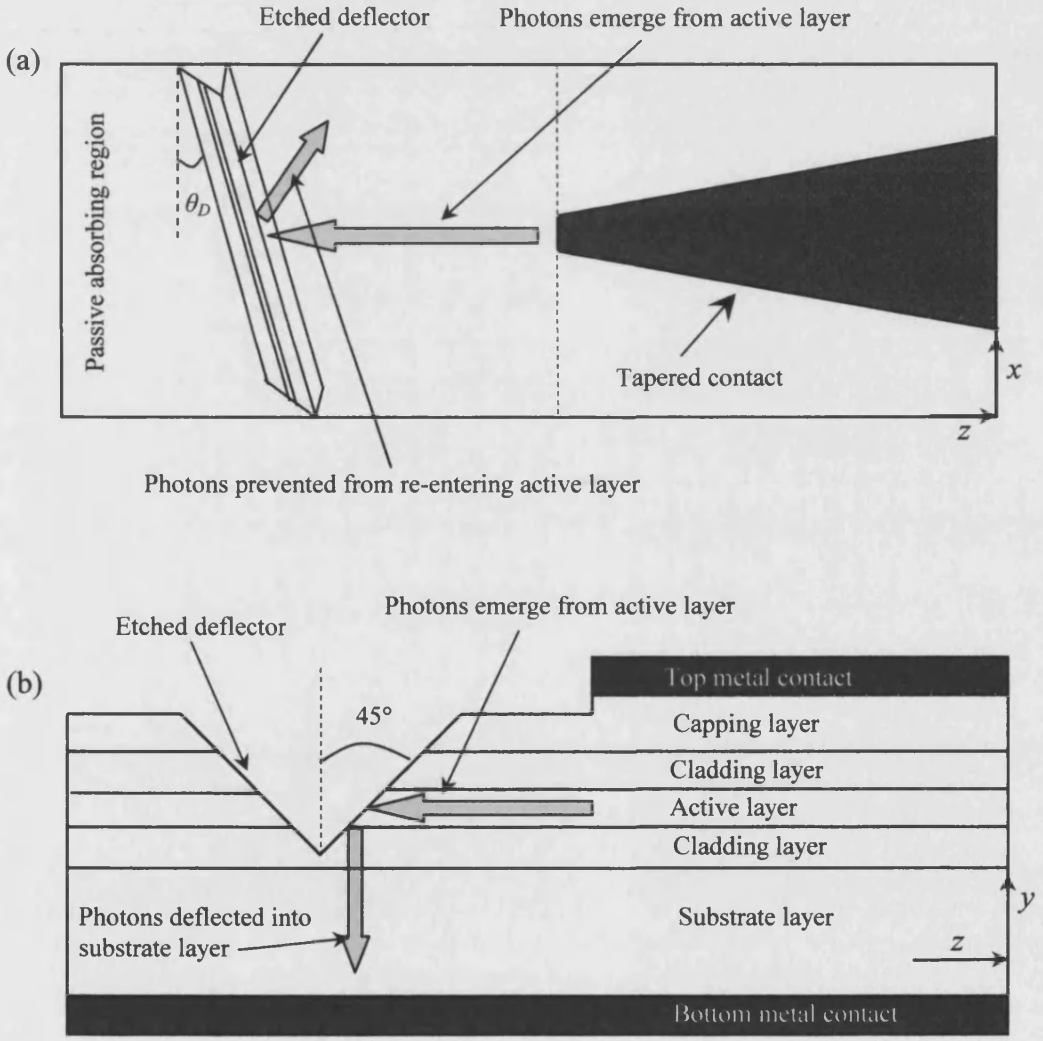

Figure 4.2: Schematic diagram of a tapered SLD with a two-dimensional etched deflector in the absorbing region. (a) top view, showing the deflector axis inclined at 10° with respect to the x axis. (b) side view, showing the deflector walls inclined at 45° with respect to the y axis.

4.3 Experimental Results

A number of TSLDs were fabricated and measured. The devices were mounted p^+ side up on copper heat sinks with Indium solder and tested with 2μs pulses and a duty cycle of 10:1. Several devices were also fabricated without deflectors to investigate the ability of the etched back deflector in reducing optical feedback. The experimental technique used for the following measurements are detailed in Appendix 3B. Table 4.1 contains descriptions of the devices measured.

Device Number	UB763A	UB763B	UB766A	UB766B
Wide facet, W_{max} (μm)	100	100	100	100
Narrow facet, W_{min} (μm)	5	5	5	5
Taper Contact Length, L_c (μm)	1000	1000	1000	1000
Deflector	Yes	No	Yes	Yes
Deflector distance, L_1 (μm)	500	---	100	200

Table 4.1: Dimensions of TSLDs used in the measurement.

4.3.1 The Effect of the Etched Deflector

Two devices were fabricated with and without the etched back deflector in order to investigate its ability in suppressing lasing. Figure 4.3 shows a plot of output power against current for these devices. The solid curve represents the TSLD with a deflector (UB763A) and the dashed curve represents the TSLD without a deflector (UB763B). Results show that the device without the etched back deflector (UB763B) reached lasing threshold at about 1.7A of current. Further evidence of this can be seen in the near-field intensity profiles, measured below and above 1.7A, given in Figure 4.4. Well before the onset of lasing the near-field profile is broad covering

the whole width of the output facet. However, above 1.7A, the near-field intensity profile is much narrower with a series of troughs and peaks, indicating the presence of higher-order modes.

Conversely the TSLD with the etched back deflector (UB763A) did not exhibit any lasing characteristic up to 3.2A of current. The measured near-field intensity profiles plotted in Figure 4.5 are stable and broad at several currents. This proves that the etched back deflector is very effective in reducing optical feedback and suppressing lasing.

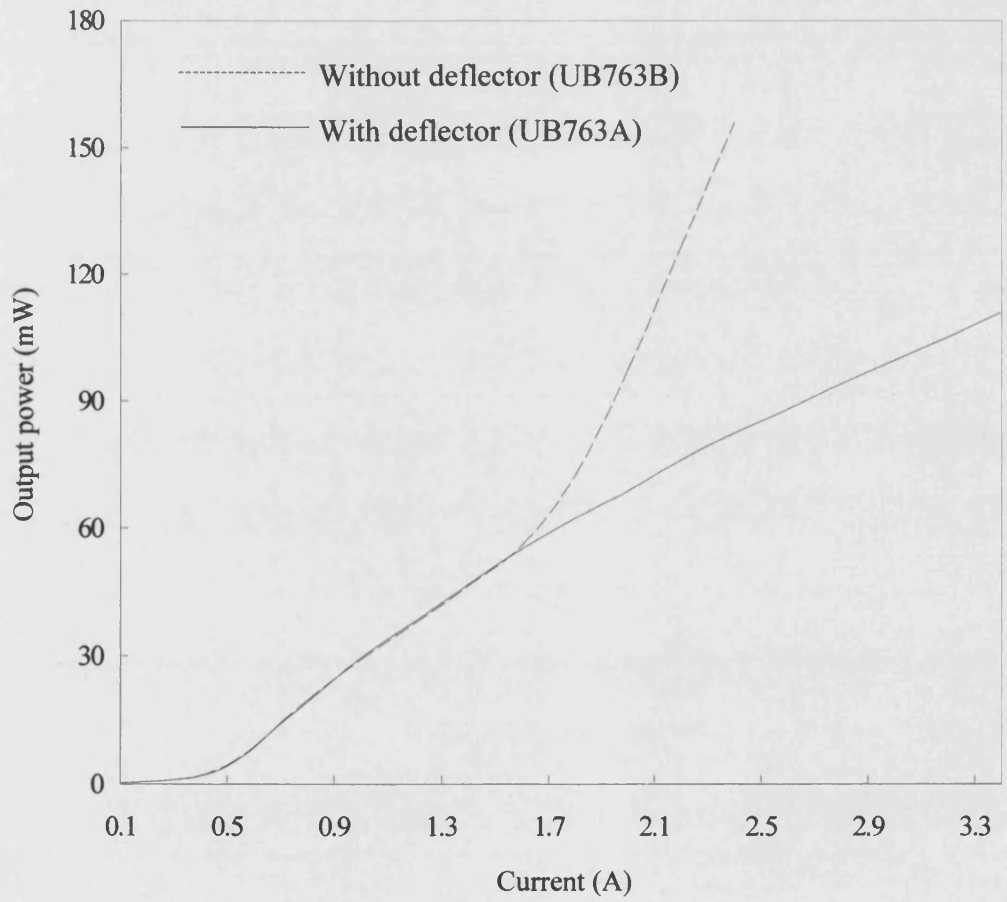

Figure 4.3: Measured light-current (L-I) characteristics of devices UB763A with a deflector and UB763B without a deflector.

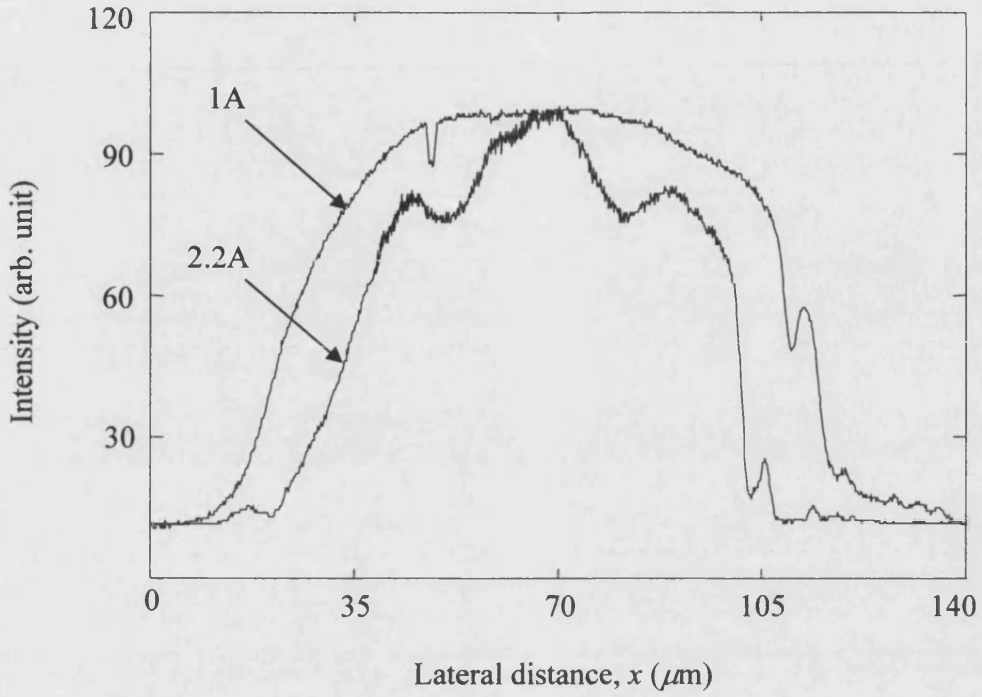

Figure 4.4: Near-field profiles of UB763B without etched deflector measured at 1.0A and 2.2A of current.

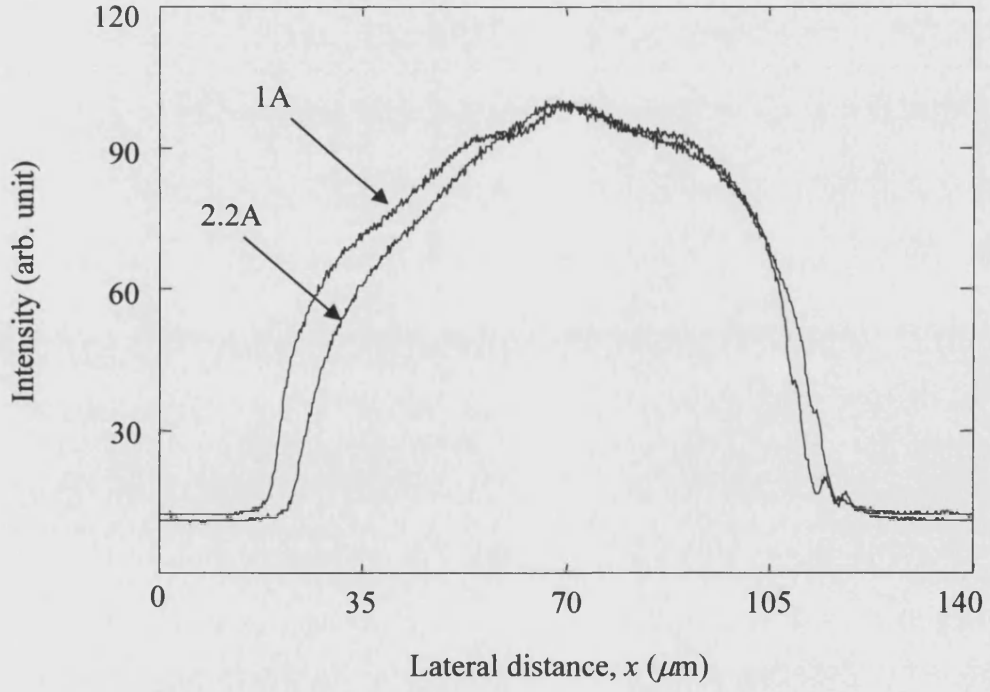

Figure 4.5: Near-field profiles of UB763A with etched deflector measured at 1.0A and 2.2A of current.

4.3.2 *The Effect of Varying Deflector Distance L_1*

The effects of varying the deflector distance L_1, shown in Figure 4.6, on the electrical efficiency of the TSLDs are investigated. The devices all had W_{max} = 100μm, W_{min} = 3μm and L_c = 1000μm. Three devices were measured and compared, which are:

i) UB766A – L_1 = 100μm
ii) UB766B – L_1 = 200μm
iii) UB763A – L_1 = 500μm

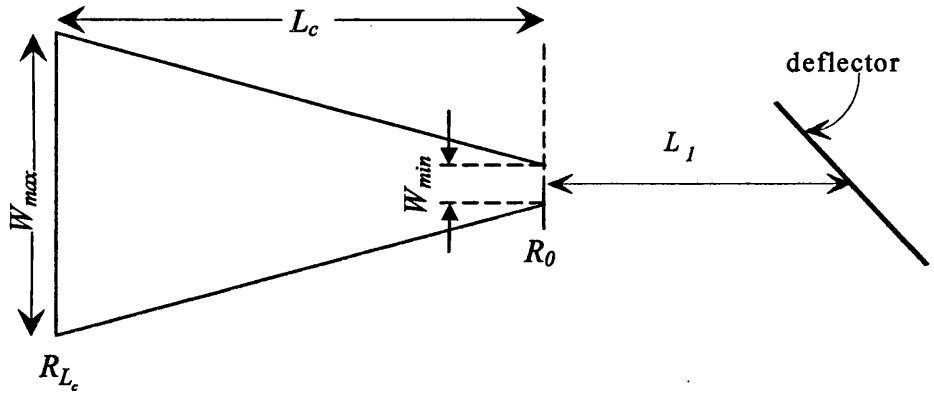

Figure 4.6: Schematic diagram of TSLD with etched back–deflector. L_2 is the distance between the deflector and the device.

Figure 4.7 shows a plot of output power against current for devices UB766A, UB766B and UB763A. At low currents there is little difference in output power that these devices yield. However at high currents, the difference becomes significant, with output power increasing with increase in L_1. Note, the front facets were not A-R coated. It was shown in the previous chapter that optical feedback from the front facet causes carrier depletion, due to large power densities occurring at the rear end of the device. Consequently, devices with long absorption region absorb more light which in turn reduces the power density at the rear of the device. Therefore, devices with long absorbing region are able to deliver more power than those with short absorbing region. More importantly, this exercise demonstrates that devices with an etched back deflector does not require excessively long absorption region to suppress lasing. This is an advantage since there is no wastage of material and devices can be made to be more compact in size.

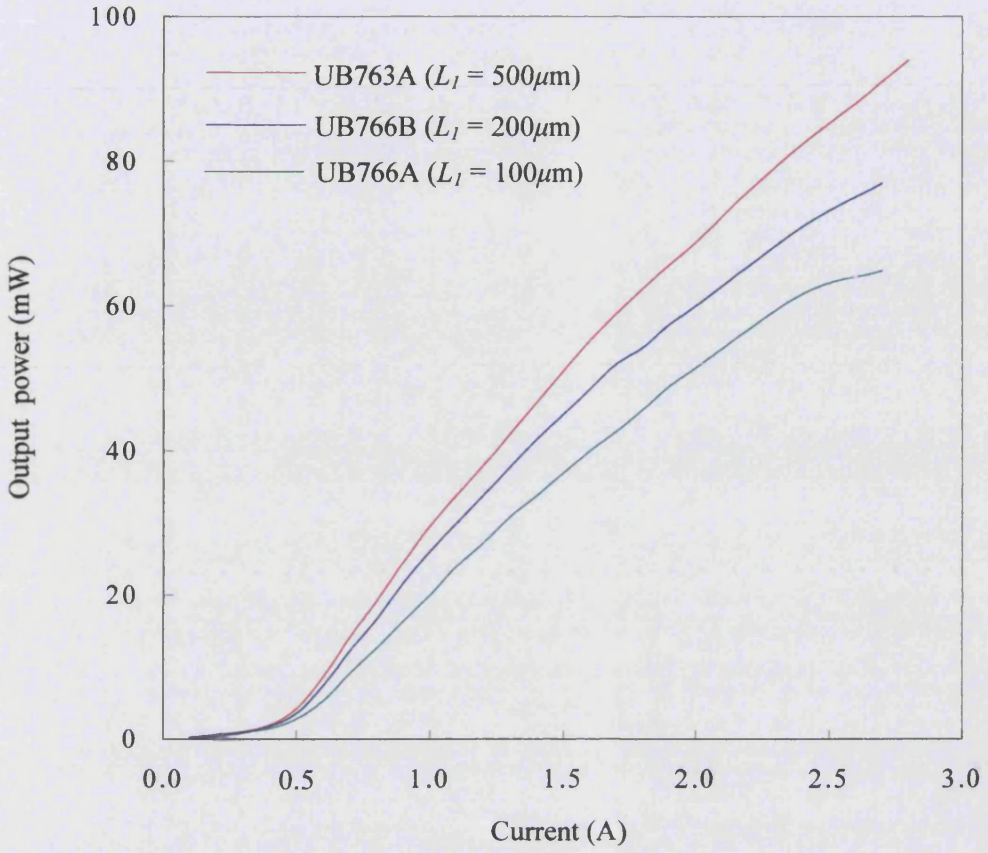

Figure 4.7: Measured light-current characteristics of devices UB763A (L_1=500μm), UB766A (L_1=100μm) and UB766B (L_1=200μm)

4.3.3 Anti-Reflection Coating on the Front Facet

- *Light-Current Characteristic*

Device UB763A was measured before and after the wide facets was A-R coated with a single layer of Zirconium Oxide/Titanium Oxide (ZrO_2/TiO_2). The wide facet was A-R coated to about 2% reflectivity. Figure 4.8 shows a plot of output power versus current before and after the wide facet was A-R coated. From the curves plotted it can be seen that after A-R coating as much as four times increase in power have been obtained with the device yielding over 500mW at about 4.5A of input current. At the time the research was conducted, this was reported to be the highest recorded power obtained from a SLD [3].

It has also been reported in the literature that by using a spherical lens to collimate the beam and a cylindrical lens to remove the astigmatism, coupling efficiencies into a single mode fibre of over 50% can be achieved from taper devices, [4], [5]. Therefore it is estimated that powers in excess of 250mW can be coupled into single mode fibres from the TSLDs described in this section.

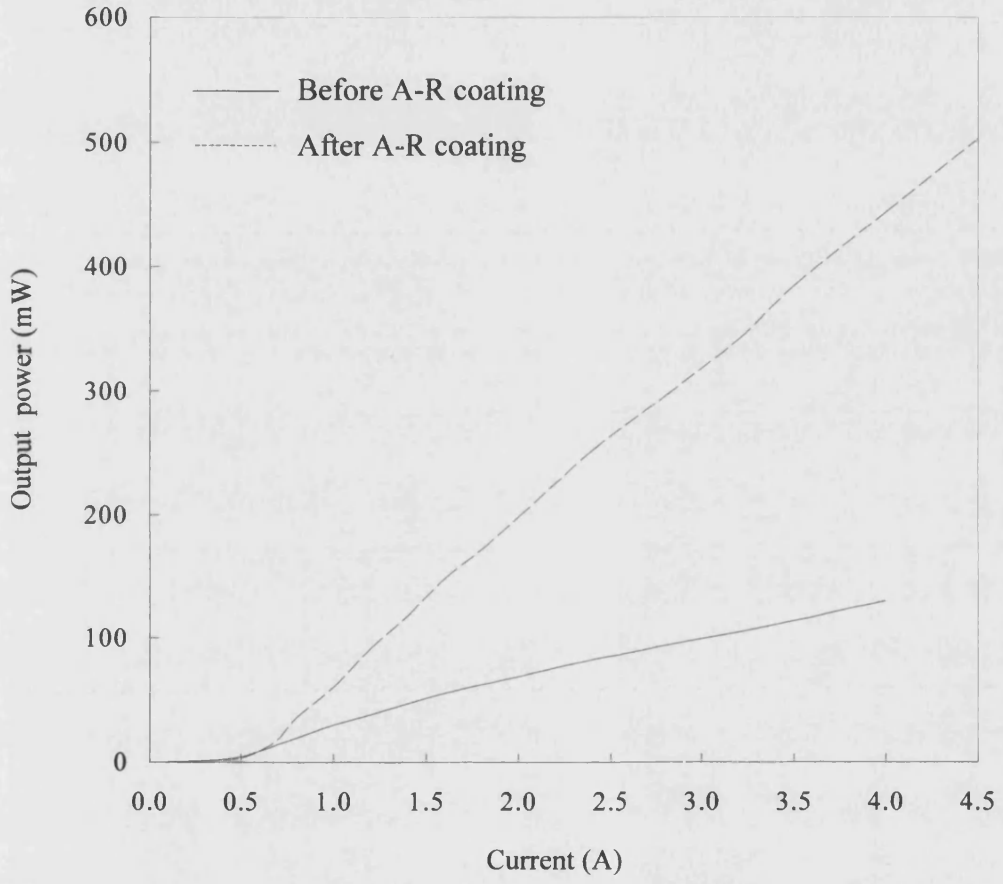

Figure 4.8: Measured light-current characteristics of device UB763A before and after A-R coating of the front facet.

- *Near-Field Intensity Distribution*

The near-field intensity profiles for UB763A were measured to investigate if there is any clear difference in the intensity distribution across the output facet before and after A-R coating. Figure 4.9 shows experimentally measured near-field profiles of device UB763A after A-R coating taken at several currents. Comparing Figure 4.5 (near-field before A-R coating) and Figure 4.9 one can see no significant difference in the measured near-field profiles obtained before or after A-R coating.

- *Far-Field Intensity Distribution*

The far-field intensity profiles for device UB763A were measured at several currents after A-R coating. The profiles obtained are shown in Figure 4.10. In general the far-field intensity profiles up to 3A of current had FWHM of ~ 56° narrowing slightly to FWHM ~ 50° at 4A of current. The narrowing of the far-field intensity profiles can be understood by considering that at high currents (high gain), the effective depth contributing to the output power is now the entire length of the device. Rays originating form the back of the device carry the most power and radiate over small angles (essentially parallel to the z axis). Hence, the observed decrease in far-field FWHM as current is increased.

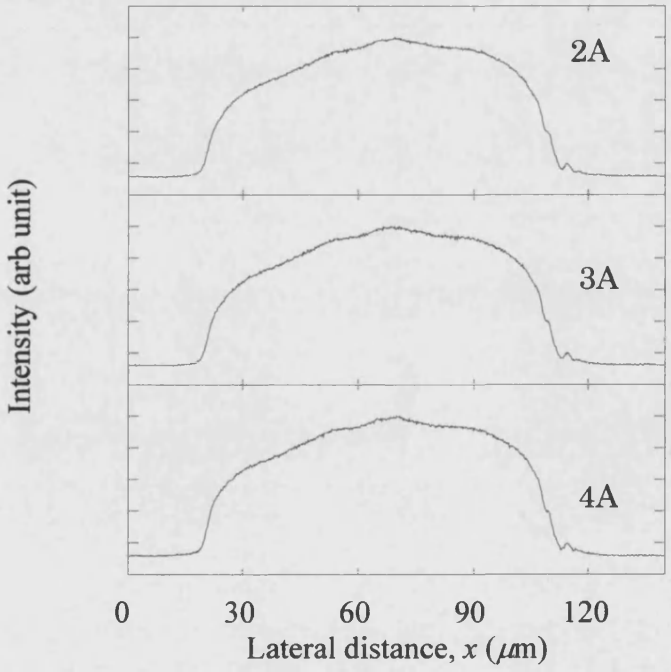

Figure 4.9: Measured near-field profiles UB763A at several currents after A-R coating.

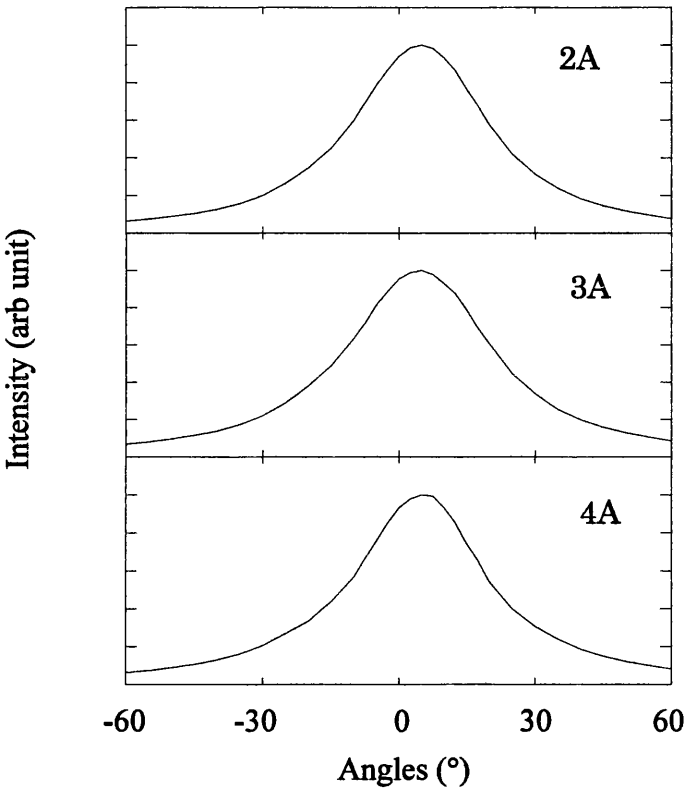

Figure 4.10: Measured far-field profiles of device UB763A at several currents after A-R coating.

- *Spectral Distribution*

Figure 4.11 shows the spectral variation of the light output from device UB763A at several currents. The spectral distribution had an approximately 9nm FWHM bandwidth over the current range 1A to 3A. Broadening of the spectra to 11nm was observed at 4A of current. This phenomenon was also observed by Boeck and Aman [6]. The width of the spectra distribution is related to the width of the gain curve. At high current densities the gain curve broadens with the increase in the quasi-Fermi separation, which in turn causes the broadening of the spectral distribution.

A shift in the peak of the emission wavelength from 883nm to 888nm was also noticed with increase in current. The movement of the spectral peak to long wavelengths has been shown theoretically by Goebel et. al, [7]. This has been attributed to heating effects in the active layer, [8]. Mounting the device p^+ side down, i.e. placing the active region closer to the heat sink should reduce the effect of heating. More importantly no discernible Fabry-Perot resonances were observed

even at high currents. This confirms that facet reflectivities are low and that feedback into the active region has been reduced significantly.

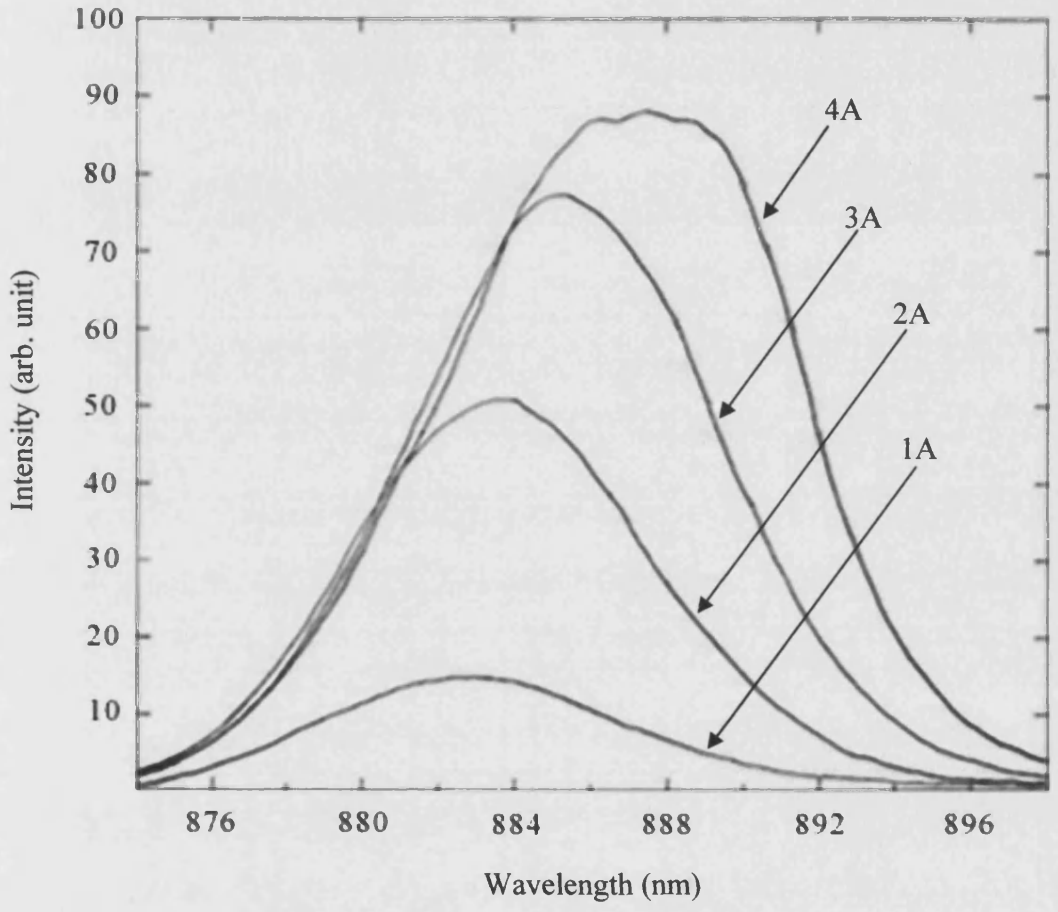

Figure 4.11: Emission spectrum at several currents from UB763A.

4.4 Variation in Taper Flare Angles - Experimental

The effect of varying the taper flare angles on the performance of the tapered SLDs, in particular on the angular intensity distribution, has been investigated. The experimental results of the measured light-current characteristic, near-field and far-field intensity distributions are contained and discussed in this section. Taper flare angles θ_T, are defined as;

$$\tan\theta_T = W_{max}/L_c$$

Devices with a variety of flare angles have been fabricated and measured. Table 4.2 contains descriptions of devices measured. All devices were fabricated from bulk material QT503A. The specification for this material can be found in Appendix 2A.

Device No	UB1041Y	UB1036Y	UB1058Y	UB1062Y
Wide facet, W_{max} (μm)	50	100	150	200
Narrow facet, W_{min} (μm)	5	5	5	5
Taper Contact Length, L_c (μm)	1000	1000	1000	1000
Contact Area (μm^2)	25,000	50,000	75,000	100,000
Deflector distance, L_1 (μm)	500	500	500	500
Flare Angles, θ_T	2.86°	5.71°	8.53°	11.31°

Table 4.2: Dimensions of TSLDs used for measurements in this section.

4.4.1 Light-Current Characteristics before and after A-R coating

Figure 4.12 shows the measured output power against current curves for devices UB1041Y, UB1036Y, UB1058Y and UB1062Y, before the wide facets were A-R coating. At low currents, the smaller area devices (UB1041Y and UB1036Y) have higher slope efficiencies than the larger area devices (UB1058Y and UB1062Y). However, at high currents the slope efficiencies for the smaller area devices has decreased. This is due to the high power densities in these devices. High power

densities cause the depletion of carriers and a reduction in gain, which in turn limits the output power. In contrast at high currents the larger area devices have better slope efficiencies. This is because the overall power densities in these devices are lower due to the larger active area. Over 130mW has been obtained from the device with the biggest flare angle (UB1062Y).

Figure 4.13 shows the various light output against current curves from the devices after the wide facets were A-R coating. From the curves plotted it can be seen that the slope efficiencies especially at high currents for all devices have improved. Once again over 1500mW of output power has been obtained from the device with the largest flare angle (UB1062Y)

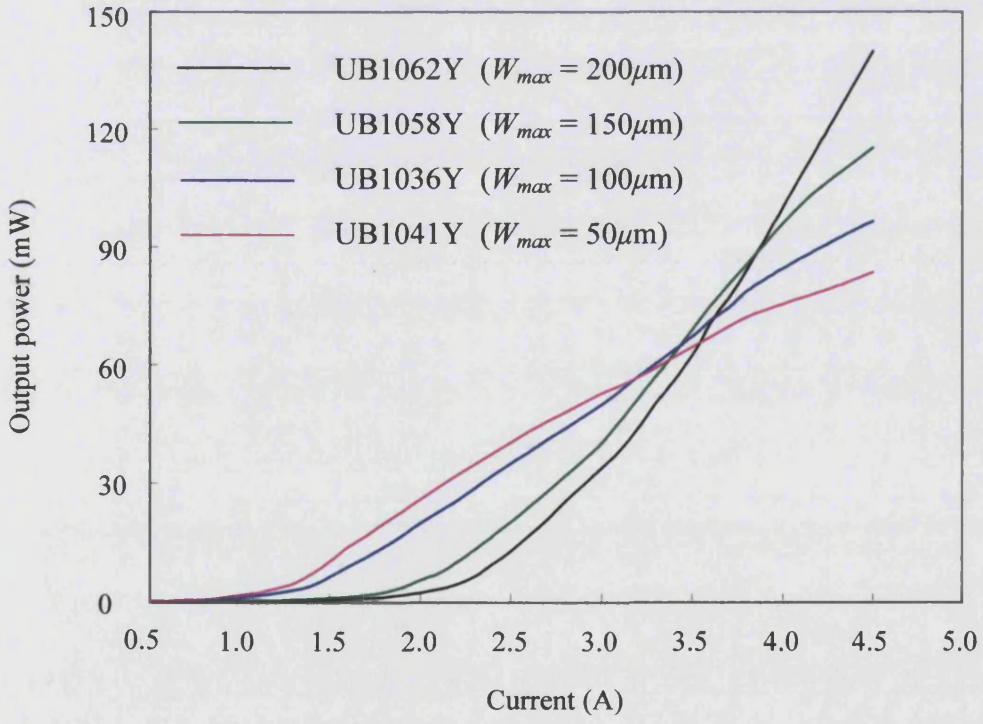

Figure 4.12: Measured light-current characteristics of devices UB1041Y, UB1036Y, UB1058Y and UB1062Y before the wide facets were A-R coated.

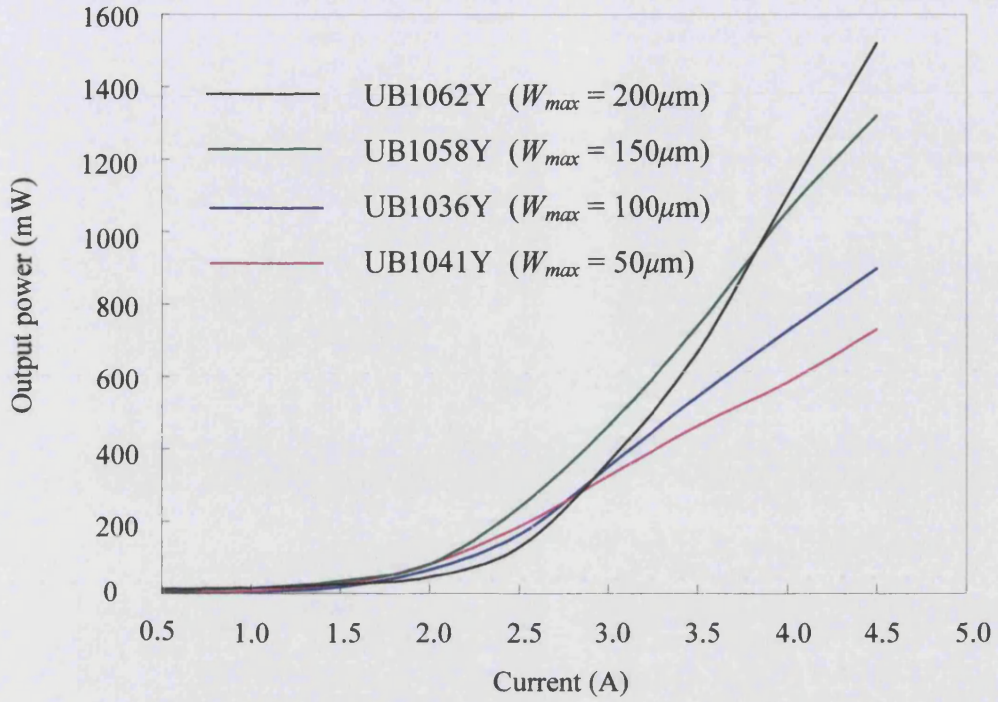

Figure 4.13: Measured light-current characteristics of devices UB1041Y, UB1036Y, UB1058Y and UB1062Y after the wide facets were A-R coated.

4.4.2 Measured Lateral and Angular Intensity Distribution after A-R Coating

- *Near-Field Intensity Distribution*

Figures 4.14, 4.15, 4.16, 4.17 shows the measured near-field intensity profiles from the output facets of devices UB1041Y, UB1036Y, UB1058Y and UB1062Y respectively after A-R coating at different currents. Most of the TSLDs showed some narrowing of the near-field profiles with increase in current. However, the near-field intensity profiles for device UB1062Y shown in Figure 4.17 consistently displayed asymmetric distribution at various currents. The asymmetry is presumed to be due to the uneven deposition of gold contact, which results in the uneven lateral distribution of current in the device.

- *Far-Field Intensity Distribution*

Figures 4.18 and 4.19, shows the measured far-field intensity profiles of the devices for two different currents. The far-field profiles shown in Figure 4.18 was measured

at 1A of input current, which is before the on-set of superluminescent operation (refer to Figure 4.13). For low bias current and correspondingly high loss, the output angular intensity distribution for devices with large θ_T, is almost Lambertian, meaning that it's angular dependence is a cosine function. The full width at half maximum (FWHM) for UB1062Y, which has the largest taper flare angle is ~ 80°. For devices with small θ_T the radiation pattern is narrower, even at low bias current, with a FWHM of ~56° for UB1041Y. At low bias current (low gain) the output radiation that escapes from the SLD, originates in a volume depth close to the output facet. In the case when the width of the output facet is wider than the effective depth from which the rays originate from, the SLD is considered a Lambertian radiator. Conversely when the output width is narrower than the effective depth of the originating rays, the SLD gives narrower angular intensity distribution. This is because rays escaping at larger angles originate from a depth on the order of the output width, thus carrying less power. Consequently, rays escaping at zero radiation angles, i.e. longer path length, have more power.

Figure 4.19 shows the far-field intensity distribution for the TSLDs measured at 3A of input current. For higher bias current the angular intensity distribution narrows with increase in gain. This can be explained by using similar arguments as in the low bias current case. The effective depth of the originating rays at high currents is now the entire length of the device. Rays originating form the rear end of the device carry the most power and are mostly directed at zero radiation angles. The far-field intensity FWHM of the TSLDs measured at 1A and 3A of current is compared and tabulated in Table 4.3.

			I=1A	I=3A
Device No	W_{max} (μm)	Flare Angle (θ_T)	FWHM	FWHM
UB1062Y	200	11.31°	80°	60°
UB1058Y	150	8.53°	70°	50°
UB1036Y	100	5.71°	62°	40°
UB1041Y	50	2.86°	56°	30°

Table 4.3: The FWHM of devices UB1062Y, UB1058Y, UB1036Y and UB1041Y is compared at low and high currents.

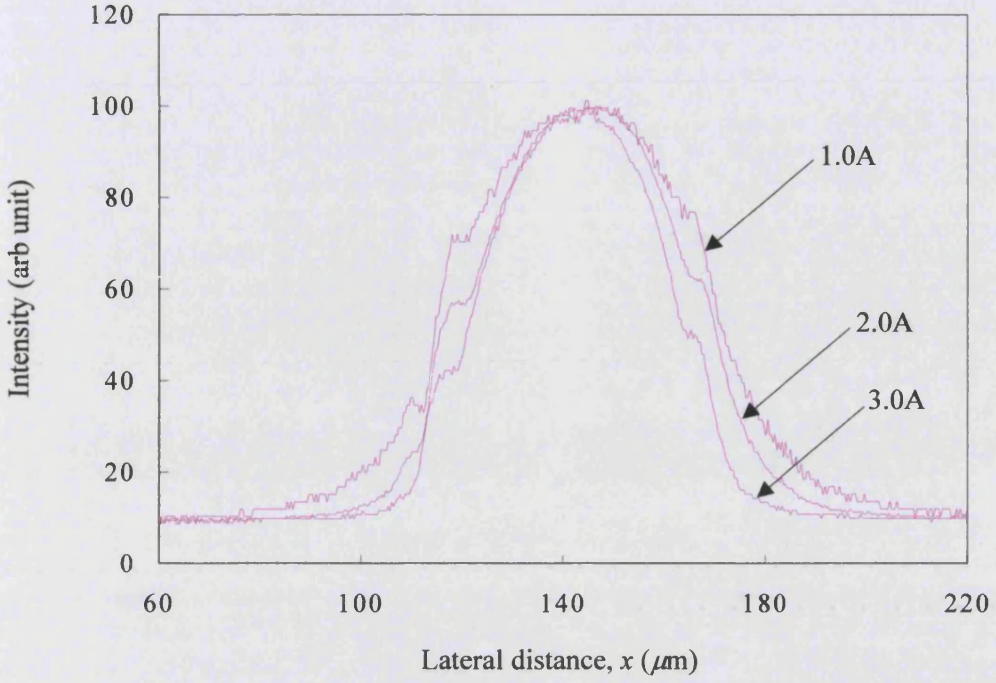

Figure 4.14: Measured near-field profiles of UB1041Y (50μm TSLD) at several currents.

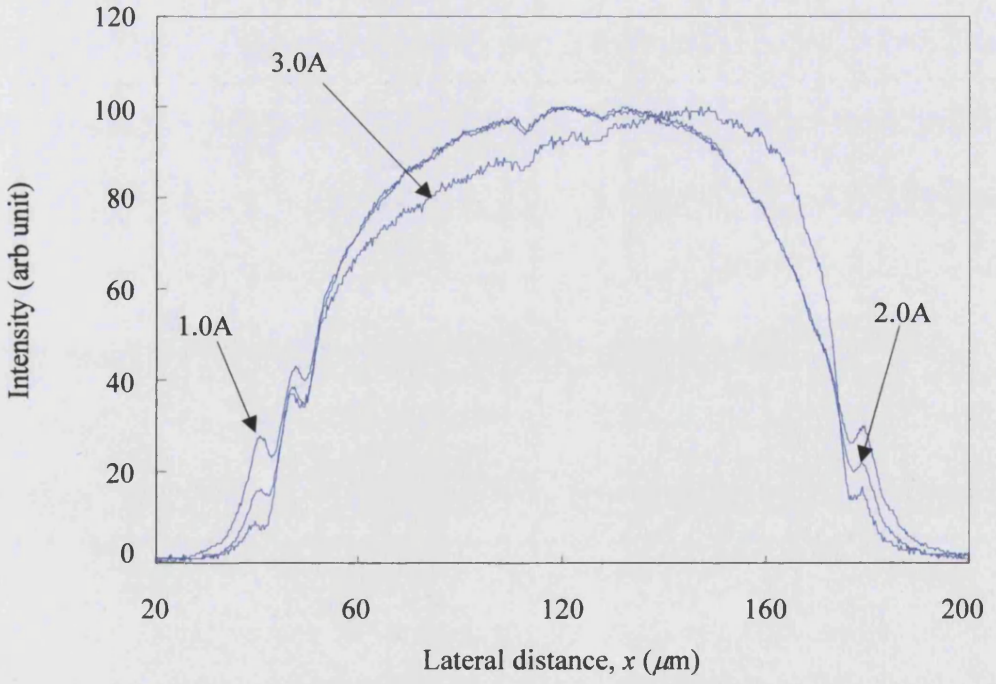

Figure 4.15: Measured near -field profiles of UB1036Y (100μm TSLD) at several currents.

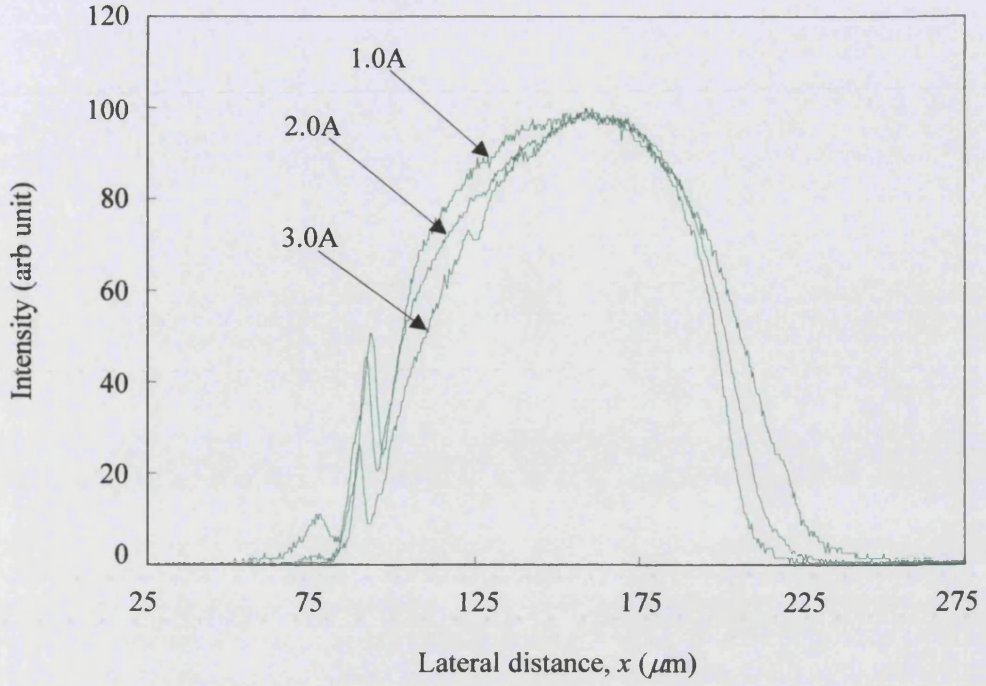

Figure 4.16: Measured near -field profiles of UB1058Y (150μm TSLD) at several currents.

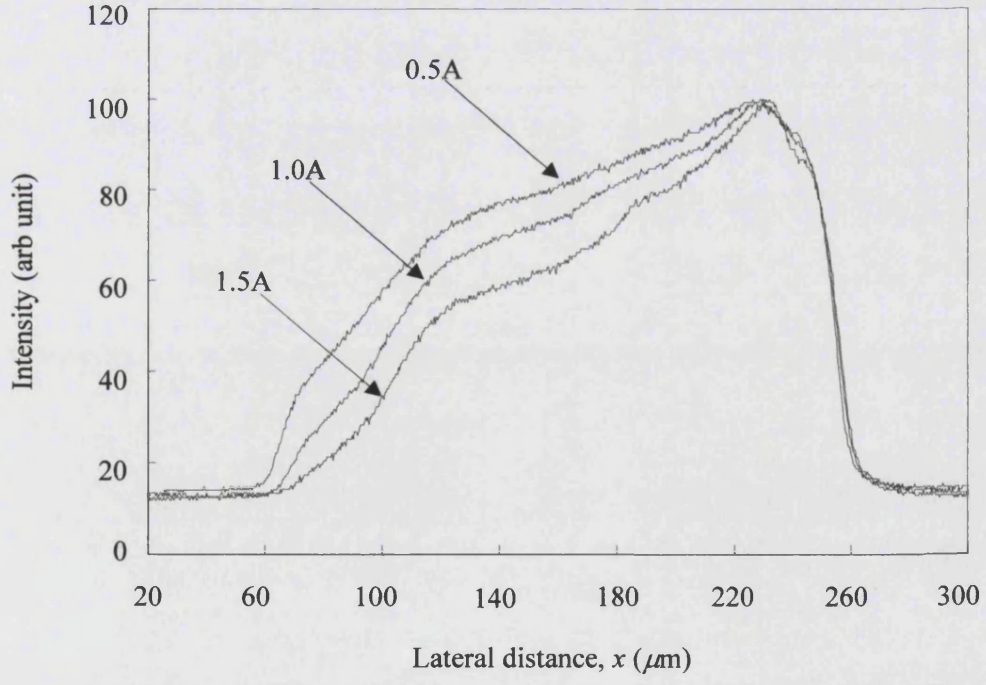

Figure 4.17: Measured near -field profiles of UB1062Y (200μm TSLD) at several currents

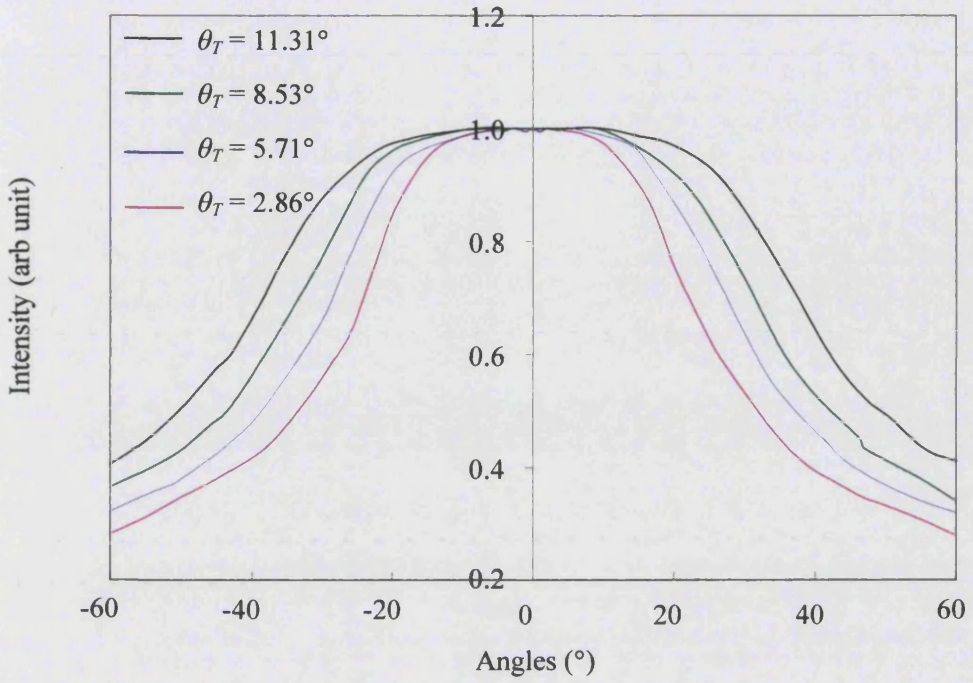

Figure 4.18: Measured far-field profiles of devices UB1062Y, UB1058Y, UB1036Y and UB1041Y at 1A of current.

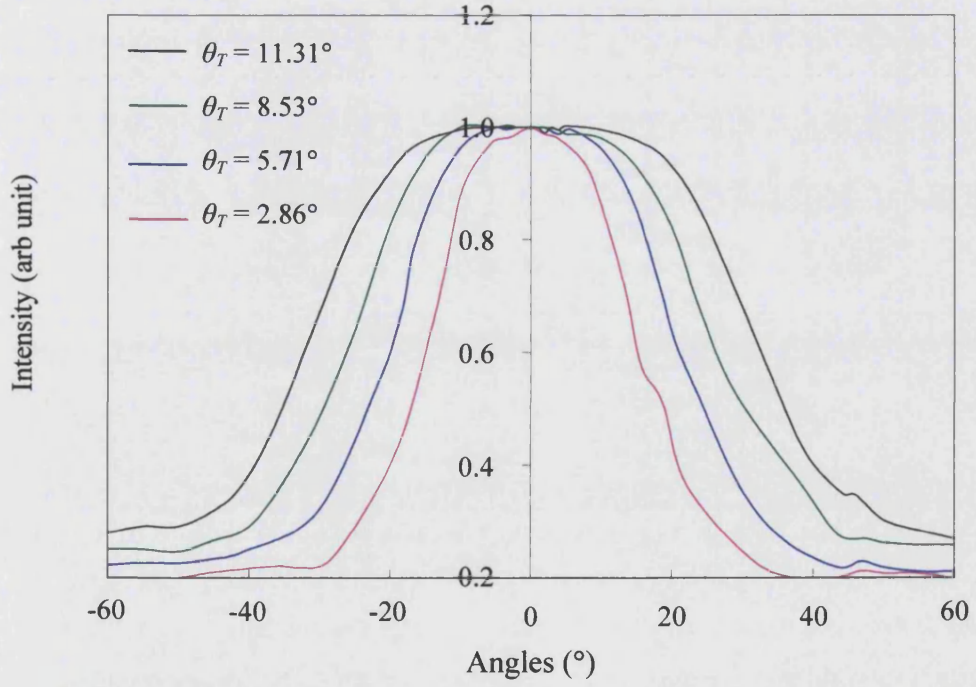

Figure 4.19: Measured far-field profiles of devices UB1062Y, UB1058Y, UB1036Y and UB1041Y at 3A of current.

4.5 Shape Comparison – Parallel Stripe and Taper SLDs

A comparison between parallel stripe and taper SLDs of equal area has been made and is presented in this section. The measured L-I slope efficiency increases made possible by a single layer of A-R coatings to parallel and tapered SLDs are also presented. A total of six devices, three parallel stripe SLDs (PSLDs) and three tapered SLDs (TSLDs), were measured. All devices were 1000μm long and were fabricated from material QT543R. Specification of the material can be found in Appendix 2A. Table 4.4 contains descriptions of the devices measured.

	Tapered SLD (TSLD)	Parallel SLD (PSLD)
Device No.	1036Y, 1037Y,	1036B, 1037B, 1038B
Wide facet, W_{max} (μm)	100	50
Narrow facet, W_{min} (μm)	5	50
Contact Length, L_c (μm)	1000	1000
Deflector	Yes	Yes
Defl. Distance, L_1 (μm) (μm)	500	500

Table 4.4: Dimensions of taper SLDs and parallel stripe SLDs.

4.5.1 Light-Current Characteristics before A-R Coating - Experimental

Figure 4.20 shows the light output against current curves for all the six devices. It is clear from the graph that at high currents the TSLDs yields more power than the PSLDs. However this is not the case at all currents. To understand how these devices operate the plots are divided into two well defined regions:

1) Region A (0A – 1.2A) – a linear region (low currents).
2) Region B and C (1.2A – 4.0A) – an exponential region (moderate to high currents).

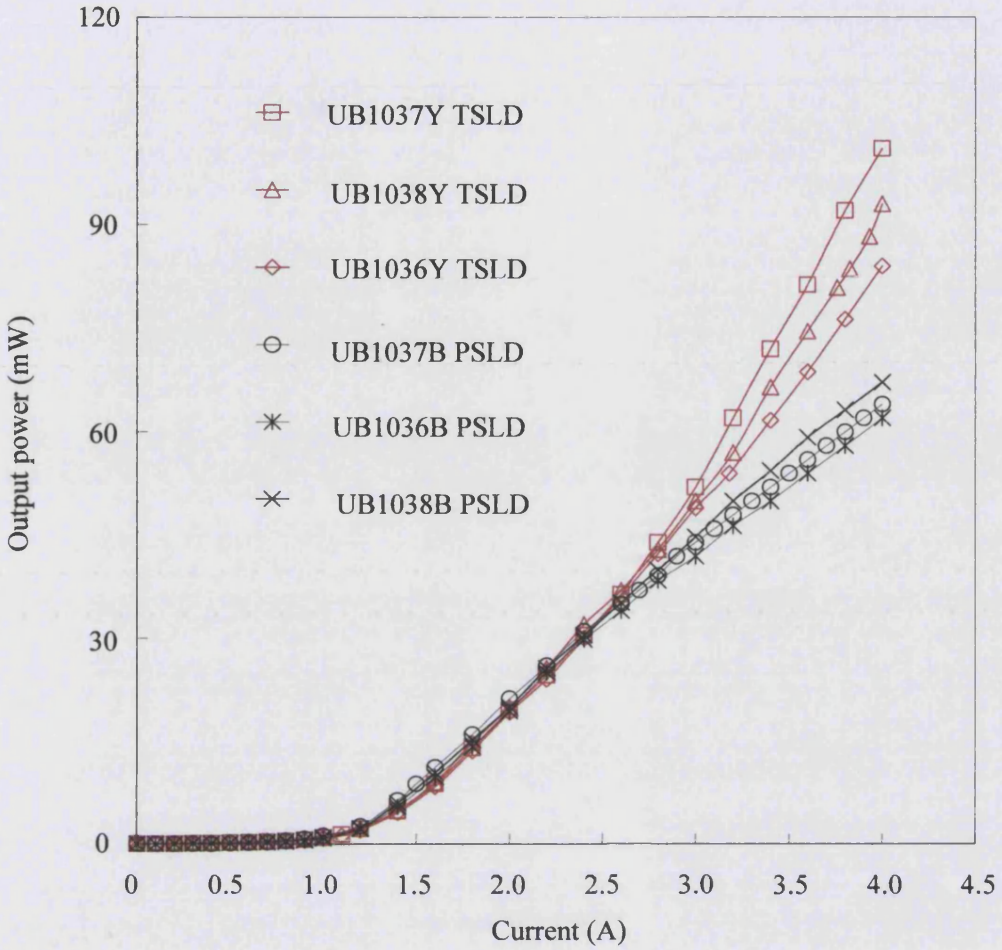

Figure 4.20: Measured light-current characteristics of TSLDs and PSLDs.

- ***Region A - (0A – 1.2A)***

Figure 4.21a, b and c shows the measured output power against current curves for devices UB1036(Y,B), UB1037(Y,B) and UB1038(Y,B). From the curves plotted it can be seen that at low currents, all the TSLDs yield more output power than the PSLDs. This is not what one might expect considering that the total active area for these two types of devices are equal. This can be easily explained by first considering that at low currents the medium is very lossy (absorbing). In this situation the radiation that escapes from the SLD, which contributes to the output power, originates from a volume close to the output facet (discussed earlier in section 4.2.2). In this case the width of the output facet for the TSLD is twice that of the PSLD, hence bigger volume. Therefore the TSLD emits more power than the PSLD.

Another interesting result that can be seen from the graphs plotted is that at about 0.8mA of current the two types of devices (parallel and taper) emit identical amount of power. At this value of current (0.8A), the current density J_0 = 1600A/cm^2. Substituting this value into equation (3.4) from Chapter 3 gives the carrier density, N = 1.42 x 10^{18} cm^{-3}. This is close to the typical N transparency value for GaAs based material, which is $N \approx$ 1.5 x 10^{18} cm^{-3} [9]. At transparency, the medium is neither absorbing nor does it have gain. In this situation rays of light generated at the back of the device are able to propagate through to the output facet without suffering any attenuation. As a result much of the light generated in the active area of the device (defined by the top metal contact) is able to radiate out and contribute to the output power. Given that the two types of devices (taper and parallel) have equal active area the output power these devices emit at transparency are also equal.

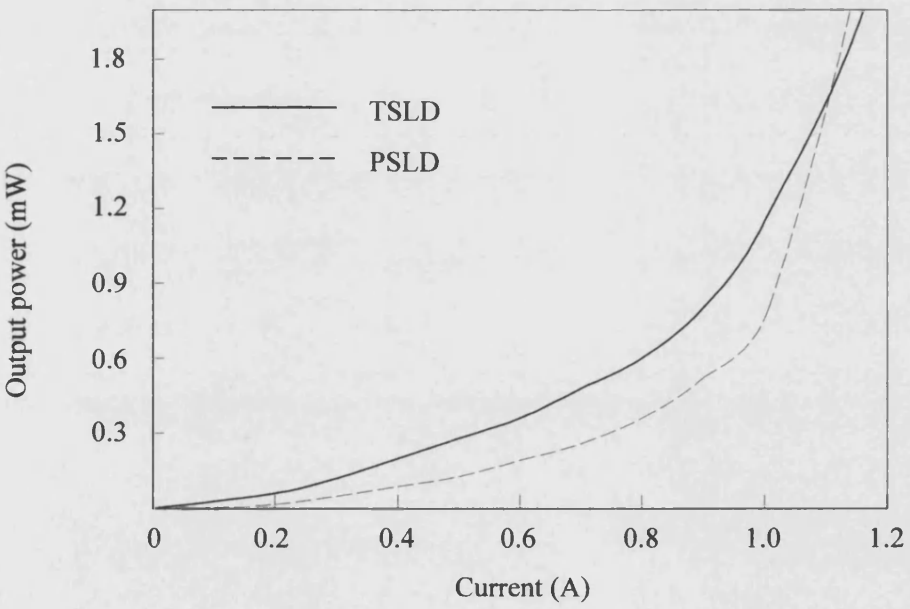

Figure 4.21a: Measured light-current characteristics of devices UB1037(Y, B).

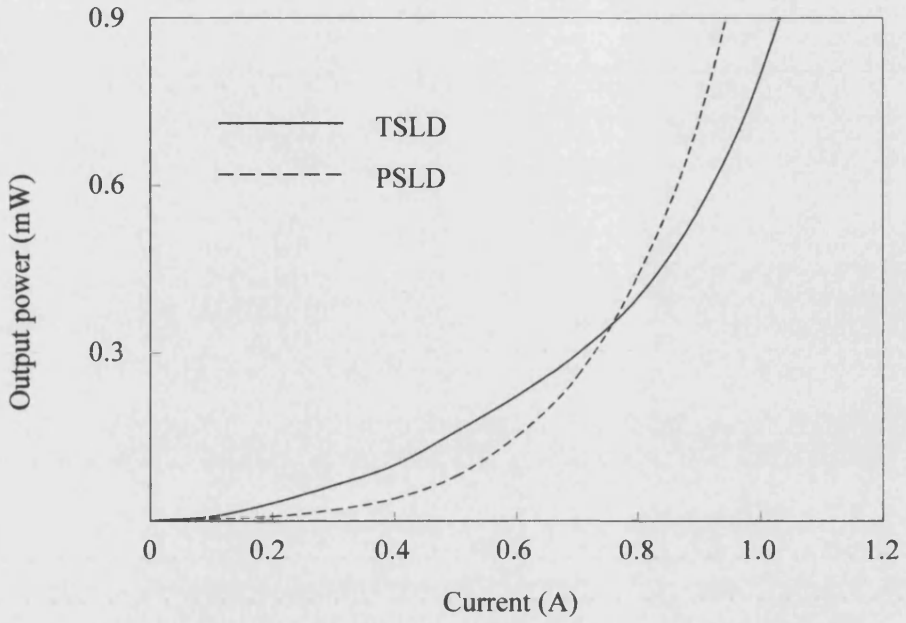

Figure 4.21b: Measured light-current characteristics of devices UB1036(Y, B).

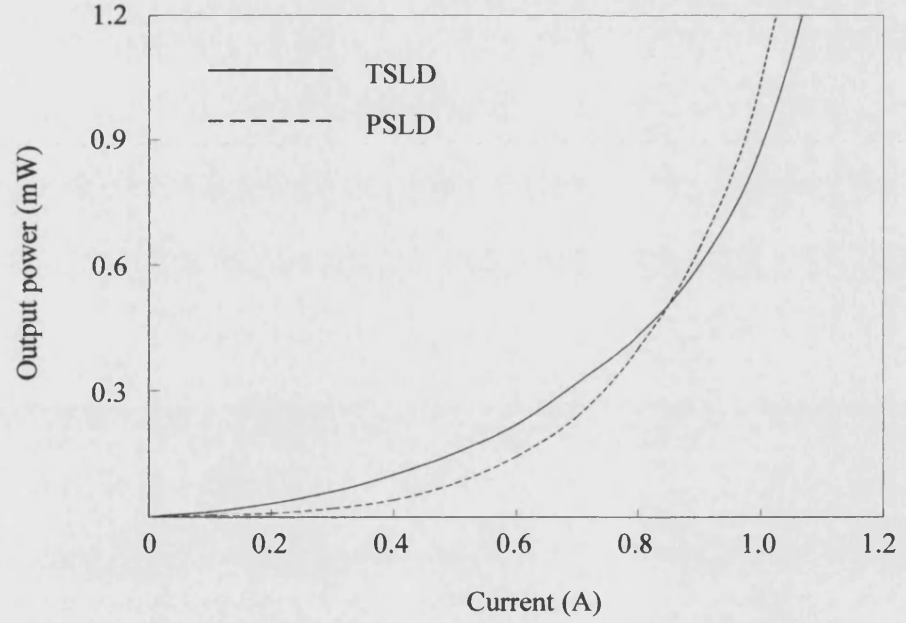

Figure 4.21c: Measured light-current characteristic of devices UB1038(Y, B).

- ***Region B and C - (1.2A – 4.0A)***

Figure 4.23a, b and c show comparison of the light current characteristic for the taper and parallel stripe SLDs between 1.2A – 4.0A. From the current range of 1.2A – 2.0A, the parallel stripe SLDs yields more power than the tapered SLDs. To explain this behaviour, consider that the active medium is no longer lossy but has gain with rays originating from the rear end of the device contributing significantly to the output power. For such rays, in fact, the exponential amplification it achieves is highest due to its long path length. With reference to Figure 4.22, the total area of the parallel stripe SLD, from $z = 0$ to $z = L_c/2$, is twice that of the TSLD. Hence, the parallel stripe SLD is able to generate more rays with long path lengths in comparison to the TSLD. This results in the PSLDs yielding more power than the TSLDs.

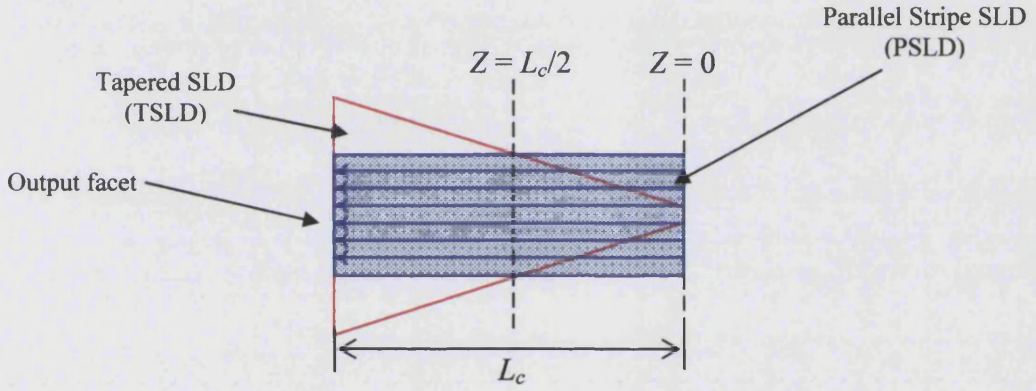

Figure 4.22: Schematic diagram comparing the total area of a PSLD and a TSLD. The diagram also illustrates parallel rays with high gain originating from the back of the PSLD.

Interestingly, a change in trend occurs at about 2.0A of current, whereby the tapered devices emit more power than the parallel stripe devices. Also evident from the curves plotted is that the slope efficiencies at high currents for the PSLDs have decreased. It is worth mentioning here that the front facet of these devices were not A-R coated. The decrease in slope efficiencies seen in the parallel stripe devices is due to carrier depletion (hole-burning), which limits the available output power from the device. In contrast the tapered geometry devices showed less susceptibility to the effects mentioned above and therefore delivered more power especially at high currents. These results indicate that tapered geometry devices in general are less sensitive to optical feedback from the front facet.

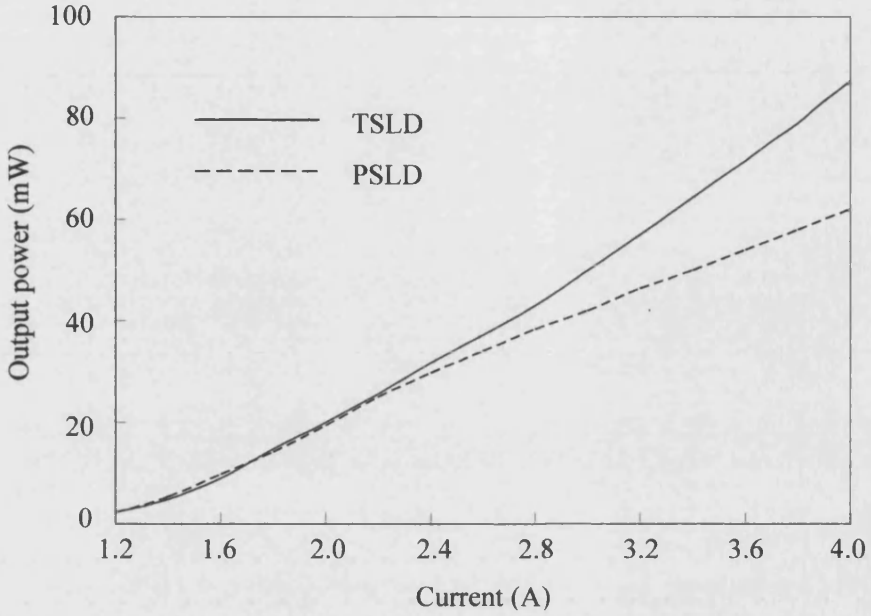

Figure 4.23a: Measured light-current characteristics of devices UB1037(Y,B). Solid curve – tapered SLD UB1037Y. Dashed curve – parallel stripe SLD UB1037B.

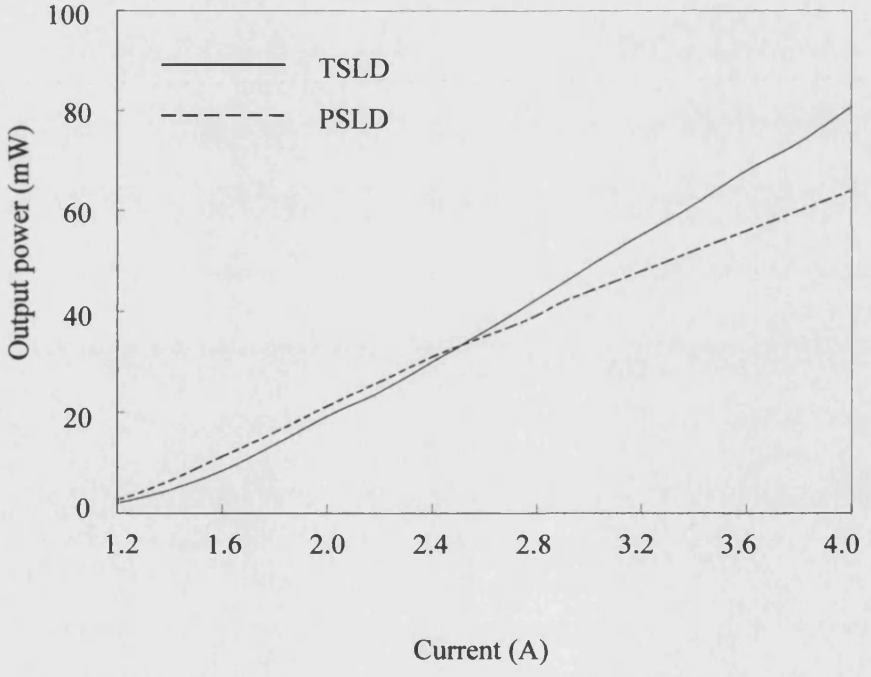

Figure 4.23b: Measured light-current characteristics of devices UB1036(Y,B). Solid curve – tapered SLD UB1036Y. Dashed curve – parallel stripe SLD UB1036B.

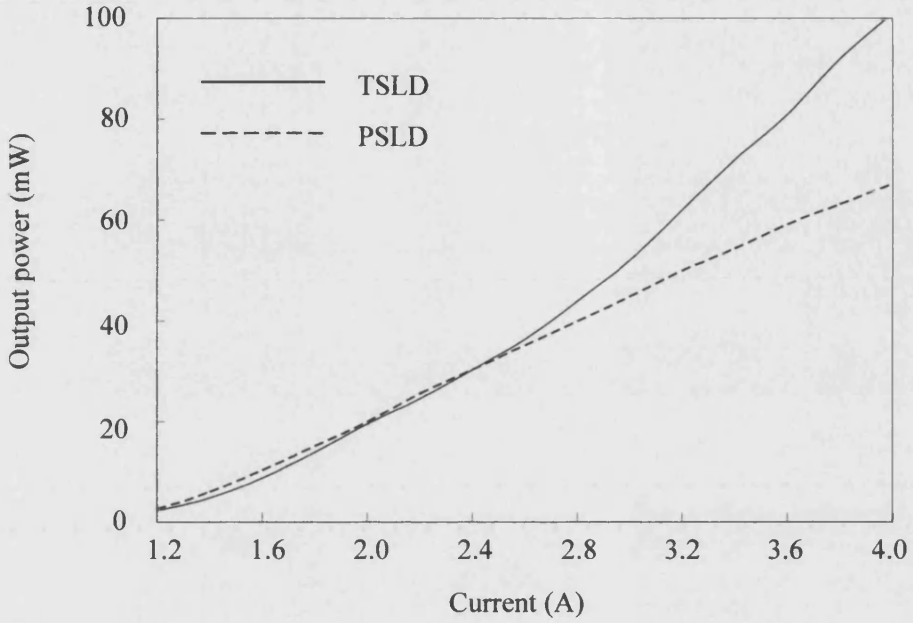

Figure 4.23c: Measured light-current characteristics of devices UB1038(Y,B). Solid curve – tapered SLD UB1038Y. Dashed curve – parallel stripe SLD UB1038B.

4.5.2 Light-Current Characteristics after A-R Coating - Experimental

Figure 4.24 shows the measured output power against current curves for devices UB1037Y which is a 100μm wide TSLD and UB1037B which is a 50μm wide PSLD, after the output facets was A-R coated. Comparing Figure 4.24 with Figure 4.23a, it is clear that the slope efficiencies, especially at high currents, for both devices have increased. Interestingly, either before or after A-R coating the tapered geometry SLD still showed superior performance compared to the parallel stripe SLD.

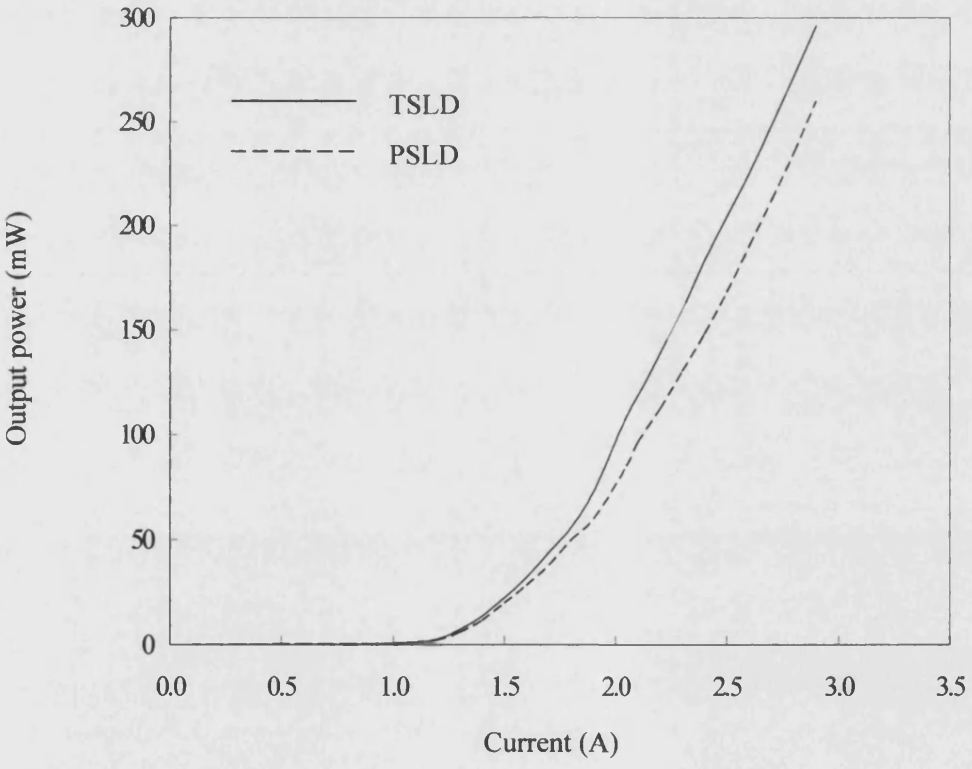

Figure 4.24: Measured light-current characteristics of TSLD UB1037Y and PSLD UB1037B.

4.5.3 Near-Field and Far-Field Intensity Distribution after A-R Coating

The measured near-field intensity distribution from devices UB1037Y and UB1037B is shown in Figure 4.25 and 4.26 respectively. It can be seen from Figure 4.25 that the near-field intensity profiles of the tapered SLD showed little change in profiles at low currents but narrows slightly at high current. However, the parallel stripe SLD showed slight changes in the near-field profiles with increase in current. A slight dip in the middle of the profile is observed. This indicate that even with A-R coating the power density across the output facet of the parallel stripe SLD is high, which suggests that the device is more prone to catastrophic optical damage (COD) than the tapered SLD.

The far-field intensity distribution for these devices was also measured and is shown in Figure 4.27 and 4.28. From these figures it can be seen that the far-field profiles narrows with increase in current. On close inspection, at high currents, the far-field profile from the tapered SLD (UB1037Y) is slightly narrower the parallel stripe SLD (UB1037B). This is an unexpected result, as initially it was thought that the far-field profile of the TSLD would be broader than the PSLD, since it has a much broader output facet.

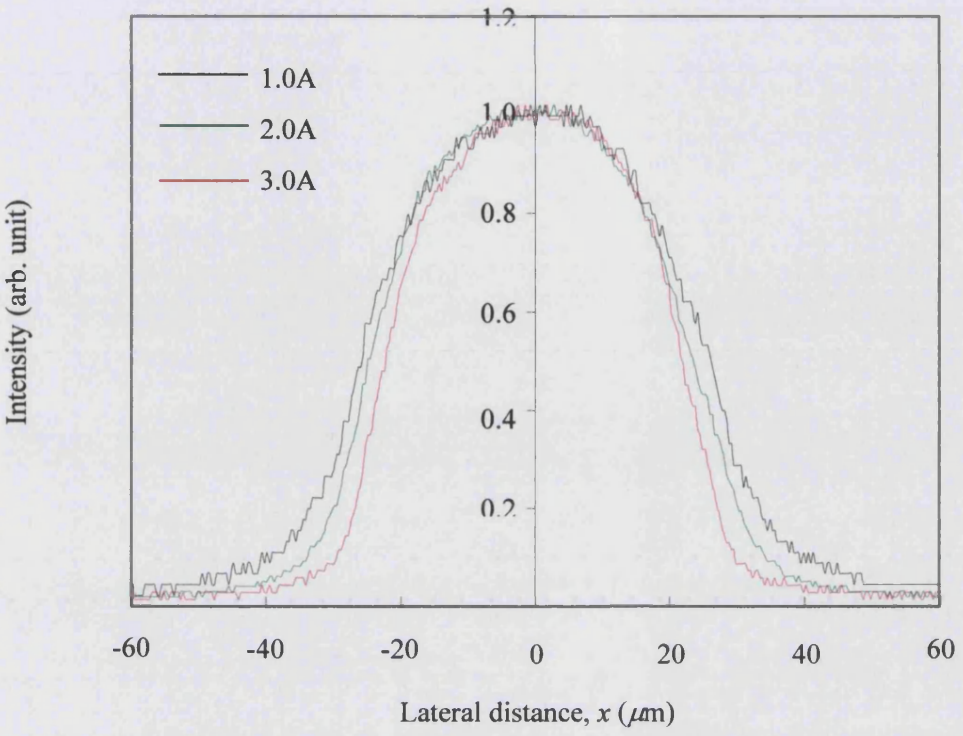

Figure 4.25: Measured near-field profiles of tapered SLD UB1037Y at several currents.

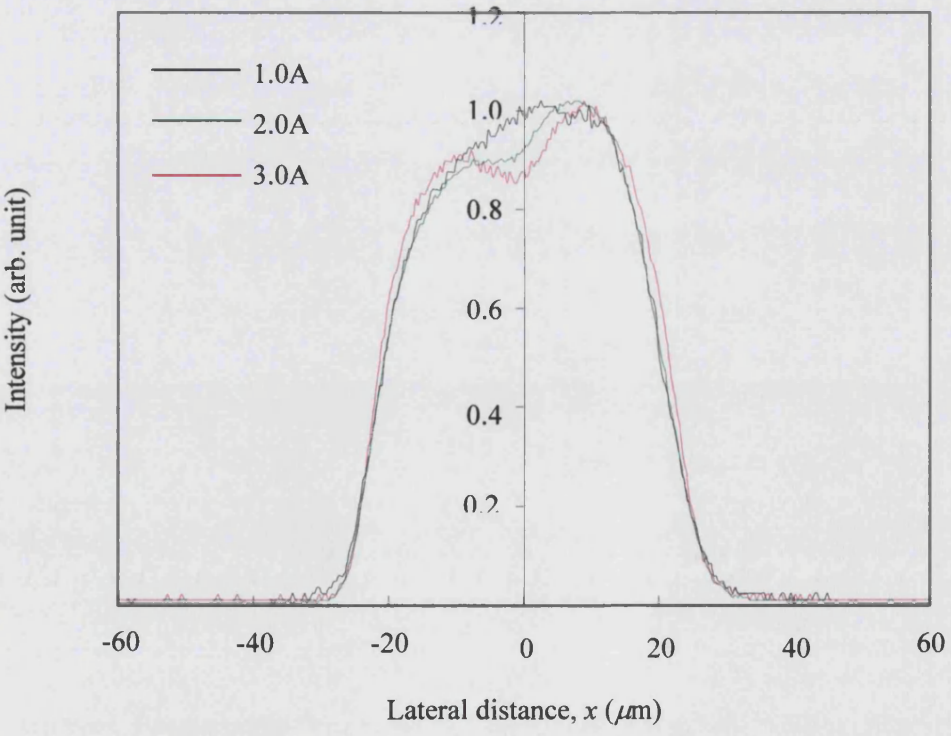

Figure 4.26: Measured near-field profiles of parallel stripe SLD UB1037B at several currents.

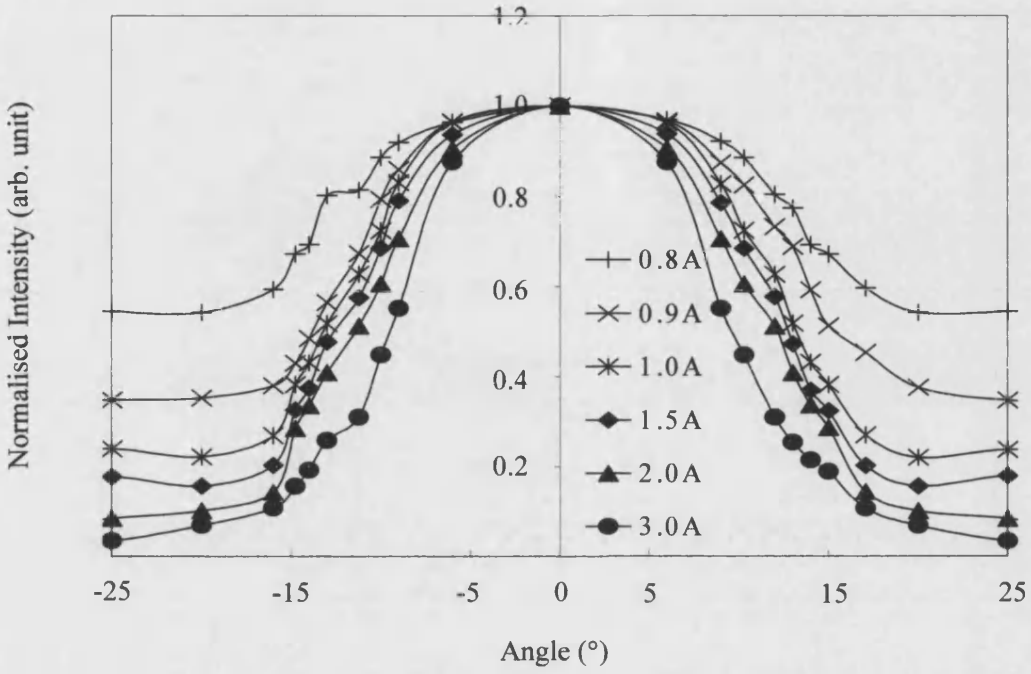

Figure 4.27: Measured far-field profiles of tapered SLD UB1037Y at several currents.

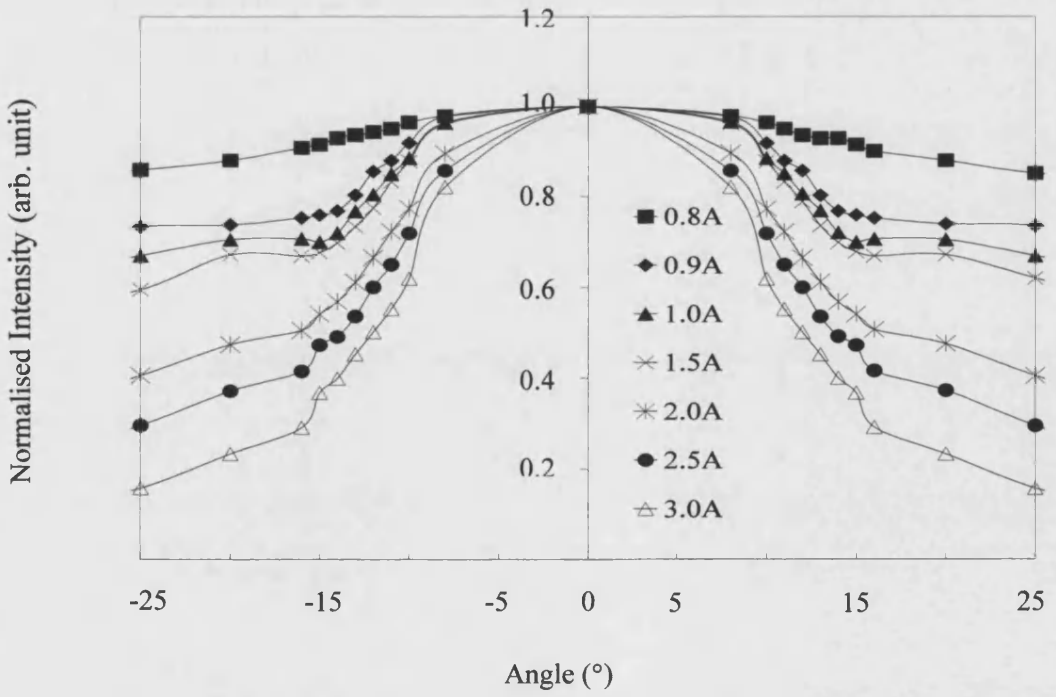

Figure 4.28: Measured far-field profiles of parallel stripe SLD UB1037B at several currents.

4.6 Conclusions

Experimental results presented in section 4.3 have shown that the combination of tapered geometry contact, A-R coating on the front facet and the etched deflector in the absorbing region has not only reduced facet reflectivities but significantly improved the L-I slope efficiencies of the TSLD. Output powers over 500mW quasi CW was obtained from a 100μm wide and 1000μm long TSLD. The spectral distribution showed no discernible Fabry-Perot resonances up to 4A of input current. The beam quality from this device was also good. The near-field field and far-field profiles were broad and stable at various currents.

In section 4.4 it was shown that TSLDs with large flare angles emit high powers but may not be suitable for fibre coupling applications. The far-field profiles FWHM from these devices are broad and thus power may not couple well into the optical fibre. However the TSLD flare angle can be designed to give narrower far-field profiles in order to achieve better coupling to optical fibres. For TSLDs with small flare angles the length of the device can be made longer to increase the output power it yields.

An experimental comparison of the output characteristics between PSLDs and TSLDs has been made. Results from the light-current characteristic have revealed that at high currents, tapered geometry SLDs gives superior performance compared to parallel stripe SLDs of similar area. This indicates that TSLDs have a reduced susceptibility to power saturation. However, unexpectedly, the measured far-field profile from the TSLD has been found to be slightly narrower than the PSLD. The reasons for this are as yet unclear.

In conclusion, tapered geometry SLDs has great potential for high power applications. Also, the simple fabrication process and non-stringent tolerance of the A-R coating make this device a cheap source of high-power wide-bandwidth amplified spontaneous emission (ASE).

References

[1] *F. Koyama, K. Y. Liou, A. G. Dentai, T. Tanbun-ek, C. A. Burrus*, **'Multi-8-Quantum-Well GaInAs/GaInAsP Tapered Broad-Area Amplifiers with Monolithically Integrated Waveguide Lens for High-Power Applications'**, IEEE Photonics Letters, Vol. 5, No. 8, pp. 916-919, 1993.

[2] *L. Goldberg, D. Mehuys, D. C. Hall*, **'3.3 CW Diffraction Limited Broad Area Semiconductor Amplifier'**, Electronics Letters, Vol. 28, No. 12, pp. 1082-1084, 1992.

[3] *I.Middlemast, J. Sarma, S. Yunus*, **'High Power Tapered Superluminescent Diodes using Novel Etched Deflectors'**, Electronic Letters, Vol.33, No.10, pp. 903-904, 1997.

[4] *L. Goldberg, D. Mehuys*, **'High-Power Superluminescent Diode Source'**, Electronic Letters, Vol. 30, No. 20, pp. 1682-1684, 1994.

[5] *J. C. Livas, S. R. Chinn, E. S. Kintzer, J. N. Walpole, C. A. Wang, L. J. Missaggia*, **'Singlemode Optical Fibre Coupling of High-Power Tapered Gain Region Devices'**, IEEE Photonic Technology Letters, Vol. 6, No. 3, pp. 422-424, 1994.

[6] *Aman, Boeck and Harth*, **'The Influence of Technological Parameters on Spectral Properties of Double Heterostructure Superluminescent Diodes'**, Frequenz, Vol. 45, p. 635, 1978.

[7] *E. O. Goebel, O. Hildebrand and K. Lohnert*, **'Wavelength Dependence of Gain Saturation in GaAs Lasers'**, IEEE J. of Quantum Electronic, Vol. QE-13, p.848, 1977.

[8] *Kressell and Butler*, **'Semiconductor Lasers and Heterojunction LEDs, Academis Press'**, Chapter 14.

[9] *H. Kressel and J. K. Butler*, **'Semiconductor Lasers and Heterojunction LEDs'**, Academic Press, p. 556, 1977.

Chapter 5

Angled Tapered Superluminescent Diodes

5.1 Introduction

Experimental results presented in Chapter 3 and Chapter 4 have shown that a combination of etched deflector and a single layer of anti-reflection (A-R) coating on the front facet caused a dramatic increase in the output power of the TSLD. It is essential to reduce reflected light from the front facet from coupling into the narrow end of the taper. This is because carrier depletion, [1], [2], in the narrow end of the taper significantly reduces gain and consequently the available output power from the TSLD. It is expected that further reduction of the output facet reflectivity, e.g. multilayer A-R coating, will further increase the output power from the TSLD. However, the deposition of high quality A-R coatings requires complicated and often expensive fabrication technique. As a consequence, alternative ways of reducing front facet reflectivity has been investigated.

One of the simplest methods for reducing the effective reflectivity of the front facet is to incline the taper contact at an angle with respect to the normal of the output facet. This method has been used by Alphonse et al. [3] and Takayama et al. [4] on narrow parallel stripe LEDs, and has been proven to be very effective. Hence, this approach has been adopted for the TSLDs.

This chapter presents the experimental characterisation of high power angled tapered superluminescent diodes (ATSLDs), and demonstrates the effectiveness of angular displacement of the contact in reducing front facet reflectivity and hence improve device performance. This chapter also describes the asymmetry of the near-field intensity distribution obtained from ATSLDs and how they can be explained by a

simple ray analysis. A discussion on the ray analysis method used to model the ATSLD is given in section 5.3 of this chapter. In order to test the validity of the ray model different experimental measurements were employed, one is the measurement of the near-field profiles at low and high currents and the second is the spectrally resolved near-field intensity profile of ATSLDs. Discussions and results from the measurements are presented in section 5.4.

5.2 Experimental Results

A number of ATSLDs with different inclination angle were fabricated from semiconductor bulk material QT543R. The specification of this material can be found in Appendix 2A. Figure 5.1 shows a schematic diagram of the ATSLDs. A number of devices have also been fabricated without the etched back deflector. The devices all had W_{max} = 100μm and were 1000μm long. Devices were mounted p+ side down on copper heatsinks, to avoid heating effects seen in the previous batch of TSLDs presented in chapter 4. Table 5.1 contains descriptions of the devices measured. The measurement techniques used for the following measurements are detailed in Appendix 3B.

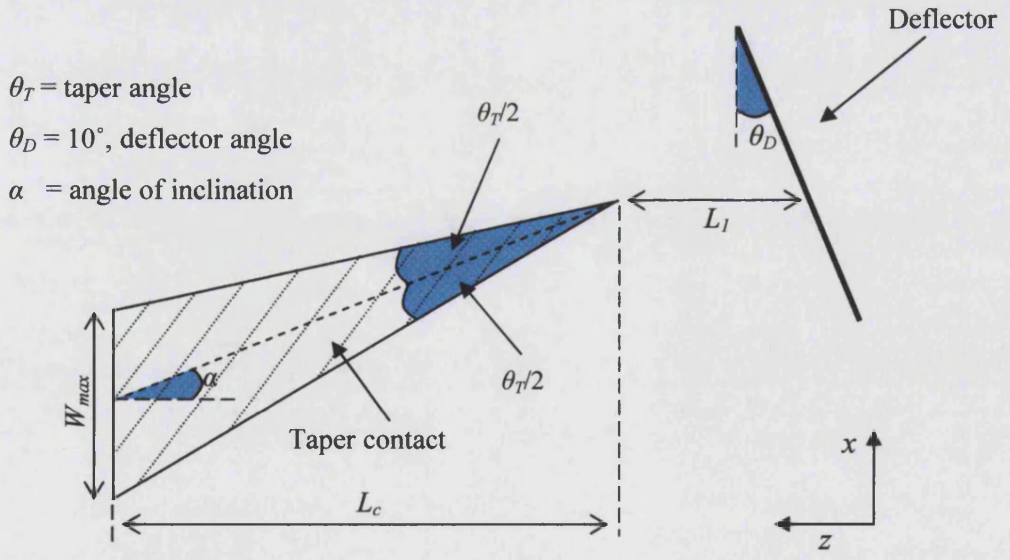

Figure 5.1: Schematic diagram of an ATSLD with an etched back deflector.

Device No	UB763A	UB764A	UB764B	UB765A	UB765B	UB1021
Inclination angle α	0°	5°	5°	10°	10°	5°
Wide facet, W_{max} (μm)	100	100	100	100	100	100
Taper length, L_c (μm)	1000	1000	1000	1000	1000	1000
Deflector	Yes	Yes	No	Yes	No	Yes
Def. Dis., L_1 (μm)	500	500	-----	500	-----	500

Table 5.1: Dimensions of ATSLDs used in the experiments.

5.2.1 Light-Current Characteristic

A number of ATSLDs with angular displacements α = 5° and 10°, with and without the etched back deflector were measured. Figure 5.2 shows a plot of output power against current curves for devices UB764(A,B) and UB765(A,B). The curves show that the device with an angular displacement α = 5° (UB764B) without the etched back deflector reached lasing threshold at about 2A of current. In contrast a similar device (UB764A) with an etched deflector showed no lasing characteristics up to 4A of current. This indicates that a slight misalignment of the electrical contact does not sufficiently reduce reflected light from the front facet to inhibit lasing. Therefore, in this case, an etched deflector is necessary to destroy the optical feedback path and suppress lasing. Conversely, the device with an angular displacement α = 10° (UB765B) without the etched back deflector did not reach lasing threshold, which indicates that there is sufficient suppression of reflected light into the active region. Note also that a similar device (UB765A) with an etched back deflector emitted more power, over 500mW.

Figure 5.3 shows a comparison between the measured L-I characteristics of ATSLDs UB764A (α = 5°) and UB765A (α = 10°) with a head on taper UB763A (0°), before and after the front facet of UB763A was A-R coated. It can be seen from the curves that only a moderate improvement in emitted power is obtained from the device with α = 5° in comparison to the head on taper (UB763A) before A-R coating. However higher output powers was obtained from the device with α = 10° (UB765A),

indicating that an angular displacement of 10° is sufficient to produce a stronger reduction in facet reflectivity than that obtained from a single layer of A-R coating, which resulted in front facet reflectivity of ~ 2%.

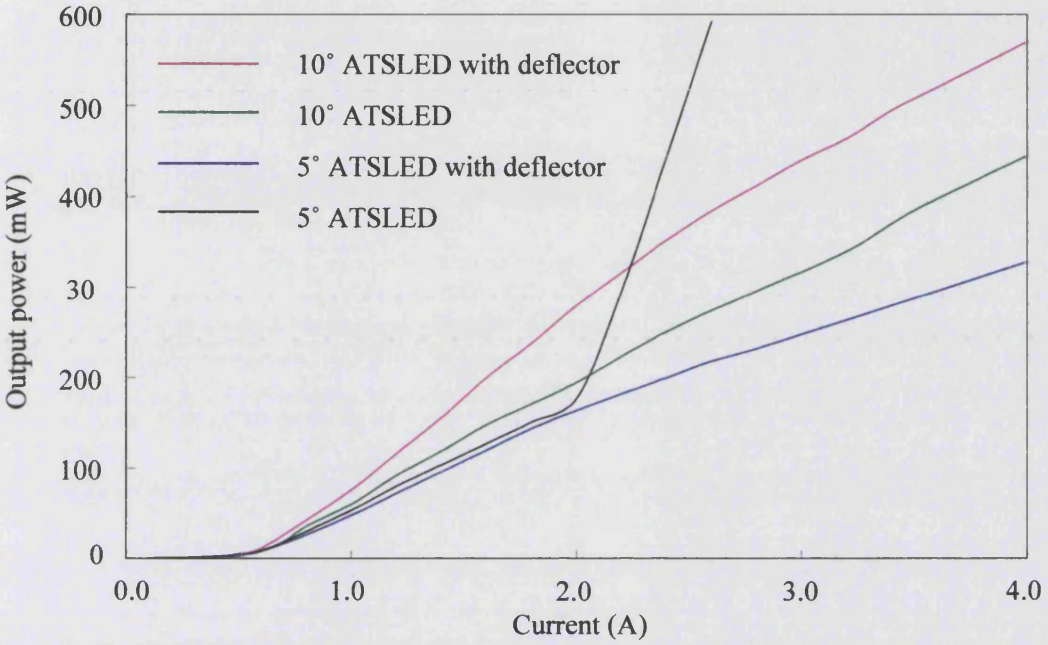

Figure 5.2: Measured L-I characteristics of ATSLDs UB764(A,B) and UB765(A,B).

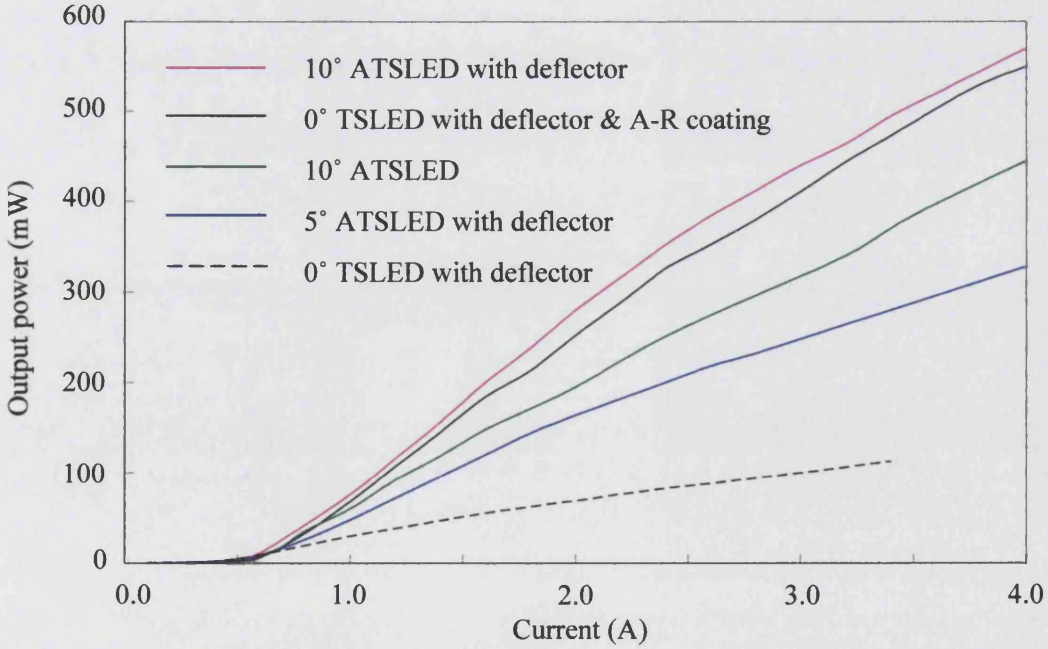

Figure 5.3: L-I characteristics of ATSLDs UB764A, UB765A and TSLD UB763A before and after A-R coating.

5.2.2 *Measured Degree of Polarisation*

The light emitted by SLDs is partially polarised and is usually described by a commonly used term, the degree of polarisation (DOP). This is defined as

$$\mathrm{DOP} = \frac{(P_{TE} - P_{TM})}{(P_{TE} + P_{TM})} \times 100\% \tag{5.1}$$

where P_{TE} and P_{TM} are the power in the TE and TM polarisations respectively. The factor of 100 simply converts the fraction into a percentage. Equation (5.1) implies that the DOP is positive when the power is mainly TE polarised, negative when the power is mainly TM polarised and zero when both polarisations contribute to the output power. To obtain the degree of polarisation of SLDs the light-current characteristics of both TE and TM polarisations were measured. The measurement technique is detailed in Appendix 3B.

The polarisation characteristics of laser diodes are different from SLDs, with the output power being mainly TE polarised due to the reflectivity of the cavity facets, [5]. The output powers from SLDs are not dependent on facet reflectivities and therefore should show a slight preference for the TM polarisation. To verify this several ATSLDs and a TSLD (head on taper) polarisation characteristics were measured. Figure 5.4 shows a plot of DOP against current for devices UB764A (α = 5°), UB765A (α = 10°) and UB763A (α = 0°). All the devices show a distinct preference for TE polarisation, which increases with injected current. It has been suggested in [6], [7] that the preference of TE polarisation is partly due to the fact that the confinement factor for the TE polarised light is slightly greater than it is for the TM polarised light. Hence, the gain experienced by the TE polarised light is greater than that of the TM polarised light. Another contributing factor is that the fraction of spontaneous emission coupling to the TE and TM polarisation may not be equal [8], [9].

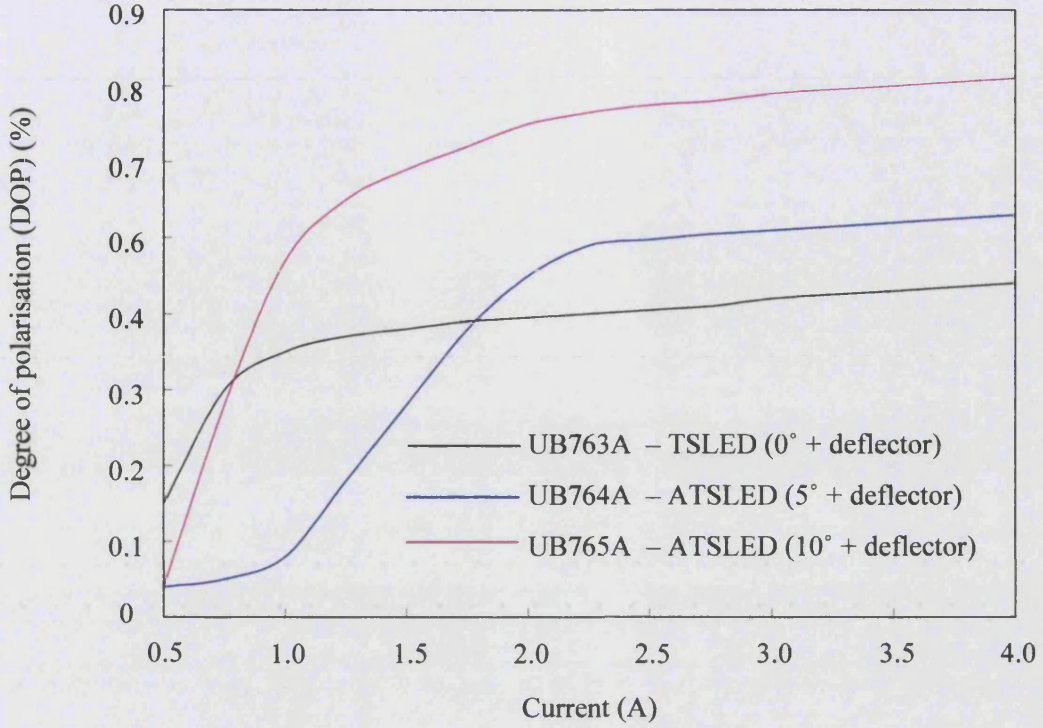

Figure 5.4: Measured degree of polarisation (DOP) of devices UB763A, UB764A and UB765A.

5.2.3 Lateral and Angular Intensity Distribution

- *Near-Field Intensity Distribution*

The near-field intensity distributions of the ATSLDs were also measured. Figures 5.5 and 5.6 shows the measured near-field profiles at several currents of devices UB764A (α = 5°) and UB765A (α = 10°). The near-field profiles obtained are asymmetric for both devices. It is also evident from the plots that the near-field profiles of the device with the larger inclination angle α is more asymmetric than the device with the smaller value of α. Note also that asymmetry in the near-field profiles for both devices becomes more acute with increase in current. The near-field profiles were measured using a x 10 objective lens with a small numerical aperture (NA) of 0.17.

To investigate if the observed asymmetric near-field profiles are only typical of ATSLDs, the near-field intensity distribution of a parallel stripe SLD (PSLD) UB1091 with an angular displacement $\alpha = 5°$ was also measured. The device was also measured using a x 10 objective lens with NA = 0.17. Device UB1091 is 50μm wide and 1mm long with an etched deflector distance $L_1 = 500\mu$m. Figure 5.7 shows the measured near-field profiles at various currents for UB1091. It can be seen from the plot the near-profiles obtained are also asymmetric.

The near-field profiles of the ATSLDs, UB764A and UB765A, were also compared with those from a head on taper (UB763A), given in Figure 5.8a. These profiles clearly show the increase in asymmetry with increase in α. To investigate if the observed asymmetric profile is the result of measuring these devices with a small NA lens, the near-field measurements were repeated using a larger NA lens. In this case, a x 40 objective lens with NA = 0.65 was used. Figure 5.8b shows the measured near-field profiles of the ATLDS and the TSLD (UB763A). Comparing Figure 5.8a and 5.8b one can see a significant improvement in the near-field profiles of the ATSLDs obtained with a large NA lens, i.e. the profiles are more symmetric.

Experimental results obtained have shown that the near-field profiles of angled devices, parallel or taper, when measured with a small NA lens are asymmetric. This can be explained by first considering that when there is significant gain in the devices, rays originating from the rear end of the device contribute significantly to the output power due to its long path length. In the case of the angled devices the longest rays radiate over large angles with respect to the normal of the facet and emerge from the output facet at even larger angles due to refraction. Therefore an objective lens with small NA, i.e. small light acceptance angle, is not able to capture these large angle rays successfully. As a consequence, asymmetric near-field profiles are obtained. To verify the hypothesis discussed above the ray model for ATSLDs using the ray analysis method have been developed, which is described in section 5.3.

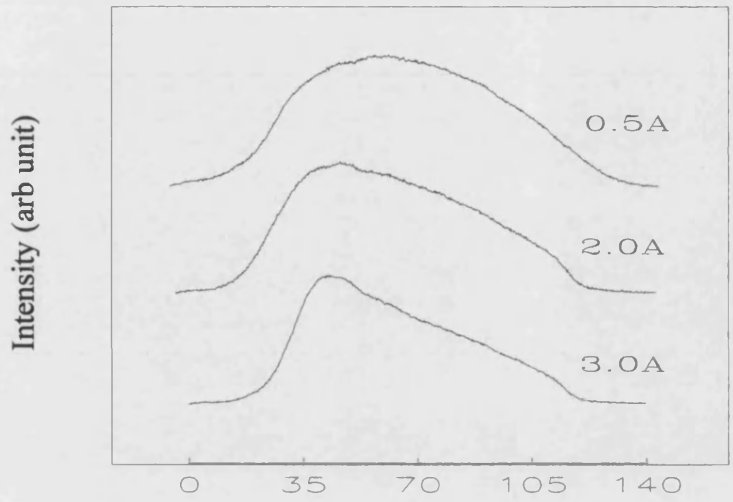

Figure 5.5
UB764A (ATSLD)
$\alpha = 5°$
NA = 0.17

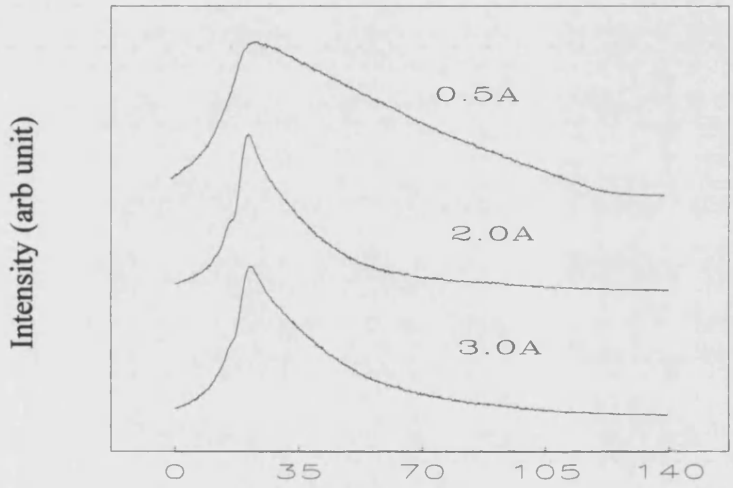

Figure 5.6
UB765A (ATSLD)
$\alpha = 10°$
NA = 0.17

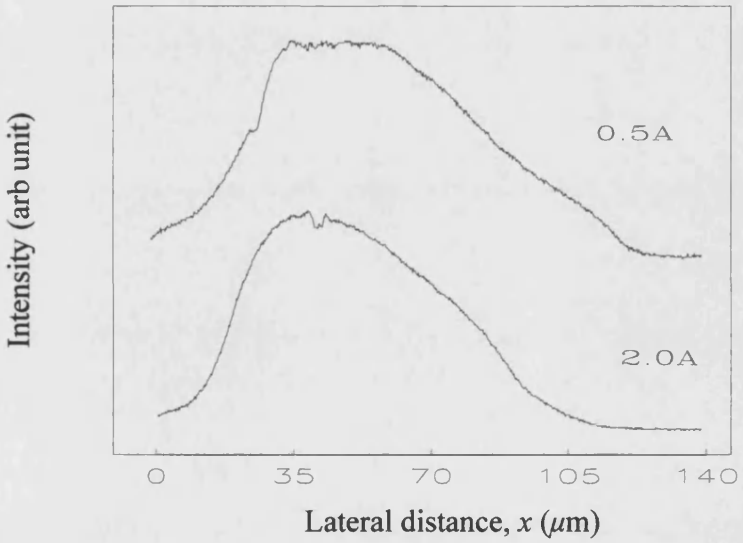

Figure 5.7
UB1091 (PSLD)
$\alpha = 5°$
NA = 0.17

Figure 5.5: Measured near-field profiles of ATSLD UB764A with NA = 0.17. Figure 5.6: Near-field profiles of UB765A. Figure 5.7: Near-field profiles of UB1091 with NA = 0.17.

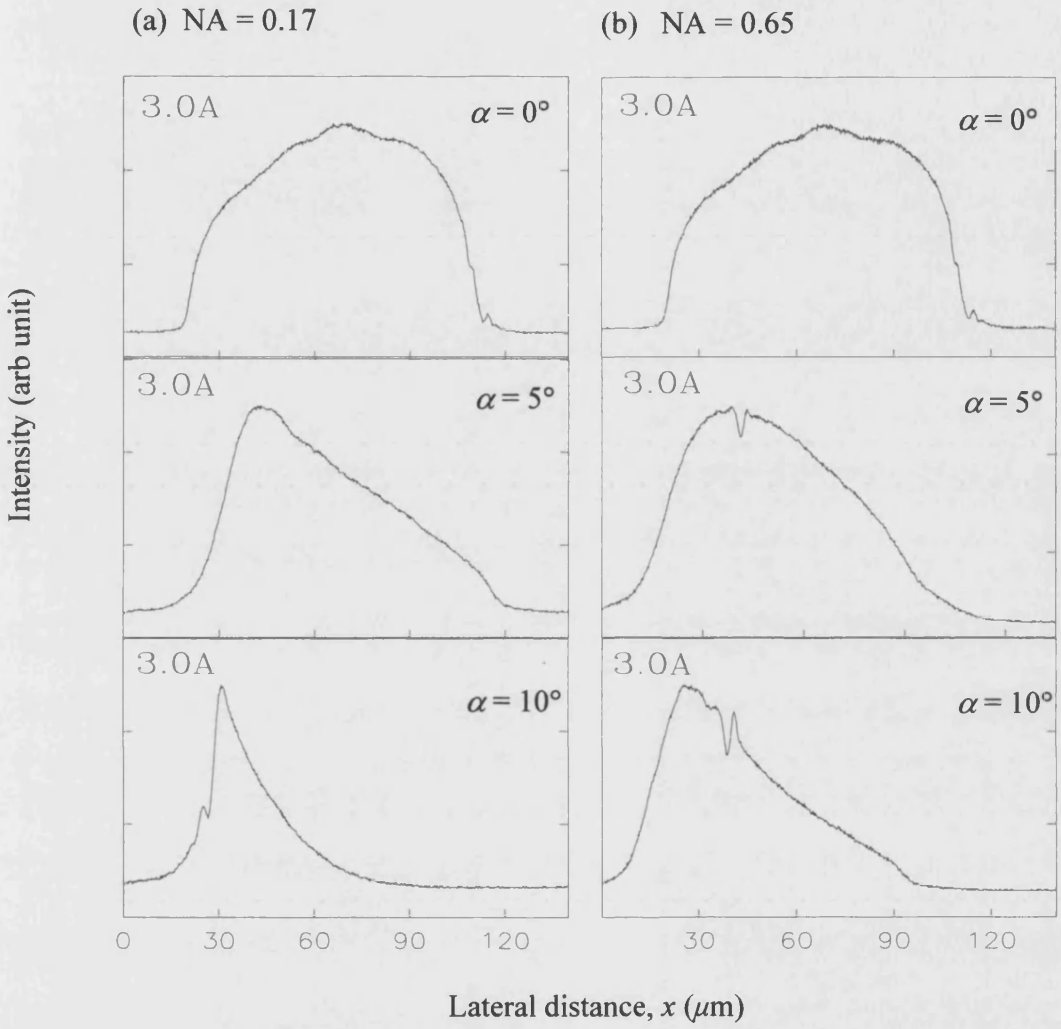

Figure 5.8: Near-field profiles of UB763A (0°), UB764A (5°), and UB765A (10°). (a) measured with lens NA = 0.17. (b) measured with lens NA = 0.65.

- *Far-Field Intensity Distribution*

Figure 5.9 shows the far-field profiles of devices UB763A (α = 0°), UB764A (α = 5°) and UB765A (α = 10°) measured at 3A. Unlike the head on taper UB763A the far-field profiles of the ATSLDs are not centred at 0°. The far-field profile for the device with an angular displacement α = 5° is centred at the refracted angle 17° and similarly for the device with α = 10° the peak of the far-field profile is centred at 35°. These results demonstrate that rays originating form the rear end of the device carry the most power and are essentially directed at the inclination angle (α) of the taper contact.

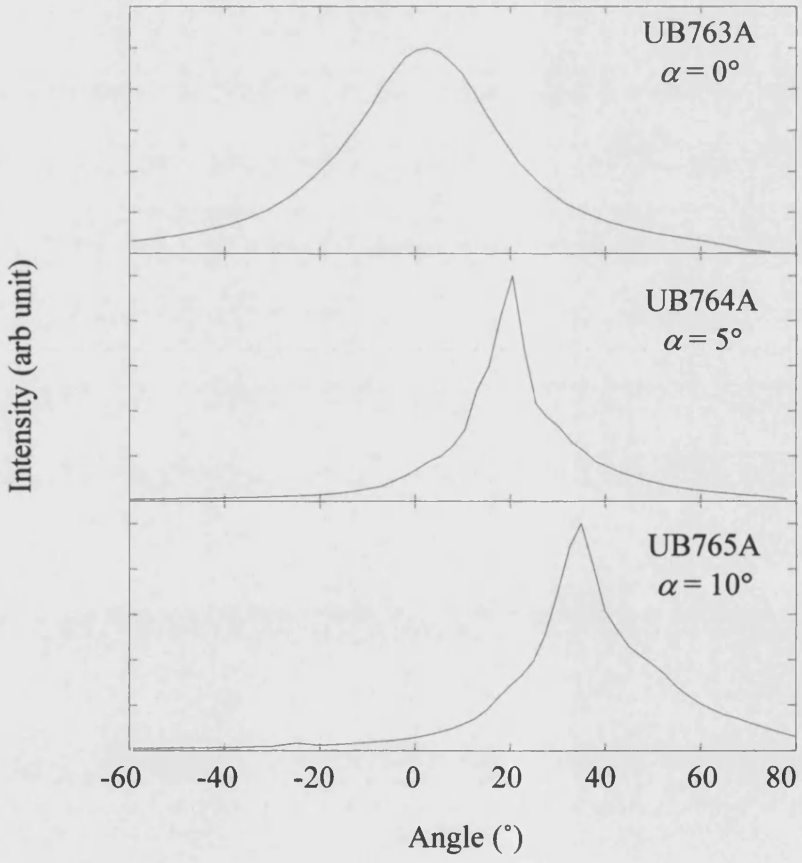

Figure 5.9: Far-field profiles of UB763A, UB764A and UB765A measured at 3A.

5.3 Ray Model for ATSLD

The ray model discussed in this section has been developed to estimate the near-field profiles of the ATSLDs across the output facet as a function of the NA of the objective lens used for collecting the output beam. For computational simplicity, approximations are used to reduce the problem to a one dimensional (lateral x) analysis. First, the effects of current spreading and diffusion are neglected. This meant that carrier density distribution is assumed to be constant throughout the taper shaped pumped region. Secondly, steady state conditions, $\frac{d}{dt}=0$ are assumed, and plane waves (ray optics) in the (x, z) plane of the junction. As has been discussed earlier in Chapter 3 in section 3.2, the advantage of assuming constant carrier density distribution is that the steady state rate equations, [10], have relatively simple analytic solutions.

The geometry of the problem is outlined in Figure 5.10, which presents the top view of the ATSLD. The shaded area represents the collection of rays that are captured by the objective lens. Figure 5.10 shows that the NA of the objective lens determines the maximum external collection angle θ_E, and consequently the internal collection angle θ_I at any point X on the output facet. The external and internal collection angle (θ_E and θ_I) is given by

$$\theta_E = \sin^{-1}(NA) \tag{5.2}$$

$$\theta_I = \sin^{-1}(\frac{\eta_1}{\eta_2}\overbrace{\sin\theta_E}^{NA}) \tag{5.3}$$

where η_1 is the refractive index of air and η_2 is the refractive index of the semiconductor material. At each point X on the output facet of the device and for each angle θ_s, which is the sweeping angle, it is possible to draw a ray of length $XJ = \hat{L}(X,\theta_s)$. In the formulation only forward travelling photons (+ve z direction) are considered. Therefore, defining s as the co-ordinate along the ray, and using the

photon rate equation (2.9) given in Chapter 2, the rate of change of the forward travelling photon density, $\tilde{P}(s,\theta_s)$, along the direction of the ray can be written as:

$$\frac{d\tilde{P}}{ds} = \frac{\tilde{g}(\overline{N})}{\upsilon}.P(s,\theta_s) + \delta_f \frac{\overline{N}}{\tau_{sp}\upsilon} \tag{5.4}$$

where $\overline{N}$ is the constant carrier density, $\tilde{g}(\overline{N})$ is the material gain, δ_f the fraction of spontaneous emission in the forward direction, τ_{sp} the is the spontaneous emission recombination lifetime and $\upsilon = \frac{c}{\eta_{mat}}$ the velocity of light in the semiconductor medium of refractive index η_{mat}.

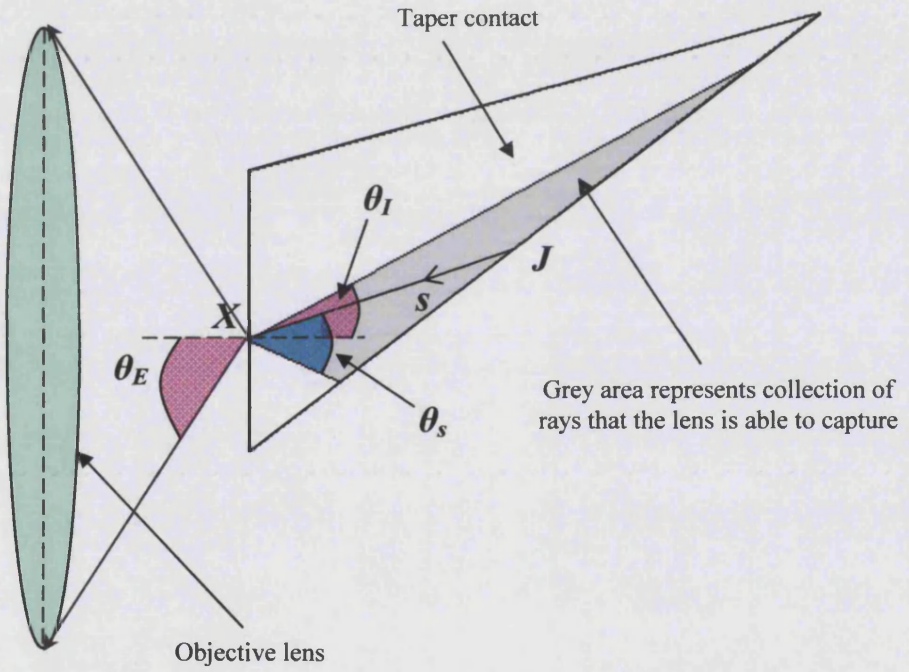

Figure 5.10: Schematic diagram of the ATSLD illustrating the external collection angle θ_E, internal collection angle θ_I and the sweeping angle θ_s.

From the derivation given in Appendix 3A it is known that the analytic solution to equation (5.4) takes the form;

$$\tilde{P}(s) = P_0 \exp\left(\bar{g}\hat{L}(X,\theta_s)\right) + \left(\exp\left(\bar{g}\hat{L}(X,\theta_s)\right) - 1\right)\overline{P}_{sp} \tag{5.5}$$

The first term in equation 5.5 represents stimulated emission and is ignored here since only spontaneous emission is considered.

To obtain the near-field intensity distribution across the output facet, the power for all the rays that are included in the shaded area must be summed at each point X on the output facet. With reference to Figures 5.11 and 5.12 at each point X there exist a limit angle $\theta_{lim} = \theta_{lim}(X)$, given by

$$\theta_{\text{lim}}(X) = \tan^{-1}\left(\tan(\gamma) + \frac{X}{L_c}\right) \tag{5.6}$$

and

$$\tan(\gamma) = \alpha + \frac{\theta_T}{2} \tag{5.7}$$

where W_{max} is the width of the output facet and L_c is the contact length. The limit angle θ_{lim}, may or may not divide the shaded (grey) area XT_1T_2 into two triangles, depending on the position X on the output surface. From this, two cases are distinguished, the first case refers to Figure 5.11 where $0 < \theta_I < \theta_{\text{lim}}$ and the second case refers to Figure 5.12 where $\theta_I > \theta_{\text{lim}}$. In the two cases two different expressions are derived for the length $\hat{L}(X,\theta_s)$ of the rays XJ. Applying the sine rule to triangle XBT_1 in figure 5.11 for the first case, $0 < \theta_I < \theta_{lim}$, we obtain;

$$\hat{L}(X,\theta_s) = X\frac{\sin(\varphi)}{\sin\left(\frac{\pi}{2} + \theta_I - \varphi - \theta_s\right)} \qquad 0 < \theta_s < 2\theta_I \tag{5.8}$$

where

$$\varphi = \frac{\pi}{2} - \theta_T - \phi \tag{5.9}$$

and

$$\phi = \alpha - \frac{\theta_T}{2} \tag{5.10}$$

Having found the expression for $\hat{L}(X,\theta_s)$ the output power $P(X)$ at each point X, in this case, is found by integrating equation (5.5) which takes the form:

$$P(X) = \int_0^{2\theta_I} \overline{P}sp(exp(\overline{g}\hat{L}(X,\theta_s) - 1)\, d\theta \tag{5.11}$$

Similarly for the second case $\theta_I > \theta_{lim}$, applying the sine to triangle XBT_2 in figure 5.12, we obtain;

$$\hat{L}(X,\theta_s)=\begin{cases} X\dfrac{sin(\varphi)}{sin\left(\dfrac{\pi}{2}+\theta_I-\varphi-\theta_s\right)} & 0<\theta_s<\theta_{lim} \\ (W_{max}-X)\dfrac{sin\left(\dfrac{\pi}{2}+\phi\right)}{sin(\theta_s-\theta_I-\phi)} & \theta_{lim}<\theta_s<2\theta_I \end{cases} \quad (5.12)$$

The output power $P(X)$, collected by the lens is calculated by summing the contributions of the rays XJ that are included in the shaded (grey) area of Fig. 5.12, given by:

$$P(X) = \int_0^{90°+\theta_{lim}} \overline{P}_{sp}(exp(\overline{g}\hat{L}(X,\theta_s)-1)\,d\theta + \int_{90°+\theta_{lim}}^{2\theta_I} \overline{P}_{sp}(exp(\overline{g}\hat{L}(X,\theta_s)-1)\,d\theta \quad (5.13)$$

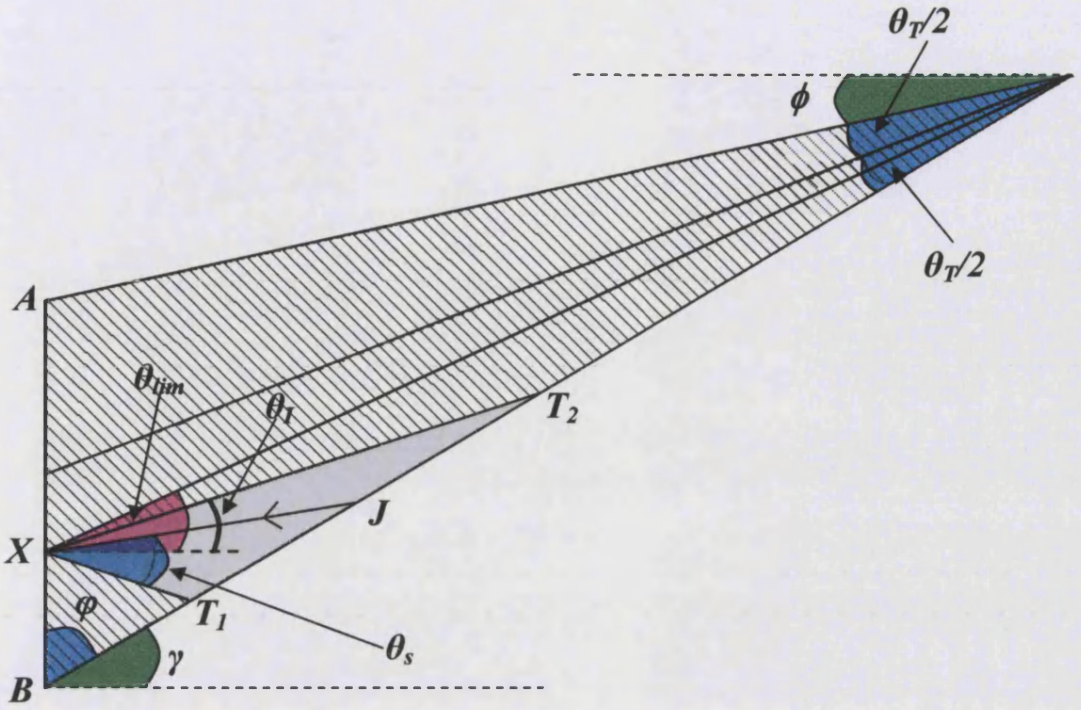

Figure 5.11: Schematic diagram of the geometry used in the ray model. Shaded (grey) area of angular spread $2\theta_I$ represent the rays that are collected by the lens: first case $0 < \theta_I < \theta_{lim}$.

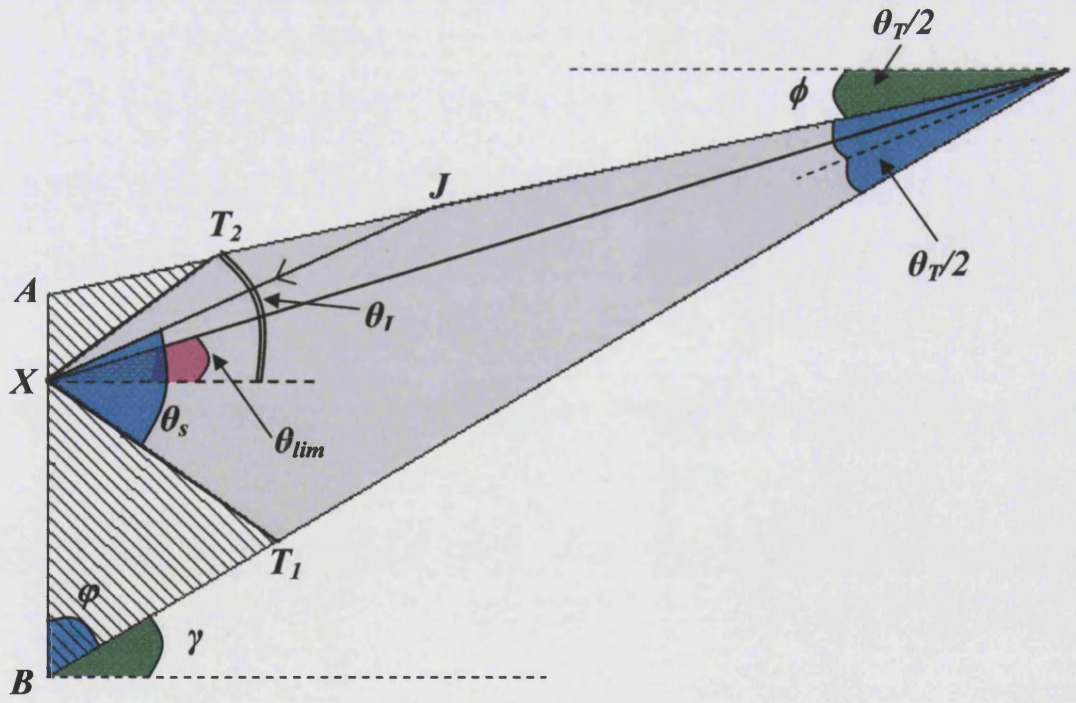

Figure 5.12: Schematic diagram of the geometry used in the ray–model. Shaded (grey) area of angular spread $2\theta_I$, which represent the rays that are collected by the lens: second case $\theta_I > \theta_{lim}$.

5.3.1 Simulation Results

The calculated near-field profiles of an ATSLD with an angular displacement $\alpha = 5°$, $W_{max} = 100\mu m$ and $L_c = 1000\mu m$ at several currents for NA = 0.17 and NA = 0.65 are shown in Figure 5.13 and Figure 5.14. The calculated near-field profiles are clearly asymmetric with the asymmetry increasing with increase in current, which concurs with the experimental results presented earlier. This can be explained by first considering the fact that at high currents the active region is now the entire length of the device. Therefore rays originating form the back end of the device, radiating over large or small angles, carry the most power compared to rays that originate near the facet. Unfortunately, rays radiating over large angles originating from the back are not efficiently captured by the lens. As a result the near-field profiles obtained at high currents is more asymmetric than that obtained at low currents.

Nonetheless, simulation results also show that the near-field profiles obtained with a large NA lens, either at low or high currents are more symmetric compared to those obtained with a small NA lens. This is because a large numerical aperture lens is able to capture more rays especially those that emerge at large refraction angles. In this case, an objective lens with NA = 0.17 has light acceptance angle (external capture angle), i.e. $\theta_E = 9.8°$. In comparison, an objective lens with NA = 0.65 has light acceptance angle $\theta_E = 40.5°$. Hence, with a large NA lens more rays are captured resulting in a more symmetric near-field profile.

In order to test the validity of the model two different experimental measurements were performed on the ATSLDs. The measurement techniques and the experimental results obtained are discussed in detail in section 5.4.

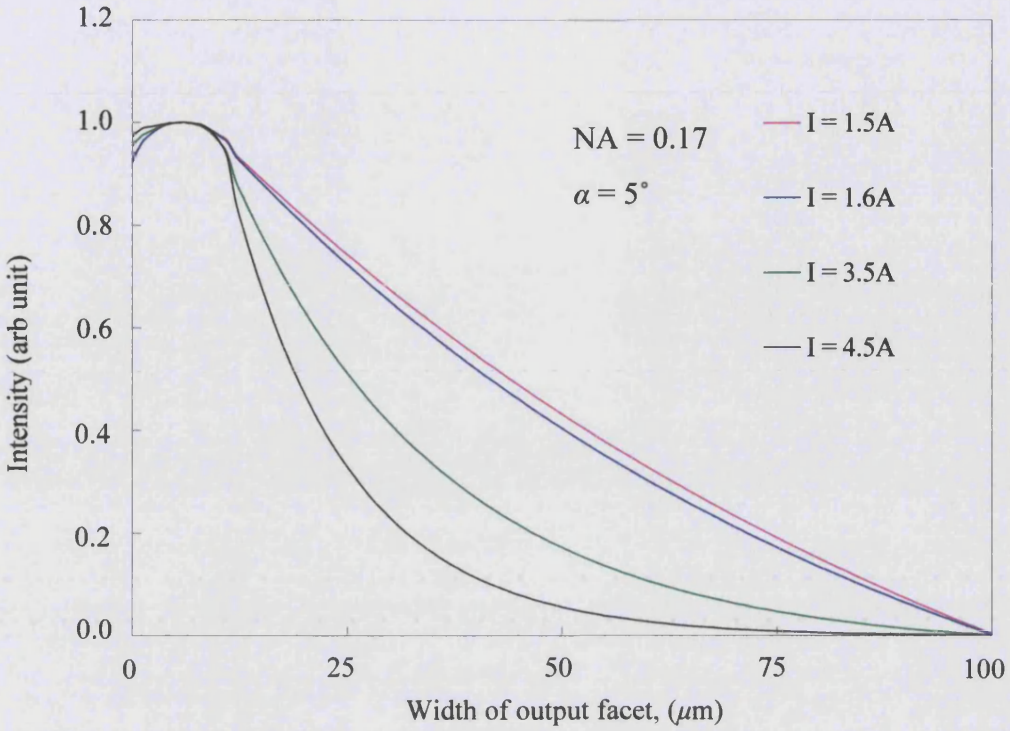

Figure 5.13: Calculated near-field profiles of an ATSLD with α = 5° and NA = 0.17 at several currents.

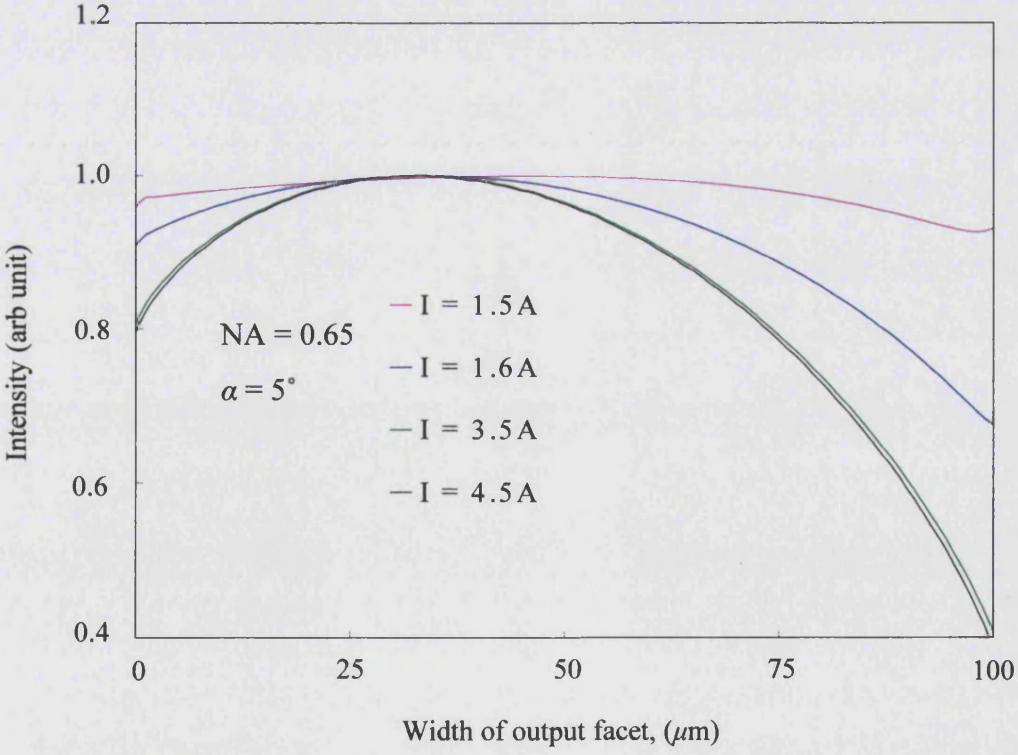

Figure 5.14: Calculated near-field profiles of an ATSLD with $\alpha = 5°$ and NA = 0.65 at several currents.

5.4 Validity of Ray Model

5.4.1 Experimental Near-Field Profiles at Low and High Currents

Figures 5.15 shows the measured near-field profiles for device UB764A ($\alpha = 5°$) at low currents (500mA) with NA = 0.17 along with curves calculated by the model. Figure 5.16 show similar results for UB764A with NA = 0.65. The solid curve represents the experimental result and the dashed curve represents the theoretical result. Reasonably good agreement can be seen between the experimentally measured near-field profiles and those predicted by the model. Examining the near-field profiles more closely and comparing profiles from Figure 5.15 with Figure 5.16, one can see that the difference in asymmetry is not significant. As has been discussed in section 5.3.1, at low currents much of the rays from the back suffers heavy attenuation and thus do not contribute significantly to the output power.

Figures 5.17, 5.18, 5.19 and 5.20 shows the measured near-field profiles of devices UB764A and UB765A at high currents (3A) with NA = 0.17 and NA = 0.65 respectively. The dashed curves in these Figures show the near-field profiles calculated from the model. It can be seen from the graphs plotted that exact matches between the experimental curves and the theoretical curves have not been obtained. The disparity between experiment and theory is due to the fact that current spreading, carrier diffusion and hole-burning effects have not been included in the model. Nevertheless, the theoretical model does predict the trend of the near-field profiles quite well.

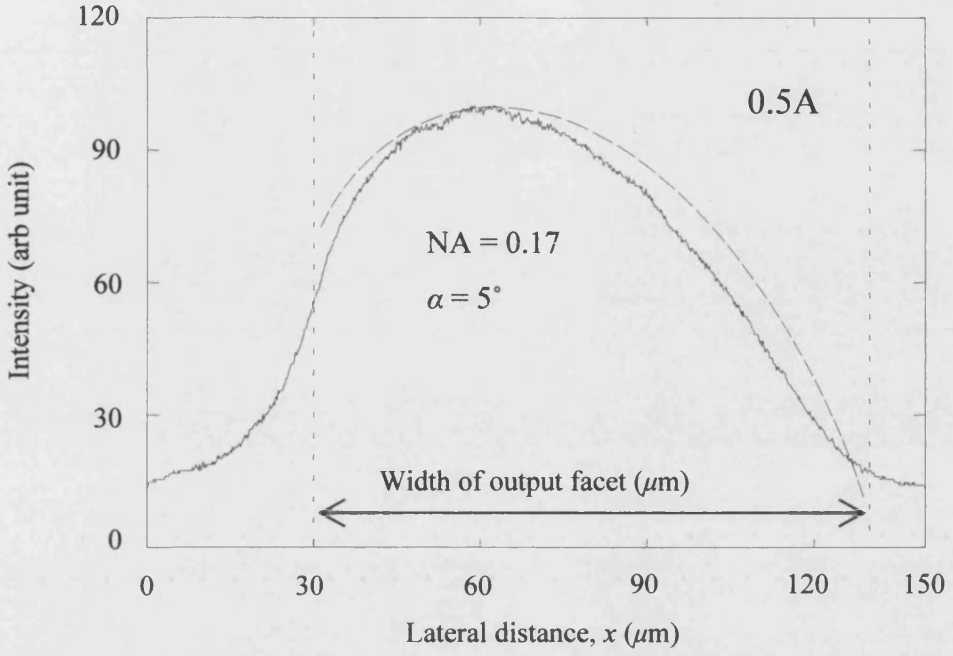

Figure 5.15: Measured near-field profile of UB764A at 0.5A using an objective lens with NA = 0.17. Solid curve – experimental. Dashed curve – theoretical.

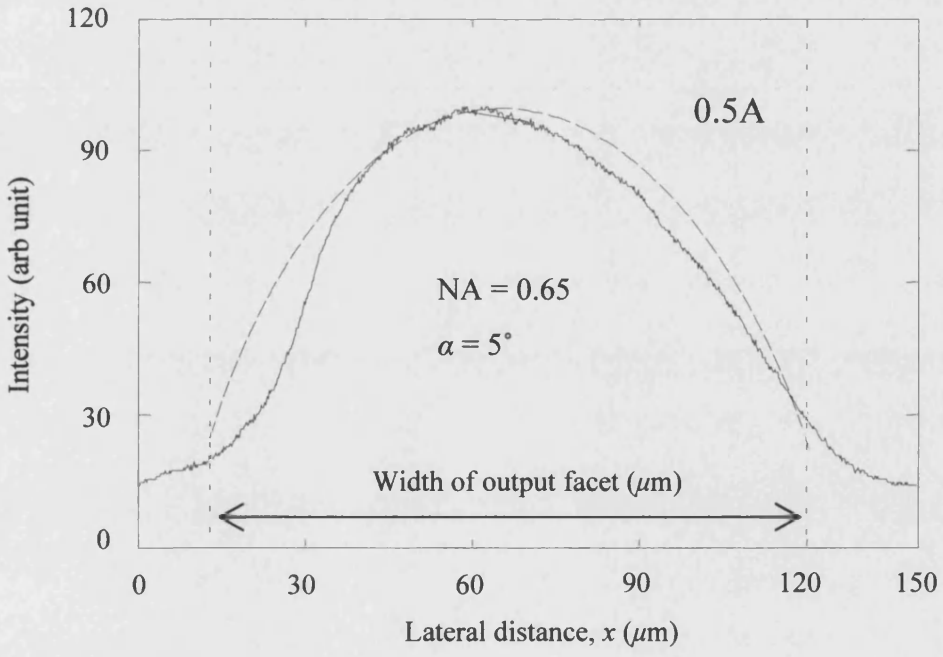

Figure 5.16: Measured near-field profile of UB764A at 0.5A using an objective lens with NA = 0.65. Solid curve – experimental. Dashed curve – theoretical.

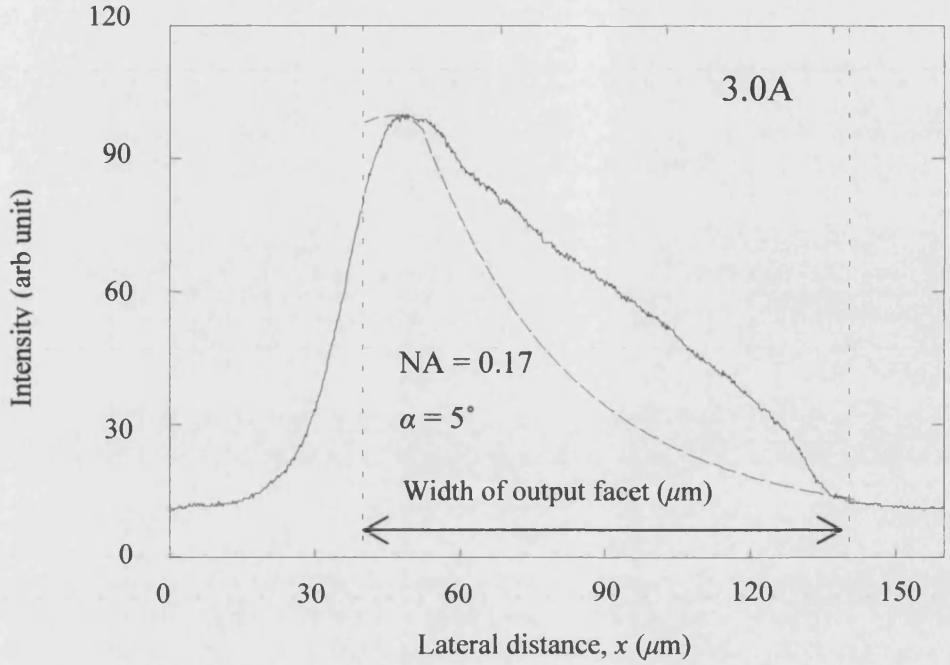

Figure 5.17: Measured near-field profile of UB764A at 3.0A using an objective lens with NA = 0.17. Solid curve – experimental. Dashed curve – theoretical.

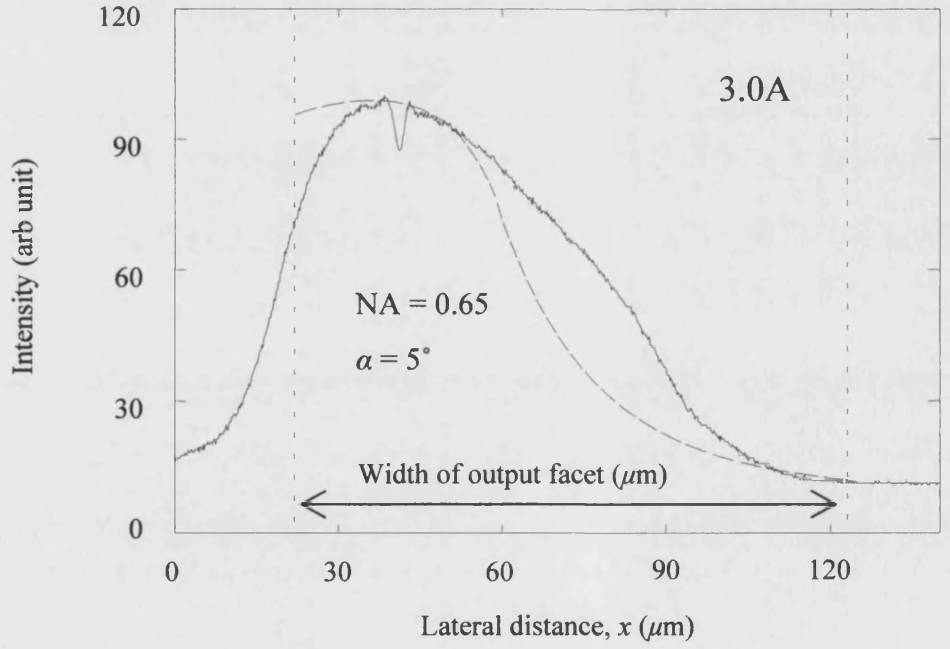

Figure 5.18: Measured near-field profile of UB764A at 3.0A using an objective lens with NA = 0.65. Solid curve – experimental. Dashed curve – theoretical.

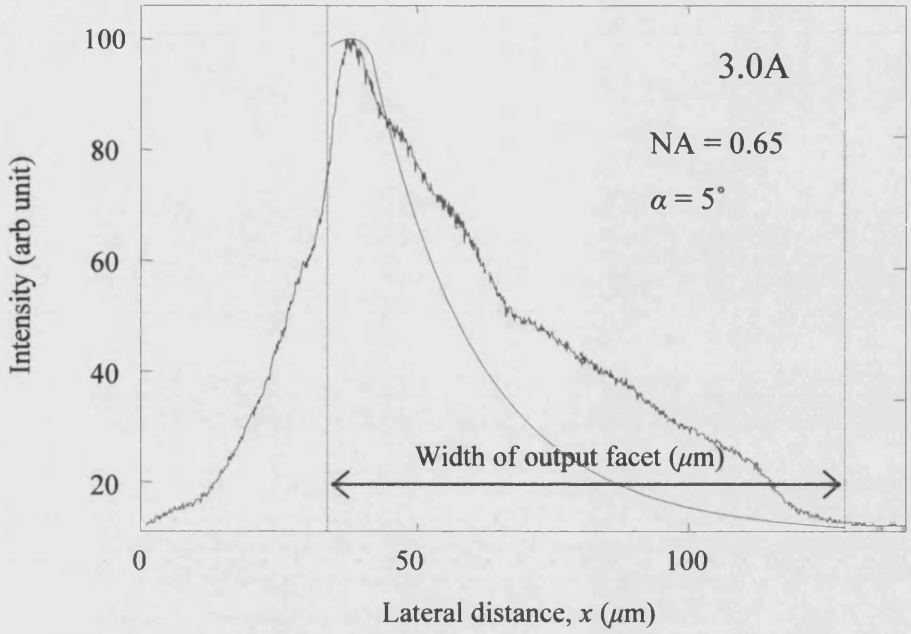

Figure 5.19: Measured near-field profile of UB765A at 3.0A using an objective lens with NA = 0.17. Solid curve – experimental. Dashed curve – theoretical.

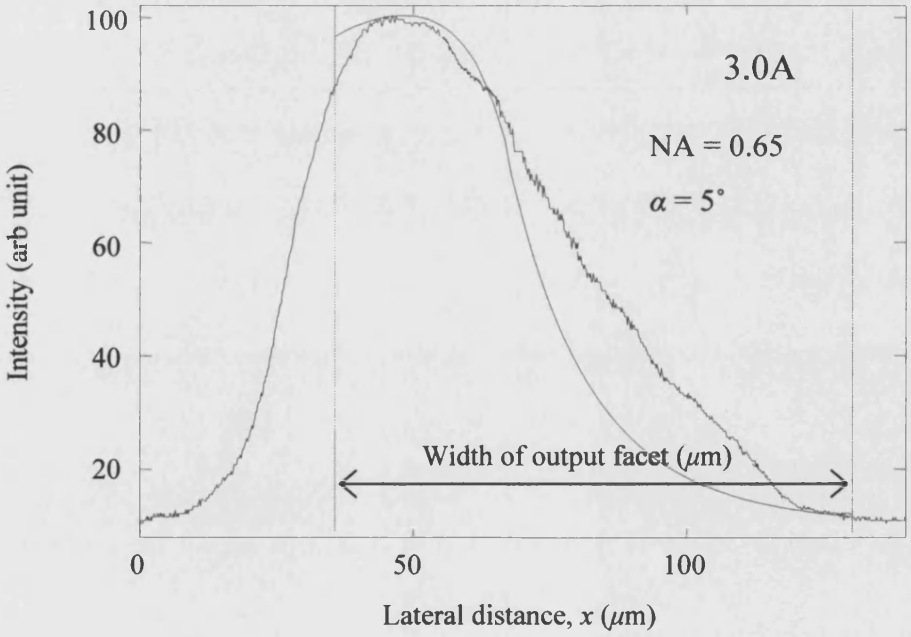

Figure 5.20: Measured near-field profile of UB765A at 3.0A using an objective lens with NA = 0.65. Solid curve – experimental. Dashed curve – theoretical.

5.4.2 Spectrally Resolved Near-Field Profiles

To further test the validity of the model, spectrally resolved near-field intensity measurements was performed on device UB1021 ($\alpha = 5°$). It is common knowledge that LEDs have a broad emission spectrum and that the material gain, $g(N)$ is also wavelength dependent, $g(N,\lambda)$. Hence, the near-field profiles of LEDs can be measured at several wavelengths that correspond to rays of light with high or low gain. Typical spontaneous emission spectrum at several currents for device UB1021 can be found in Appendix 5A. With reference to the emission curves in Appendix 5A, the near-field intensity distribution of device UB1021 was measured at three different wavelengths, λ = 869nm, 873nm and 876nm.

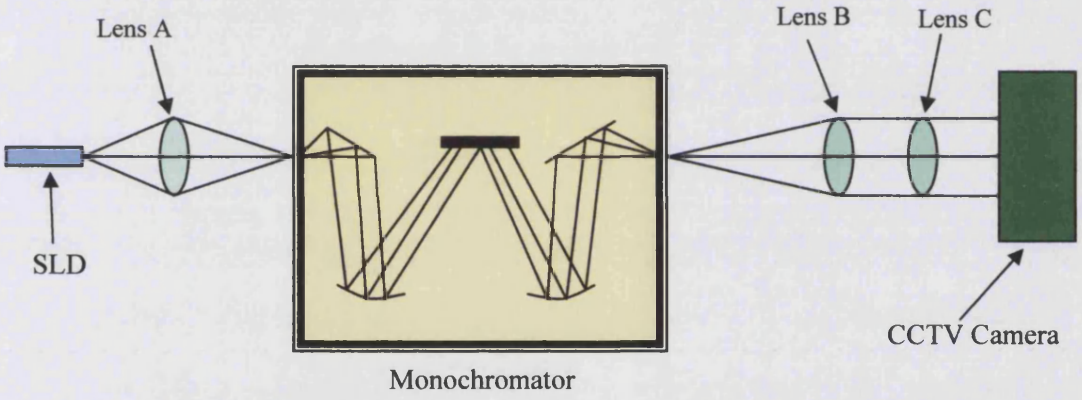

Figure 5.21: Experimental apparatus used for spectrally resolved near-field measurements.

The experimental apparatus used in this experiment is shown in Figure 5.21. For the spectrally resolved near-field intensity measurements a monochromator was placed between lenses A and B. For the first set of measurements, a x 10 objectives lens with NA = 0.17 (lens A) was used to collect the light from the front facet of the device at the entrance slit of the monochromator. The x 40 objective lenses with NA = 0.65 (lens B and C) was then used to collect the light form the output end of the monochromator and focus it onto the vidicon camera. For the second set of measurements, the x 10 objectives (lens A) was replaced with a x 40 objective lens with NA = 0.65.

Figure 5.22 shows the near-field profiles of device UB1021 ($\alpha = 5°$) measured using an objective lens with NA = 0.17 (lens A) at 3A. It can clearly be seen that at the peak of the emission spectrum (λ = 869nm), i.e. rays with long path lengths the near-field profile is very asymmetric. At this wavelength, rays radiating over small or large angles originate from the rear of the device carry the most power and contribute significantly to the output profile. However, due to the small NA of lens A, rays radiating over large angles are not effectively captured. As a consequence, the near-field profile obtained at this wavelength is asymmetric. In contrast, when the near-field intensity distribution of device UB1021 was measured at λ = 876nm, i.e. rays with short path lengths, a near-symmetric profile is obtained. This is because rays that radiate over small or large angles originating near the output facet carry very little power and do not contribute significantly to the output profile.

Figure 5.23 shows similar results for device UB1021, measured using an objective lens with NA = 0.65 (lens A). As expected at the peak of the emission spectrum (λ = 869nm) the near-field profile is very asymmetric and near the minima of the emission spectrum (λ = 876nm) the near-field profile is more symmetric. Note that the near-field profiles obtained with a large NA lens is more symmetric even at high currents than that obtained with a small NA lens, Figure 5.22. As has been discussed earlier, an objective lens with a big numerical aperture is able to efficiently capture rays that radiate over large angles, which results in a more symmetric near-field profile.

In general this experiment demonstrates that a symmetric near-field profile can be obtained with a small NA lens by measuring the intensity distribution at the appropriate wavelength. More importantly these results concur with the experimental and theoretical results presented in section 5.4.1.

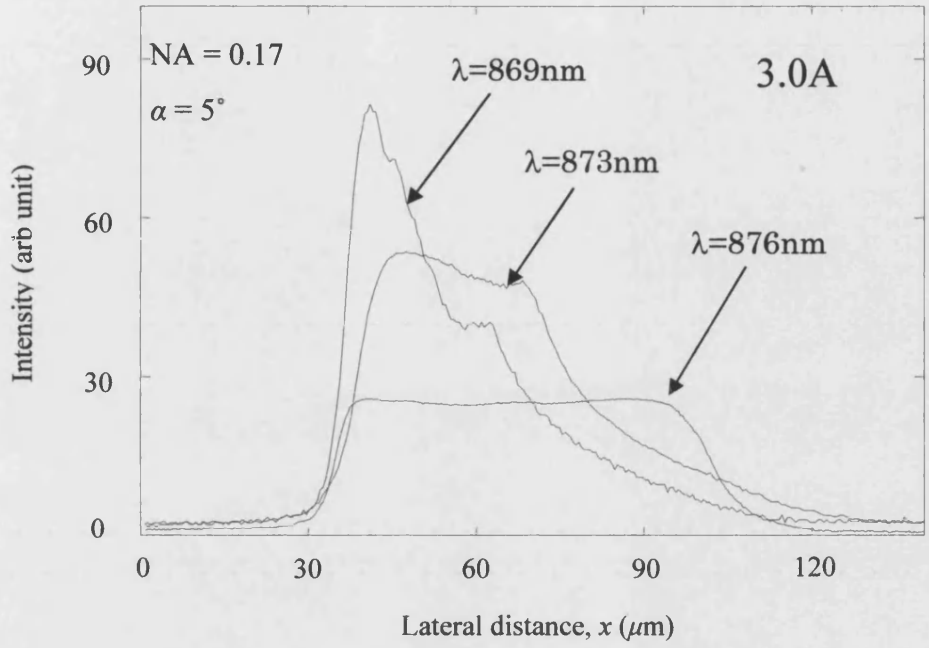

Figure 5.22: Spectrally resolved near-field profiles of ATSLD UB1021 with NA = 0.17 at 3A.

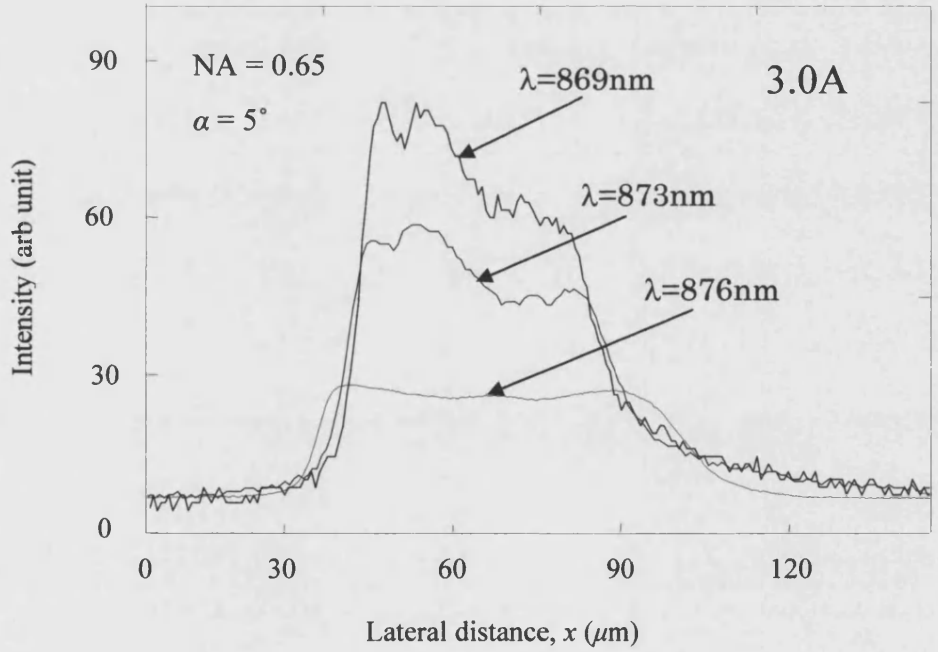

Figure 5.23: Spectrally resolved near-field profiles of ATSLD UB1021 with NA = 0.65 at 3A.

5.5 Conclusions

The angular displacement of the tapered contact SLD has proved to be a very efficient way of reducing unwanted optical feedback from the front facet from re-entering the active region. The experimental results presented in this chapter confirms that ATSLDs produce high output powers that are comparable to those achieved by A-R coated TSLDs (from previous chapter), but with the advantage of relatively simple fabrication process. Over 550mW has been obtained from the device with an angular displacement $\alpha = 10^{\circ}$ (UB765A), which is more than that obtained from a head on taper UB763A with front facet reflectivity of about 2% (after A-R coating).

Disconcertingly, asymmetric near-field profiles of ATSLDs were obtained, when measured with a small NA lens. Interestingly, asymmetric near-field profiles have not been reported by other research groups [3], [4], mentioned earlier in the introduction of this chapter. The ray model developed demonstrated that the observed asymmetry is in actual fact the discriminating effect of the gain and the use of a small numerical aperture (NA) lens when measuring the near-field profiles of angled TSLDs. Theoretical results from the model for small and large NA lenses at low currents are shown to match well with experimental results. However, at high currents the theoretical profile does not closely match the experimental results. This is due to several factors. The ray model developed assumed constant carrier distribution both laterally and longitudinally. It has been shown in chapter 2 that the carrier distribution in tapered geometry devices varies quite considerably, particularly in the longitudinal direction. Furthermore, hole-burning effects or carrier deletion that occurs at the rear of the device, as has been demonstrated in chapter 3, is not included in the model. Nevertheless, the model does predict the trend of the near-field profiles quite well. In addition, the spectrally resolved near-field profiles obtained at several wavelengths further verified the theoretical and experimental findings.

References

[1] *M. C. Amann, J. Boeck*, **'High-Efficiency Superluminescent Diodes for Optical-Fibre Transmission'**, Electronic Letters, Vol. 15, No. 2, pp. 41-42, 1979.

[2] *I.Middlemast, J. Sarma, T. Kambayashi*, **'A Comprehensive Study and Characterisation of Superluminescent Light Emitting Diodes'**, IEEE Specialist Conference on Light Emitting Diodes and Photodetectors, 1982, Paper (21), Ottawa, Canada, 1982.

[3] *Gerard A. Alphonse, Dean B. Gilbert, M. G. Harvey, M. Ettenberg*, **'High Power Superluminescent Diodes'**, IEEE Journal of Quantum Electronics, Vol. 12, No 12, pp. 2454-2457, 1988.

[4] *Toru Takayama, Osamu Imafuji, Yasuyuki Kouchi, Masaaki Yuri*, **'100-mW High-Power Angled Stripe Superluminescent Diodes with a New Real Refractive-Index-Guided Self-Aligned Structure'**, IEEE Journal of Quantum Electronics, Vol. 32, No. 11, pp. 1981-1986, 1996.

[5] *G. H. B. Thompson*, **'Physics of Semiconductor Laser Devices'**, John Wiley and Sons, 1980.

[6] *T. P. Lee, C. A. Burrus, B. I. Miller*, **'A Stripe-Geometry Double-Heterostructure Amplified Spontaneous Emission (superluminescent) diode'**, Journal of Quantum Electronics, Vol. QE-9, No. 8, pp. 820 – 827, 1973.

[7] *W. Streifer, D. R. Scifres, R. D. Burnham*, **'Analysis of Laser Diode Properties'**, IEEE Journal of Quantum Electronics, Vol. QE-18, No. 11, pp. 1918 - 1929, 1982.

[8] *W. Streifer, D. R. Scifres, R. D. Burnham*, **'Analysis of Spontanoues Emission Effects on Spectra and *L* vs *I* Characteristics of Diode Lasers'**, Japanese Journal of Applied Physics, Vol. 21, pp. L282-284, 1982.

[9] *H. Kressel and J. K. Butler*, **'Semiconductor Lasers and Heterojunction LEDs'**, New York: Academic, p. 556, 1977.

Chapter 6
Comprehensive Ray Model

6.1 Introduction

A number of assumptions were made in the ray model discussed in the previous chapter. One of which is the assumption of the uniformity of carrier density and gain distribution throughout the device. Hence, it was possible to obtain a closed form solution to the photon rate equation. In reality however, the carrier density and gain distribution in a device is not uniform. As has been discussed in Chapter 2 the carrier density distribution is determined by current spreading and carrier diffusion [1]. In order to accurately predict the spatial characteristics (near-field and far-field intensity distribution) of SLDs these factors must be taken into account.

In this chapter, extension of the ray model to include lateral and longitudinal distribution of carriers is discussed. The advantage with including the lateral and longitudinal distribution of carriers is that it allows SLDs of various geometric shapes, in the context of this research, parallel stripe, tapered and angled tapered SLDs, to be analysed. The model (non-uniform carrier density) studies both the near and far-field profiles and incorporates in-situ measured parameters. Simulation results obtained from the two methods, assuming uniform and non-uniform carrier density distribution, are compared. Finally some experimental results from parallel stripe, tapered and angled tapered SLDs are presented and comparisons made with those predicted from the comprehensive ray model.

6.2 Description of the Non-Uniform Ray Model

The ray model has been extended to include the complexity of both lateral (x) and longitudinal (z) distribution of carriers, which is particularly inherent in tapered geometry SLDs. Figure 6.1 shows a schematic diagram from the top, of a tapered geometry SLD and the typical carrier density distribution in the device. In order to include the non-uniform (x, z) distribution of carriers in the device, the lateral carrier density distribution $N(x)$ must be found at every step along the length (z direction) of the device. Hence, the effects of current spreading and carrier diffusion, which determines the carrier distribution in a device, must be included.

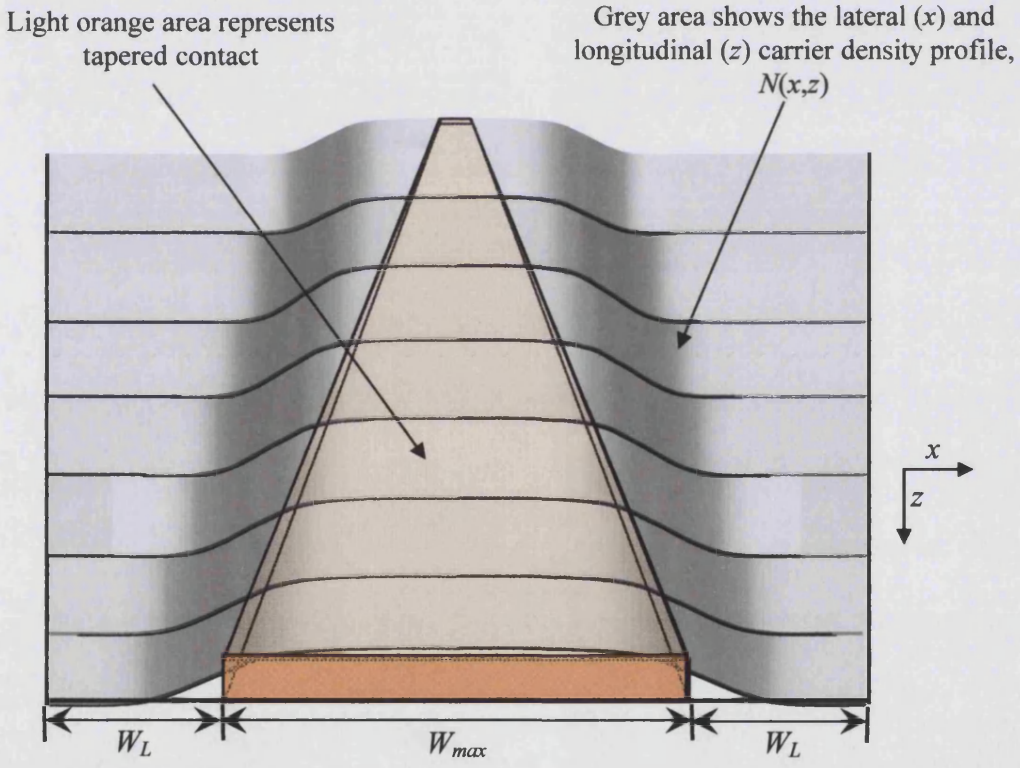

Figure 6.1: Schematic diagram from the top illustrating the lateral and longitudinal carrier density variation in a tapered geometry SLD.

The carrier distribution $N(x)$ at all z can be obtained from the current spreading model which incorporates in-situ measured parameters (refer to section 2.4 of chapter 2). Unfortunately there is a disadvantage to using the current spreading model to obtain the lateral carrier density distribution at every point along the length of the device. This method is computationally demanding, given that it would involve calculating and storing large amounts of data. From the literature however, it was found that Kambayashi [2] in his model used a simple analytic expression to represent the lateral carrier distribution $N(x)$. Satisfactory results were obtained with this approach and as a result a similar approach was adopted for this work. It should be noted that the longitudinal (z) variation of carriers were not included in [2], therefore the model is restricted to only analysing parallel stripe SLDs.

In the ray model a super-gaussian function was used to represent the lateral carrier density profile $N(x)$ at all z, which is given by

$$N_{sg}(x,z)=N_{max}e^{-\left(\frac{X}{W_c(z)}\right)^m} \tag{6.1}$$

and

$$N_{max}=\sqrt{\frac{J}{qdB_r}}$$

N_{sg} - is the super-gaussian carrier density profile
N_{max} - maximum value of the carrier density
J - injected current density
$W_c(z)$ - is the carrier density profile width at e^{-1} from N_{max} at each z
m - (integer) super-gaussian exponent

In equation (6.1), W_c determines the width and the exponent m determines the shape of the super-gaussian profile. In this model, the parameter W_c and m is adjusted until the super-gaussian (S-G) profile matches the carrier density profile obtained from the current spreading model. It has been found that in trying to match the S-G profile to the carrier density profile of a tapered geometry SLD, parameters W_c and m, has a linear relationship with z. Hence it has been possible to represent this linear relationship with an analytic expression. As a result the appropriate values of W_c and m at each z can be easily obtained, which provides a large saving on computation

time. Note, that when modelling parallel stripe SLDs W_c and m remains constant for all z.

With $N(x,z)$ known the near and far-field intensity profiles for these devices can be calculated. Figure 6.2 outlines the geometry of the problem. The area under consideration is taken to be rectangular in shape, which includes the lateral extent of the carrier distribution. This is feasible since it is the carrier density profile that ultimately determines the actual shape of the device, whether parallel or taper. In Figure 6.2, W_L is chosen to be at the point where the value of the carrier density drops down to about 0.01% from the maximum value.

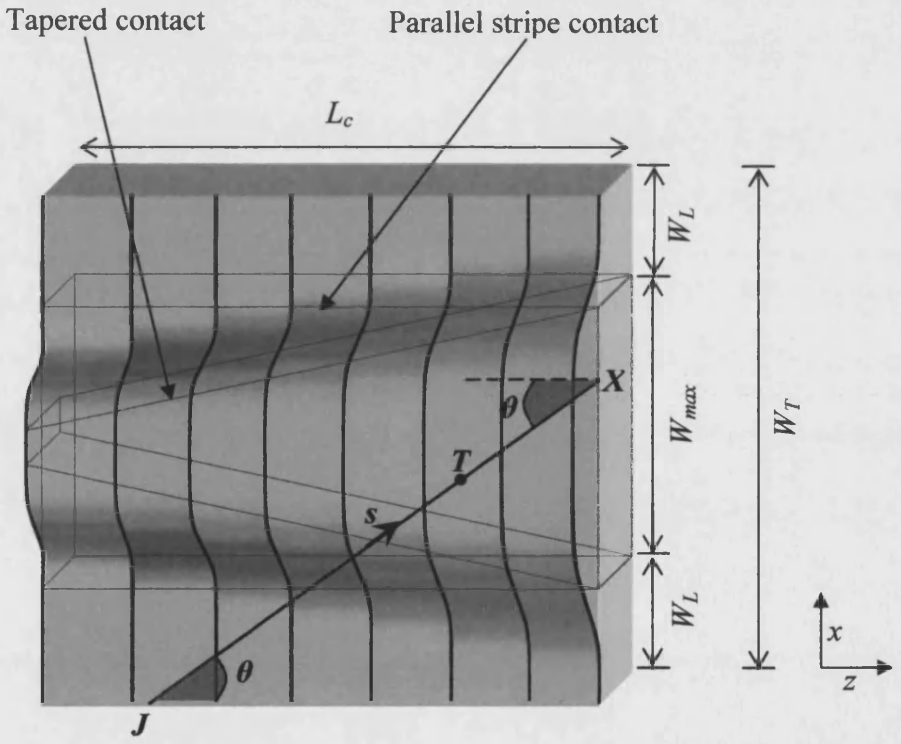

Figure 6.2: Illustrates the geometry of the problem.

At each point X on the front facet of the device and for each angle θ, a ray of length $\hat{L}_s(X, \theta)$ can be drawn, which is the distance between J and X. Defining $s = \bar{s}_{x,z}$ as

the co-ordinate along the ray under consideration, the rate of change of the forward travelling photon density $\hat{P}(s,\theta)$, is given by

$$\frac{d\hat{P}}{ds} = g(N(s,\theta)) \cdot \hat{P}(s,\theta) + \delta \frac{N(s,\theta)}{\tau_{sp} \upsilon} \tag{6.2}$$

where $N(s,\theta)$ is the carrier density distribution in the active layer, $g(N(s,\theta))$ is the optical gain in the medium, δ is the fraction of spontaneous emission in the forward direction, τ_{sp} is the spontaneous recombination time and υ is the velocity of light in the medium.

Given that the carrier profiles are expressed in terms of x and z, points on the ray s must also be expressed in terms of x and z co-ordinate. In general the x and z co-ordinate for any point, e.g. T in Figure 6.2, along the ray s, is given by:

$$z = L_c - (\hat{L}_s(x,\theta) - T).\sin\theta \tag{6.3}$$

$$x = X - (\hat{L}_s(x,\theta) - T).\cos\theta \tag{6.4}$$

The power $\tilde{P}_\theta(X)$ carried by each ray of length $\hat{L}_s(X,\theta)$ is found by integrating equation [6.2] along the ray itself, which takes the form:

$$\tilde{P}_\theta(X) = \int_0^{\hat{L}_s(x,\theta)} \hat{P}(s,\theta)\, ds \tag{6.5}$$

Due to the non-uniformity of the carrier and gain distribution equation (6.5) is solved numerically.

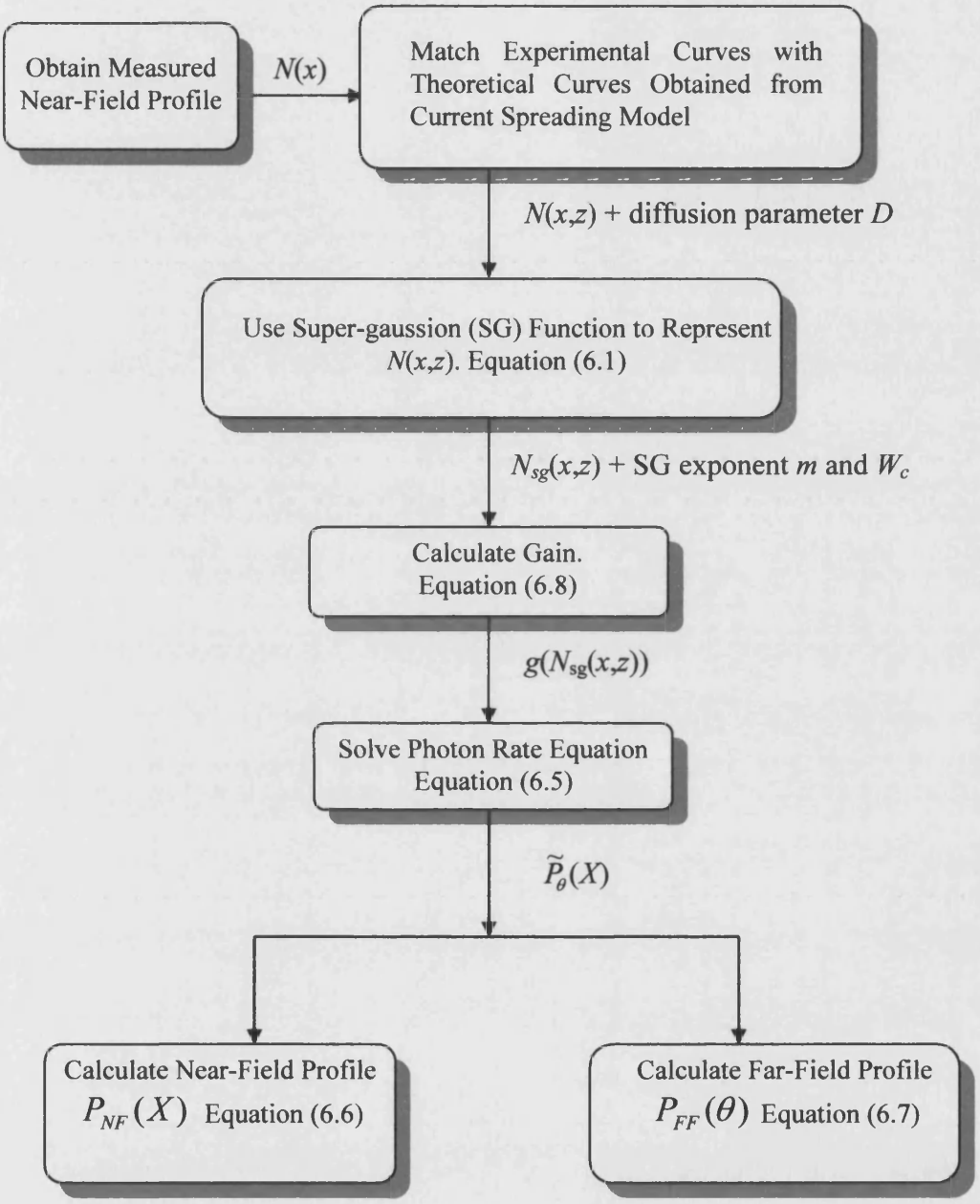

Figure 6.3: Flow diagram of the numerical procedure to calculate the near and far-field profile of parallel stripe, tapered geometry SLDs and angled tapered SLDs.

The numerical procedure followed to calculate the near and far-field profiles is shown in Figure 6.3. First, the experimentally measured profile is matched with the calculated carrier profile obtained form the current spreading model. From this the diffusion parameter D is obtained and the carrier density profile $N(x)$ at all z is found. Next the super-gaussian profile is matched with the calculated carrier profile. Having obtained the appropriate values for m and W_c, the lateral carrier density profile at every z is then plotted with the super-gaussian function.

The S-G profile, $N_{sg}(x,z)$, obtained, is then used to calculate the local gain which is given by:

$$g(x,z) = \Gamma_v \times \alpha_0(N_{sg}(x,z) - N_T) \tag{6.8}$$

where Γ_v is the vertical mode confinement factor, α_0 is the gain constant and N_T is the transparency current density.

The power $\tilde{P}_\theta(X)$ carried by each ray is then calculated by numerically integrating equation (6.5). Finally, having obtained $\tilde{P}_\theta(X)$, the near and far-field profiles are calculated. The near-field is simply the total intensity distribution across the output facet given by the following

$$P_{NF}(X) = \sum_{-\theta_A}^{+\theta_A} \tilde{P}_\theta(X) \tag{6.6}$$

where θ_A = internal lens NA angle. It is worth mentioning here that $\theta_A < \theta_{tir}$, which is the total internal reflection angle give by:

$$\theta_{tir} = \sin^{-1}\frac{1}{\eta_1}$$

where η_1 is the refractive index of the active region. The far-field, which is the angular distribution of the output beam is given by:

$$P_{FF}(\theta) = \int_0^{W_T} \tilde{P}_\theta(X)\,dX \tag{6.7}$$

6.3 Validity of the Super-Gaussian Approximation

In order to test the validity of the super-gaussian approximation a comparison was made between this method and the current spreading model. For completeness the calculated profiles are also compared with the experimentally measured carrier distribution. Simulations from the current spreading model are based on material QT503A. Parameters used in the simulation can be found in section 2.4 of chapter 2.

Figure 6.4 shows the experimentally measured carrier profile of a parallel stripe SLD (UB1027) at 1A and the calculated profiles (current spreading and super-gaussian). The device is 50μm wide and 1000μm long. As expected there is little difference between the experimentally measured profiles and the calculated carrier profiles obtained form the current spreading model. More importantly, the super-gaussian profile is found to match quite well with the experimental and calculated profile.

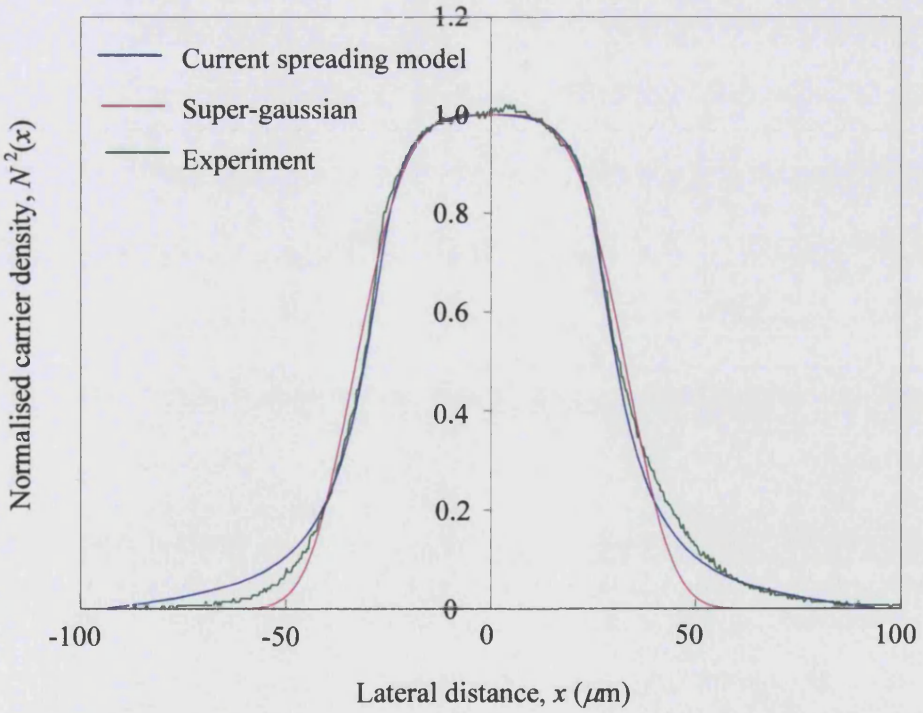

Figure 6.4: Comparison of the experimentally measured carrier profile of PSLD UB1027 and the calculated profiles. Device is 50μm wide and 1000μm long. Super-gaussian exponent m = 8.

The super-gaussian approximation was also tested on tapered contact SLD. Figure 6.5 shows the experimentall carrier density profiles at the output facet of a TSLD (UB1037Y) and the calculated profiles measured at 1A. Once again the S-G profile is found to match quite well with the experimental and calculated profile. The calculated near-field profile of the TSLD from the current spreading model and the super-gaussian method at the narrow end of the taper is also shown in Figure 6.6. It is clear that a fairly good match is obtained between the calculated carrier profile and the S-G approximation method even at the narrow end of the taper. In general the S-G approximation provides a fast and effective method of obtaining the carrier density profile at any point along the longitudinal z direction. The saving in computation time becomes even more significant when modelling taper SLDs rather than parallel stripe SLDs due to the longitudinal variation of carrier density distribution.

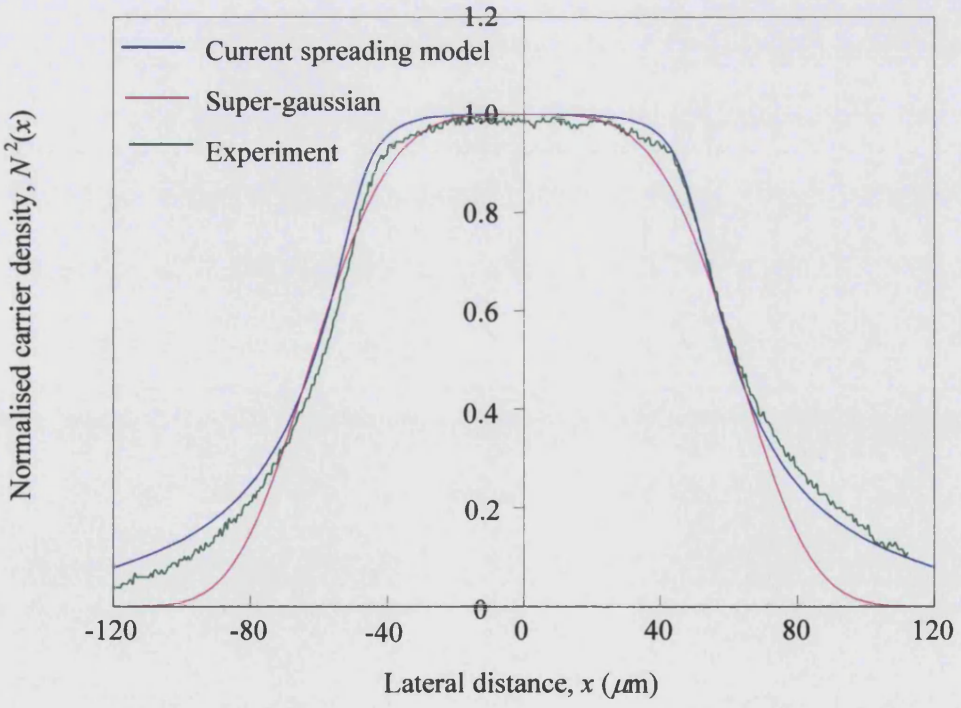

Figure 6.5: Comparison of the experimentally measured carrier profile of TSLD UB1037Y and the calculated profiles. W_{max} = 100μm wide and 1000μm long. Super-gaussian exponent m = 8.

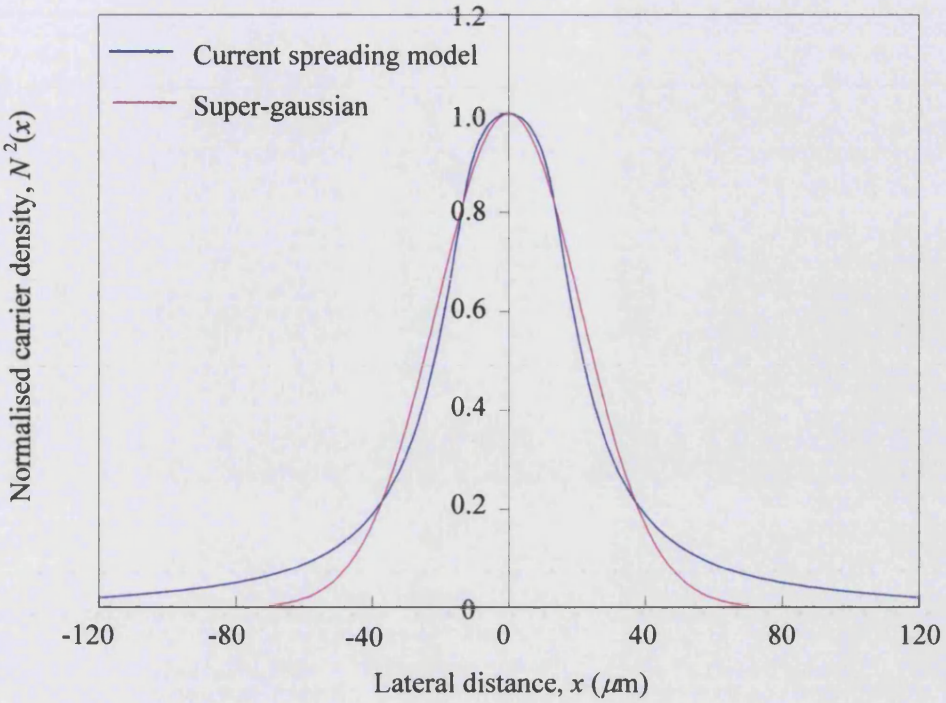

Figure 6.6: Comparison of the calculated carrier profiles of TSLD UB1037Y at the narrow end of the Taper. W_{min} = 3μm wide. Super-gaussian exponent m = 12.

6.4 Comparison between the Uniform and Non-Uniform N Method

Comparisons of the near and far-field profiles obtained by the two methods assuming uniform and non-uniform carrier (N) distribution are presented in this section. Comparisons were made for parallel stripe and taper SLDs.

6.4.1 Near-Field Profiles

Figures 6.7 and 6.8, shows the calculated near-field profiles of a parallel stripe and a taper SLD respectively. In the case of the parallel stripe SLD the calculated near–field profile from the uniform N method is square very much unlike the experimental profile. While for the taper SLD the near-field profile is parabolic. In contrast, simulation results from the non-uniform N method, offers a more realistic representation of the near-field profiles, comparable to some of the near-field profiles presented in Chapter 4.

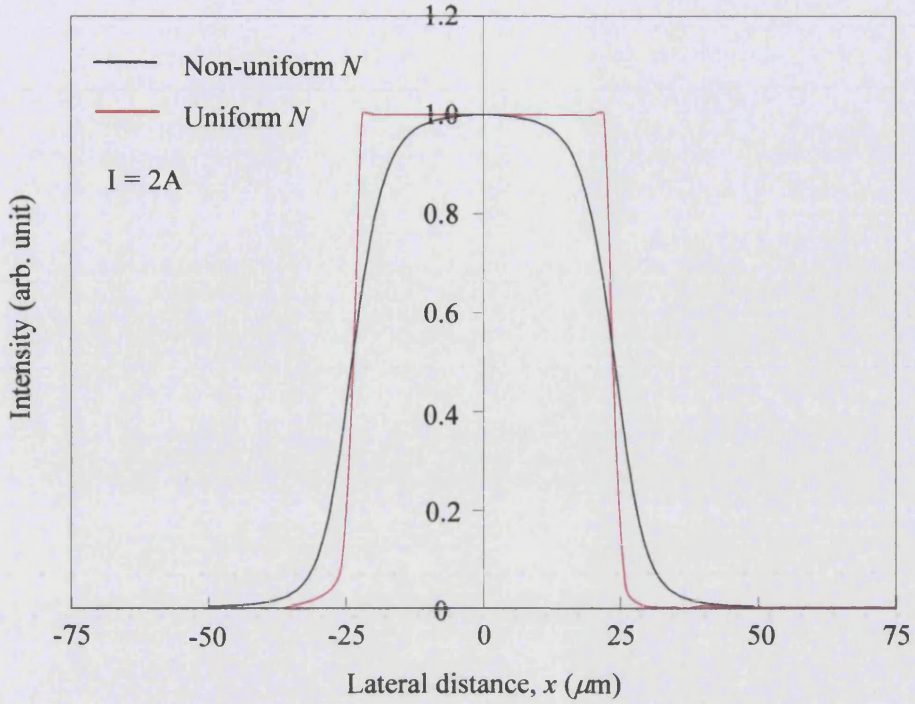

Figure 6.7: Comparison of the calculated near-field profile obtained by the two methods (unifrom and non-unifrom *N*) for a parallel stripe SLD. $W = 50\mu m$ and $L_c = 1000\mu m$.

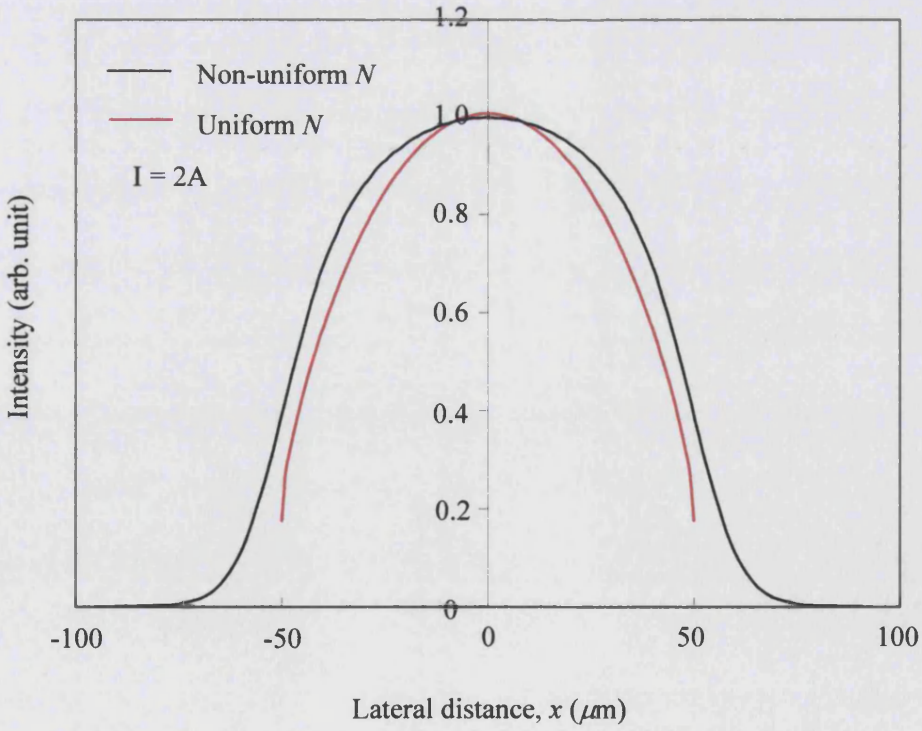

Figure 6.8: Comparison of the calculated near-field profile obtained by the two methods (unifrom and non-unifrom *N*) for a taper SLD. $W_{max} = 100\mu m$ and $L_c = 1000\mu m$.

6.4.2 Far-Field Profiles

Figures 6.9 and 6.10, shows calculated far field profiles of parallel and taper SLD. It can clearly be seen that the far-field profiles from the uniform *N* method for parallel stripe SLD is triangular in shape. Conversely the far-field profiles of the taper SLD is almost square. In contrast, the far-field profiles obtained from the uniform *N* method have a much more rounded top and hence matches better with experimental results.

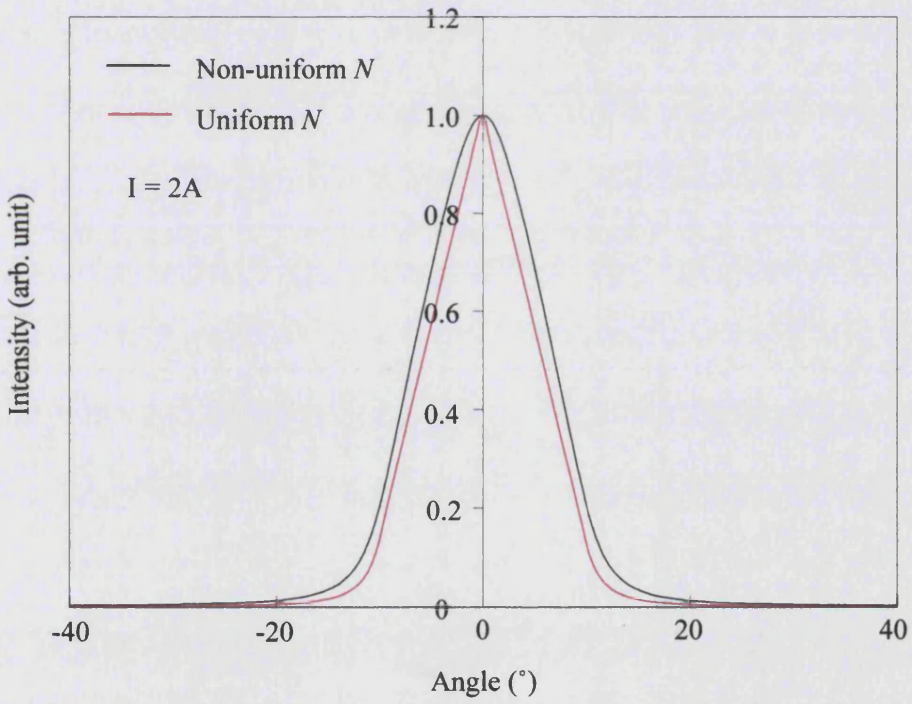

Figure 6.9: Comparison of the calculated far-field profile obtained by the two methods (unifrom and non-unifrom *N*) for a parallel stripe SLD. $W = 50\mu m$ and $L_c = 1000\mu m$.

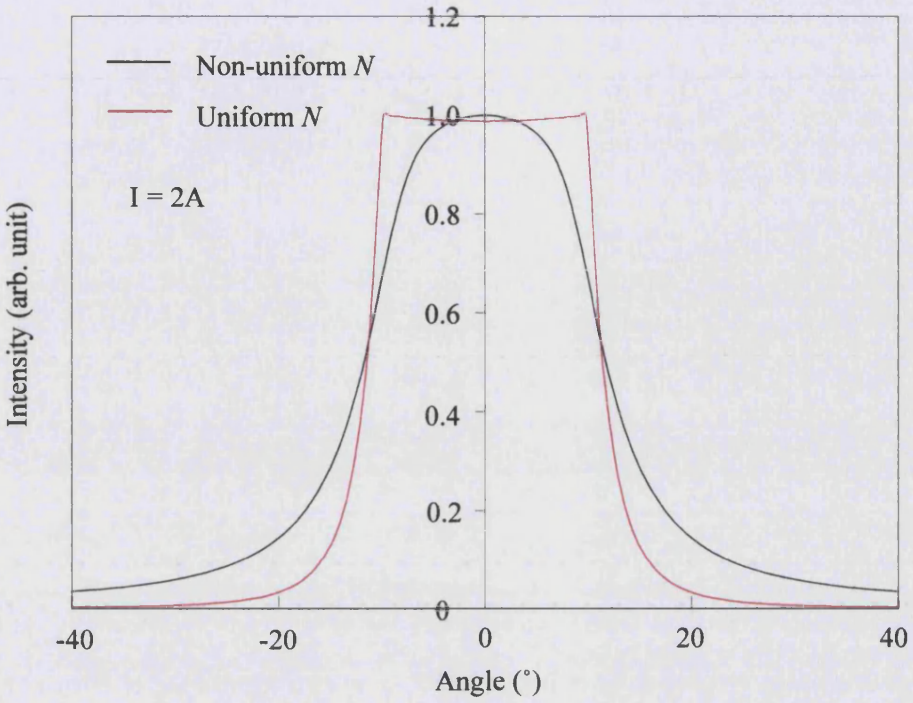

Figure 6.10: Comparison of the calculated far-field profile obtained by the two methods (unifrom and non-unifrom *N*) for a taper SLD. W_{max} = 100μm and L_c = 1000μm.

6.5 Comparison between Experimental and Theoretical Results

The experimental results of the near and far-field profiles of parallel stripe, tapered and angled tapered SLDs are compared with those predicted by the comprehensive non-uniform *N* ray model. Table 6.1 contains details of the measured devices.

Device	UB1027	UB1038Y	UB764	UB765
Device type	PSLD	TSLD	ATSLD	ATSLD
Angle of inclination, α	0°	0°	5°	10°
Output facet width, (μm)	50	100	100	100
Contact length, (μm)	1000	1000	1000	1000

Table 6.1: Details of devices measured and used in this section.

6.5.1 Near-Field Profiles

Figures 6.11 and 6.12, shows measured near-field profiles of a parallel stripe SLD (UB1027) and a taper SLD (UB1038Y) along with curves calculated by the model. Excellent agreement can be seen between the experimentally measured near-field profiles and those predicted by the model. Figure 6.13 and 6.124 show similar results for ATSLD (UB764) with $\alpha = 5^{\circ}$, measured at low and high currents using small and large NA lens. At low currents, there is no significant difference in the near-field profiles measured with either small or large NA lens. However at high currents the asymmetry becomes more accentuated. In both cases the profiles produced by the model are shown to match quite well with the experimental profiles.

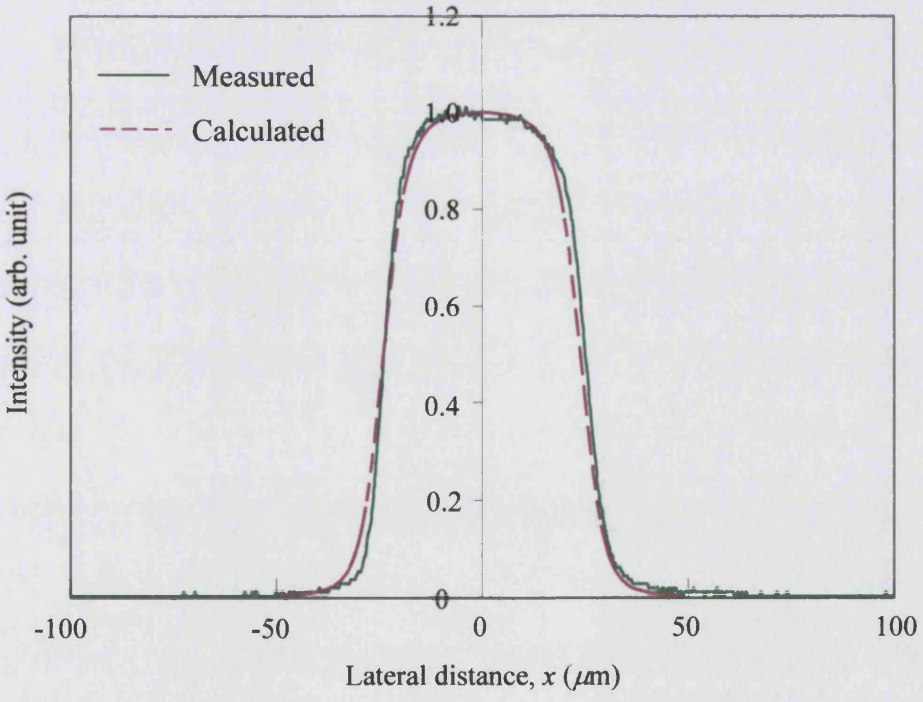

Figure 6.11: Measured and calculated near-field profiles of UB1027 Parallel Stripe SLD at 2A.

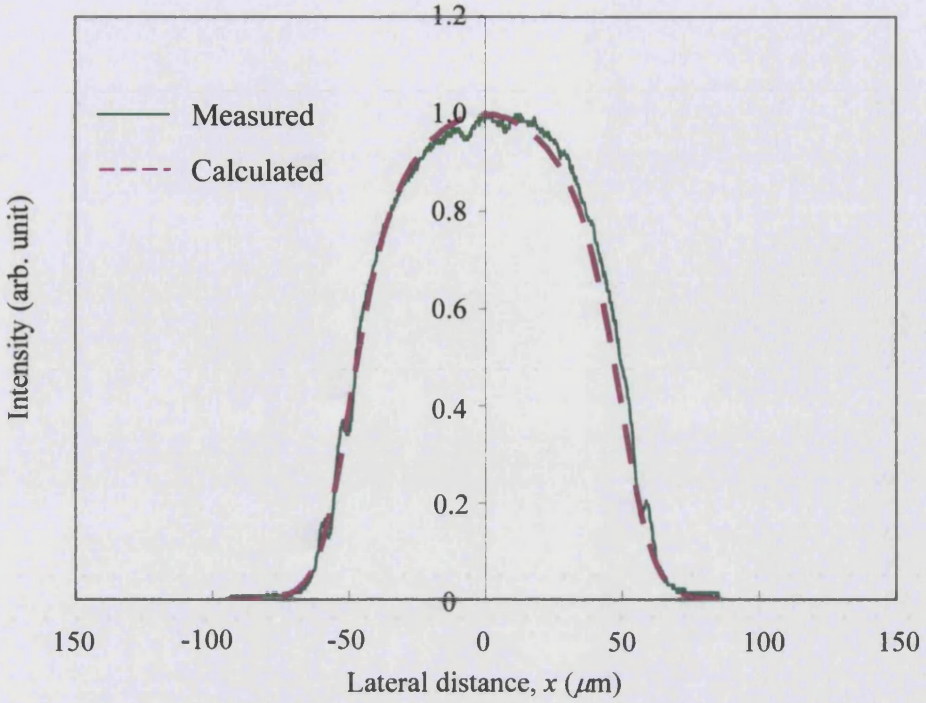

Figure 6.12: Measured and calculated near-field profiles of UB1038Y Taper SLD at 2A.

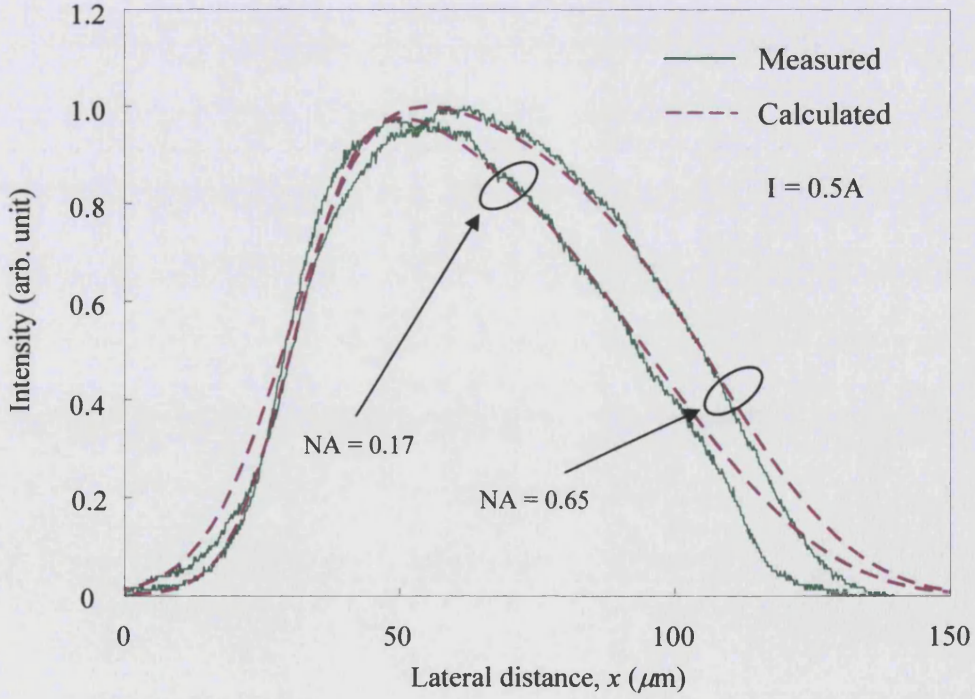

Figure 6.13: Measured and calculated near-field profiles of UB764 ($\alpha = 5^{\circ}$) ATSLD at 0.5A.

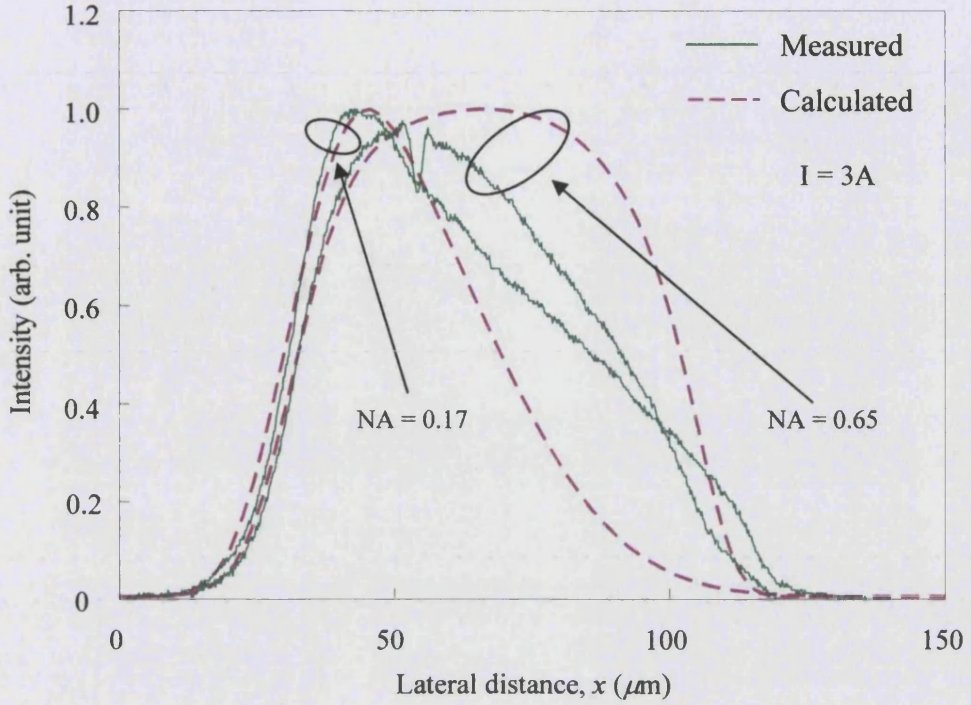

Figure 6.14: Measured and calculated near-field profiles of UB764 ($\alpha = 5°$) ATSLD at 3A.

6.5.2 Far-Field Profiles

Figures 6.15, 6.16 and 6.17 shows measured far-field profiles of parallel, taper and angled taper SLDs at several currents along with curves calculated by the model. Reasonable agreement between experiment and theory can be seen for the parallel stripe SLD. However it can be seen from Figure 6.13 that the experimentally measured far-field profiles of the taper SLD do not match very well with the theoretical profiles especially at high currents. In the case of the ATSLDs, although the peak of the far-field profiles predicted by the model match with the experimental profiles, they are however much broader than the later.

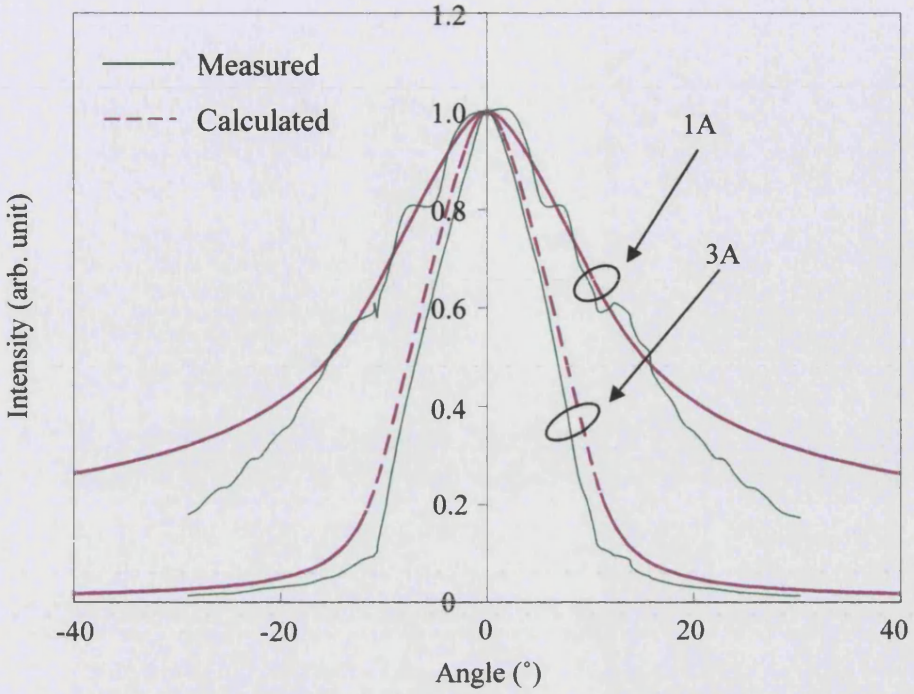

Figure 6.15: Measured and calculated far-field profiles of UB1027 PSLD at 1A and 3A.

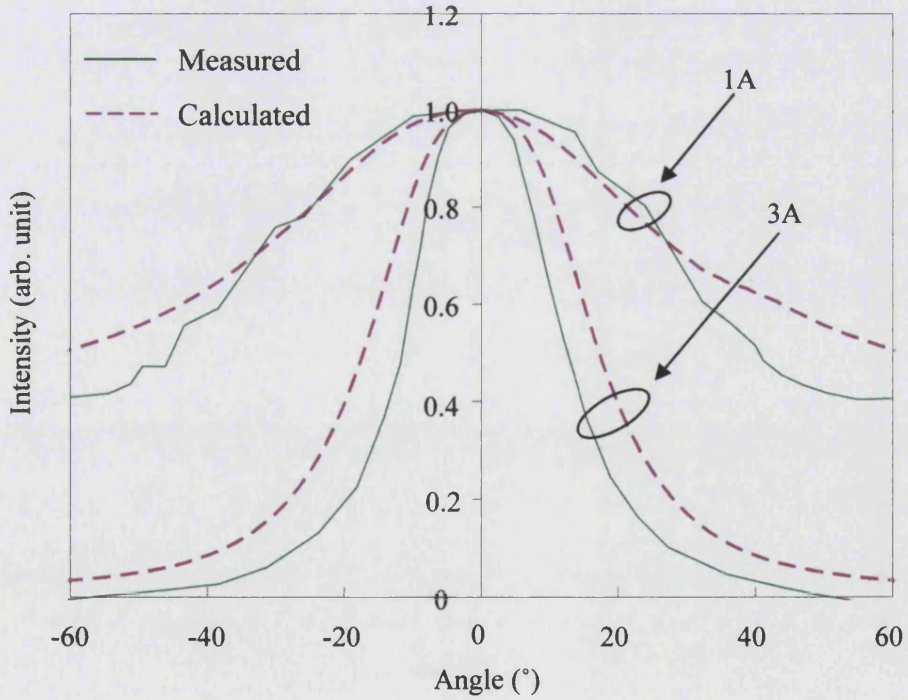

Figure 6.16: Measured and calculated far-field profiles of UB1038Y SLD at 1A and 3A.

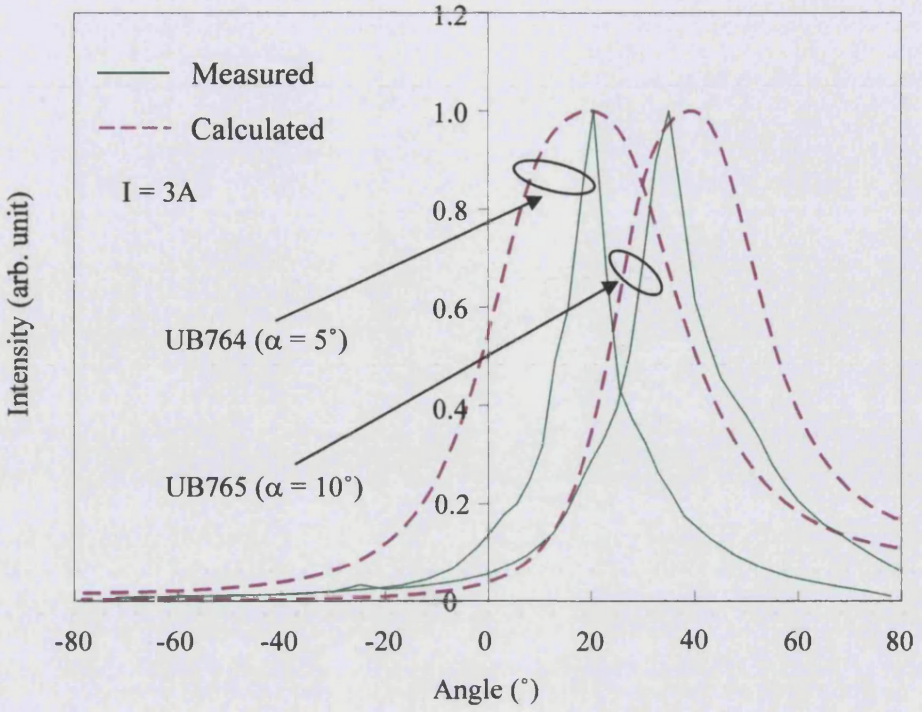

Figure 6.17: Measured and calculated far-field profiles of ATSLDs UB764 and UB765 at 3A.

6.6 Conclusions

A comprehensive ray model that provides a convenient straight- forward method for modelling near and far-field profiles of parallel stripe, tapered contact SLDs and angled contact SLDs has been developed. In-situ measured parameters have also been included in the model to produce a realistic representation of the carrier density distribution in these devices. Curve-fitting the carrier density distribution parametrically at each point along the length of the device using the super-gaussian function has simplified the computational scheme.

The near and far-field profiles of PSLDs, TSLDs and ATSLDs at low currents are shown to match quite well with those predicted by the model. However the experimentally measured far-field profiles, particularly of tapered SLDs at high currents, do not match closely with the theoretical results. This could be due to the fact that the model does not include hole-burning effect that is known to occur at high levels of pumping. Also, at high currents, due to the presence of stimulated emission, the devices are probably behaving like a partially coherent source. More specifically, an increase in the spatial coherence of the SLDs. Hence, the spatial coherence of the SLDs could be measured at several currents to investigate if increases in spatial coherence occur with increase in current.

References

[1] *G. H. B. Thompson*, **'Physics of Semiconductor Devices'**, John Wiley and Sons, Great Britain, p305, 1980.

[2] *T. Kambayashi, J.Sarma*, **'Spontaneous Emission Noise Distribution from a Gain-Guided Multimode Waveguide'**, IEEE J. Quantum Electronics, Vol. QE-19, No. 6, pp. 1084-1091, June 1983.

Chapter 7
Conclusions and Further Work

7.1 Conclusions

A model for edge-emitting parallel stripe SLDs (PSLDs) which incorporates hole burning effects has been developed to arrive at design considerations for high power tapered geometry superluminescent diodes. A number of parallel stripe SLDs with zero back facet reflectivity and finite front facet reflectivity has been analysed. The model showed that SLDs with finite front facet reflectivity suffer form severe carrier depletion at the rear end of the device. This resulted in the reduction of gain and consequently the output power. The model also showed that this problem (carrier depletion) is easily overcome by reducing the front facet reflectivity, i.e. applying anti-reflection (A-R) coating. As much as four times increase in output power from a PSLD with a single layer of A-R coating has been measured. Therefore to obtain high output powers from SLDs it is essential to reduce both facet reflectivities (front and back).

A number of tapered geometry SLDs (TSLDs) have been fabricated incorporating a two dimensional etched deflector in the absorbing region. The importance of the etched deflector has been demonstrated. TSLDs with etched back deflectors showed no lasing characteristics even at high levels of pumping. In contrast devices without etched deflectors reached lasing threshold. In addition a TSLD with a combination of A-R coating on the front facet and an etched deflector produced over 500mW quasi CW of output power. The effects of changes to the taper flare angle have also been examined. It was found that TSLD taper flare angles can be designed to give small or large output powers and also narrow or broad far-field profiles. Experimental results showed that TSLDs with small taper flare angles yields

relatively less power but gives narrow far-field profiles and hence are more suitable for fibre coupling applications. In comparison to PSLDs the TSLDs have been shown to be less susceptible to power saturation especially at high levels of pumping.

The research work has also been extended to study other methods of reducing the front facet reflectivity (i.e. apart from using high quality A-R coating). The angular displacement of the tapered contact has demonstrated to be an efficient method of reducing unwanted feedback into the active region. Experimental results showed that an angled TSLD (ATSLD) yielded output powers comparable to a similar A-R coated (R~2%) TSLD. Disconcertingly, asymmetric near-field profiles from ATSLDs when measured with small NA lens have been observed. The ray model developed has demonstrated that the observed asymmetry is due to the discriminating effect of the gain and the use of the small NA lens. Comparisons with the simulation results show good agreement between model and experiment for several devices measured with different NA lens at various levels of currents. Furthermore the spectrally resolved near-field measurements performed on ATSLDs later confirmed the theoretical findings.

A comprehensive ray model able to predict near and far-field profiles of parallel stripe, tapered contact SLDs and angled contact TSLDs has been developed. The model includes in-situ measured parameters, which produced a realistic representation of the carrier density distribution in these devices. Also, the computational scheme for the model has been made simple by using the super-gaussian function to represent the carrier density profiles. Comparisons of the near-field and far-field profiles of PSLDs, TSLDs and ATSLDs at moderate currents between experiment and those predicted by the model show excellent agreement. However measured far-field profiles of TSLDs at high currents are narrower than the simulated profile. The reasons for this are as yet unclear but could be due to phase effects seen in the measured profile that the model does not take into account.

7.2 Future Work

The work contained in this thesis has shown that tapered geometry SLDs produce high output powers. It was shown in chapter 3 that SLDs with finite front facet reflectivity suffer from severe carrier depletion at the rear of the device which reduces gain in the region. Hence A-R coatings have been used on the front facet to reduce the power density occurring in the narrow region. However, improving the L-I slope efficiencies by longitudinally varying the current density remains to be investigated. Based on a similar work [1], it may be possible to increase the output power from TSLDs, especially at high currents simply by pumping more current in the narrow taper region.

The research work has also shown that different width of far-field profiles are obtained by varying the taper flare angles. Real lateral refractive index guided TSLDs with various taper flare angles should be investigated and compared with non index guided TSLDs in order to establish if improvements in efficiency or beam quality can be obtained. In addition, the coupling efficiencies of index guided TSLDs to multimode and single mode fibres could be investigated.

In Chapter 6 the experimental result presented showed that the far-field profiles of TSLDs at high currents are much narrower than those predicted by the comprehensive ray model. This is believed to be due to phase effects, i.e. an increase in the spatial coherence of the SLD. However this hypothesis has not been verified in this research work. Hence, it would be useful to measure the spatial coherence of these devices. The spatial coherence of SLDs is of considerable interest for use in application such as optical coherence tomography.

The classical way of determining spatial coherence is the Young's double slit experiment, [2]. The drawback with this method is that the use of diffracted light prohibits its use at areas where the power is low. Furthermore, for each data point measured, a new pair of apertures has to be inserted and aligned. Recently, a method based on a fibre optic interferometer has been proposed and used to measure spatial

coherence and modal structures of HeNe lasers and laser diodes [3], [4]. This method has the advantage that light from any two arbitrary positions within the beam can be sampled and superimposed, allowing the recording of the spatial coherence function across the whole beam with high transversal resolution. Furthermore, since the sampled light is not diffracted over a large area but directly coupled into the fibre, low intensity points far away from the beam centre can also be sampled.

References

[1] *Y. Liu, Kun Liu, J. Song, Y. Chang, B. Kang, J. Yin, G. Du*, '**1.3μm Integrated Superluminescent Light Source**', Optical Materials, No. 14, pp. 235 – 238, 2000.

[2] *M. Born and E. Wolf*, '**Principles of Optics**', 6th Edition, Oxford Pergamon Press.

[3] *B. L Anderson and P. L. Fuhr*, '**Twin-Fibre Interferometric Method for Measuring Spatial Coherence**', Optical Engineering, Vol. 32, No. 5, pp. 926 – 932, 1993.

[4] *L. J. Pelz and B. L. Anderson*, '**Practical use of the Spatial Function for Determining Laser Transverse Mode Structure**', Optical Engineering, Vol. 34, No. 11, pp. 3323 – 3328, 1995.

Appendix 1A

Derivation of Current Density Conservation Equation

In this appendix the current density conservation equation is derived, which gives the relationship between inversion population N and current density J. First consider the device structure shown in Figure A1.1.

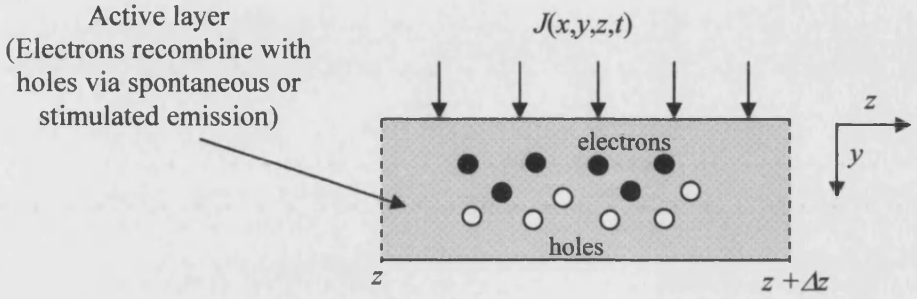

Figure A1.1: Schematic diagram illustrating the flow of current into the active layer and the recombination of electron and holes in the active layer.

In the derivation the current density is assumed to be constant throughout the rectangular striped region. This amounts to neglecting current spreading and carrier diffusion. It is also assumed that the current density is evenly distributed throughout the active layer thickness so that $J = J_0$. The number of particles entering and leaving this volume $V = \Delta x, \Delta y, \Delta z$ in time Δt is:

Entering $$\frac{J(x,y,z,t)}{q} = .\Delta x.\Delta y.\Delta z.\Delta t \qquad \text{(A1.1)}$$

Leaving $$\frac{J(x,y-\Delta y,z,t)}{q} = .\Delta x.\Delta z.\Delta t \qquad \text{(A1.2)}$$

where q is the electron charge. Hence the change net number of particles in the volume in time Δt is :-

$$\frac{1}{q}\left[J(x,y,z,t) - J(x,y-\Delta y,z,t)\right].\Delta x.\Delta z.\Delta t \qquad \text{(A1.3)}$$

The increase of carriers in this volume in time Δt by definition is:-

$$[N(x,y,z,t+\Delta t) - N(x,y,z,t)].\ \Delta x.\ \Delta y.\ \Delta z \tag{A1.4}$$

However, the depletion of carriers because of recombination due to spontaneous and stimulated emission must be taken into account.

The total number of particles recombining in time Δt via spontaneous and stimulated emission is:-

Spontaneous emission: $$\frac{N}{\tau_{sp}}.\Delta x,\Delta y,\Delta z,\Delta t \tag{A1.5}$$

Stimulated emission: $$\tilde{g}(N)[P+Q].\Delta x.\Delta y.\Delta z.\Delta t \tag{A1.6}$$

where $\tilde{g}(N)$ is the material gain in units of time^{-1} and P and Q represent the photon density of forward and reverse traveling photons respectively.

Thus it can be said that the increase in carriers in the active layer after a time Δt is equal to the net numbers of particles in the volume minus the total number of particles recombining via spontaneous and stimulate emission. This can be written as:

$$[N(x,y,z,t+\Delta t) - N(x,y,z,t)].\ \Delta x.\ \Delta y.\ \Delta z = \frac{1}{q}[J(x,y,z,t) - J(x,y-\Delta y,z,t)].\ \Delta x.\ \Delta z.\ \Delta t$$

$$-\left[\tilde{g}(N)(P+Q)+\frac{N}{\tau_{sp}}\right].\Delta x.\Delta y.\Delta z.\Delta t. \tag{A1.7}$$

Dividing equation (A1.7) through Δx, Δy, Δz, Δt and taking the limit $\Delta y \rightarrow 0$ and $\Delta t \rightarrow 0$ gives the differential current density conservation equation, which takes the form:

$$\frac{dN}{dt}=\frac{1}{q}\frac{dJ_0}{dy}-\left[\tilde{g}(N)\{P+Q\}+\frac{N}{\tau_{sp}}\right] \tag{A1.8}$$

The steady state solution to equation (A1.8) is:

$$\frac{J_0}{qd}=\tilde{g}(N)[P+Q]+\frac{N}{\tau_{sp}} \tag{A1.9}$$

Appendix 2A

Material Parameters

2A.1 Materials Used

Two different materials have been used in this research work. The wafer structure of these materials are given below

2A.1.1 Material QT543R

Layer	Thickness (μm)	Composition	Doping Density (cm^{-3})	Doping Type	Dopant
Contact	0.3	GaAs	8.0×10^{18}	p^+	Zn
Cladding	1.6	$Al_{0.36}Ga_{0.64}As$	7.5×10^{17}	p^-	C
Cladding	0.4	$Al_{0.36}Ga_{0.64}As$	Undoped	--	--
Active	0.17	GaAs	Undoped	--	--
Cladding	2.0	$Al_{0.36}Ga_{0.64}As$	7.5×10^{17}	n^-	Si
Buffer	0.1	GaAs	1.2×10^{18}	n^+	Si
Substrate	---	GaAs	----------	n^+	--

2A.1.2 Material QT503A

Layer	Thickness (μm)	Composition	Doping Density (cm^{-3})	Doping Type	Dopant
Contact	0.25	GaAs	1.1×10^{19}	p^+	Zn
Cladding	1.50	$Al_{0.33}Ga_{0.67}As$	9.0×10^{17}	p^-	C
Active	0.35	$Al_{0.02}Ga_{0.98}As$	Undoped	--	--
Cladding	3.00	$Al_{0.33}Ga_{0.67}As$	3.0×10^{17}	n^-	Si
Buffer	0.10	GaAs	1.0×10^{18}	n^+	Si
Substrate	---	GaAs		n^+	--

Appendix 3A

Constant Carrier Analysis for Rate Equations

In this appendix the analytic solution to the rate equations using the constant carrier density analysis is derived. First consider the device structure shown in Figure A3.1.

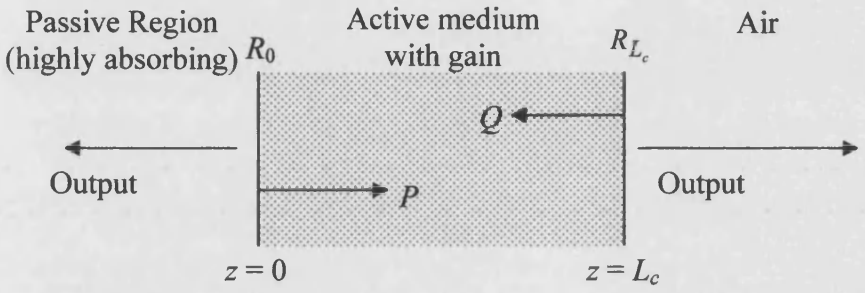

Figure A3.1: Schematic diagram illustrating the device structure.

The longitudinal (z) spatial variation of photons and carriers in the active medium is obtained by solving the photon rate equations, which takes the form:

$$\frac{dP}{dz} = \frac{\tilde{g}(N)}{\upsilon} \cdot P + \frac{\delta_f}{\upsilon} \cdot \frac{N}{\tau_{sp}} \tag{A3.1}$$

$$\frac{dQ}{dz} = -\frac{\tilde{g}(N)}{\upsilon} \cdot Q - \frac{\delta_r}{\upsilon} \cdot \frac{N}{\tau_{sp}} \tag{A3.2}$$

where N is the carrier density, P represents forward travelling photons, Q represents reverse travelling photons, N is the carrier density distribution, τ_{sp} is the spontaneous emission recombination lifetime, υ is the velocity in the media, $\delta_{f/r}$ is the fraction of spontaneous emission contributing towards the forward and reverse travelling photons, and $\tilde{g}(N)$ is the material gain given by:

$$\tilde{g}(N) = \Gamma_v . \alpha_0 (N - N_T) \tag{A3.3}$$

where α_0 is the gain coefficient, Γ_v is the optical field confinement factor in the vertical direction and N_T is the carrier density at transparency. It is assumed that spontaneous emission is radiated isotropically, such that the fraction

$$\delta_{f/r} = \frac{2\phi_c d\theta}{4\pi} \tag{A3.4}$$

is directed into the angular range $2\phi_c$ in the direction perpendicular to the junction (y direction), Figure A3.2a, and into the angular range $d\theta$ in the plane of the junction, Figure A3.2b. ϕ_c is the critical angle for total internal reflection given by:

$$\phi_c = \cos^{-1}(\frac{n_2}{n_1}) \tag{A3.5}$$

where n_1 and n_2 are the refractive indices of the active and cladding layers respectively.

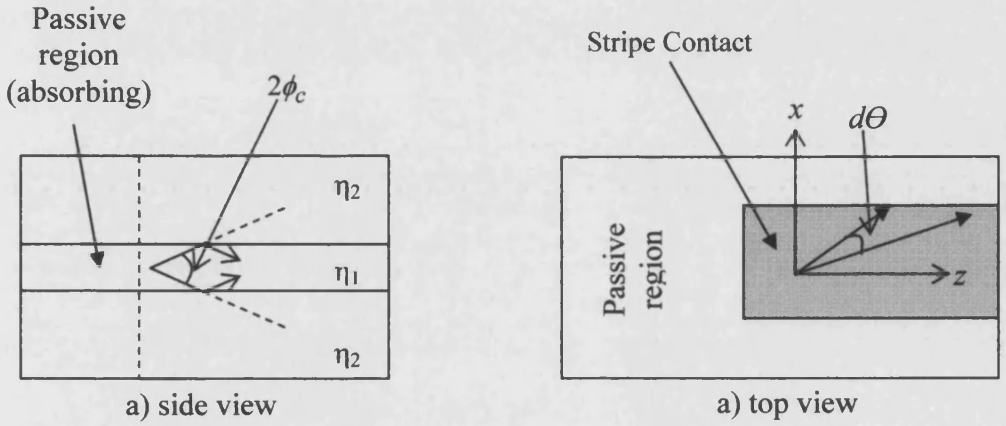

Figure A3.2: Schematic of an SLD: a) side view, b) top view. η_1 and η_2 are refractive index of the active and cladding layer respectively.

Assuming that the carrier density, N, is a constant $N = \overline{N}$, equations (A3.1), (A3.2) can be rewritten as:

$$\frac{dP}{dz} = \bar{g}\left[P + \bar{P}_{sp}\right] \qquad P = P(z) \tag{A3.6}$$

$$\frac{dQ}{dz} = -\bar{g}[Q + \bar{Q}_{sp}] \qquad Q = Q(z) \tag{A3.7}$$

where $$\bar{g} = \frac{\tilde{g}(\overline{N})}{\upsilon}$$

and $$\bar{p}_{sp} = \frac{\delta_f}{\upsilon\bar{g}} \cdot \frac{\overline{N}}{\tau_{sp}} \tag{A3.8}$$

$$\bar{Q}_{sp} = \frac{\delta_r}{\upsilon\bar{g}} \cdot \frac{\overline{N}}{\tau_{sp}} \tag{A3.9}$$

The photon rate equations in the form given in equation (A3.6) and (A3.7) have an analytic solution. However the photon rate equations are also coupled via the charge conservation equation, represented by:

$$\frac{J_0}{qd}=\tilde{g}(\overline{N})[P(z,\overline{N})+Q(z,\overline{N})]+\frac{\overline{N}}{\tau_{sp}} \tag{A3.10}$$

where q is the electronic charge and d is the active layer thickness. The injected current density J, is assumed to be constant along the length such that $J=J_0$. Assuming that the analytic solution to the photon rate equations are known, $P(z,\overline{N})$ and $Q(z,\overline{N})$, the charge conservation equation can be rewritten as:

$$\frac{J_0}{qd}=\tilde{g}(\overline{N})[P(z,\overline{N})+Q(z,\overline{N})]+\frac{\overline{N}}{\tau_{sp}} \tag{A3.11}$$

Equation (A3.11) can only be satisfied if $P(z,\overline{N})$ and $Q(z,\overline{N})$ are constant along the length. In general the photon density distribution is not constant along the length. Therefore equation (A3.11) is integrated over the length L_c, to give:

$$\frac{J_0}{qd}=\tilde{g}(\overline{N})[\overline{P}(\overline{N})+\overline{Q}(\overline{N})]+\frac{\overline{N}}{\tau_{sp}} \tag{A3.12}$$

where $$\overline{P}(\overline{N})=\frac{1}{L_c}\int_0^{L_c}P(z,\overline{N})dz \tag{A3.13}$$

$$\overline{Q}(\overline{N})=\frac{1}{L_c}\int_0^{L_c}Q(z,\overline{N})dz \tag{A3.14}$$

With reference to Figure A3.1 the photon densities P and Q must also satisfy the boundary conditions at z = 0 and z = L_c. The boundary condition states that

$$P(z=0)=P_I+R_0Q(z=0)=P_I+R_0Q_0 \tag{A3.15}$$

$$Q(z=L_c)=Q_{L_c}=R_{L_c}P(z=L_c)=R_{L_c}P_{L_c} \tag{A3.16}$$

where R_0 and R_{L_c} are facet reflectivities at $z = 0$ and $z = L_c$ respectively and P_I is the initial photon density value assumed to be 1. The analytic solution to the photon rate equations (A3.6) and (A3.7) takes the form:

$$P(z,\overline{N})=P_0G_{L_c}+[G_{L_c}-1]\overline{P}_{sp} \tag{A3.17}$$

$$Q(z,\overline{N})=Q_0G_{L_c}+[G_{L_c}-1]\overline{Q}_{sp} \tag{A3.18}$$

$$G_{L_c} = \exp(\bar{g}z)$$

where P_0 and Q_0 are constant associated to the spontaneous emission at $z = 0$. Imposing the boundary conditions on equation (A3.8) and (A3.9), we obtain the expressions for P_0 and Q_0.

$$P_0 = \frac{1}{1 - R_0 R_L G_L{}^2}\left[P_I + R_0(G_L - 1)\overline{Q}_{sp} + R_0 R_L G_L(G_L - 1)\overline{P}_{sp}\right] \quad \text{(A3.19)}$$

$$Q_0 = R_L G_L{}^2 P_0 + R_L G_L(G_L - 1)\overline{P}_{sp} + (G_L - 1)\overline{Q}_{sp} \quad \text{(A3.20)}$$

Appendix 3B

Experimental Setup for Different Measurements

3B.1 Light-Current (L-I) and Polarisation Measurement

The most commonly used method for measuring the total light power emitted from an SLD is to place a photodiode close to the SLD to ensure large collection angle. The SLD is mounted on precision '*x*, *y* and *z* movements' to allow accurate position and focusing. The SLD is placed at a distance of about 2mm from a 15mm area photodiode, which gives a collection angle of about 75° in the lateral direction. The experimental apparatus for the measurement of the L–I characteristics is shown in Figure 3B.1. The current through the device is monitored using a current probe connected to an oscilloscope. The output signal from the photodiode is terminated in 50Ω at the oscilloscope and can be related to the optical power assuming that the responsitivity is known for the wavelength being measured.

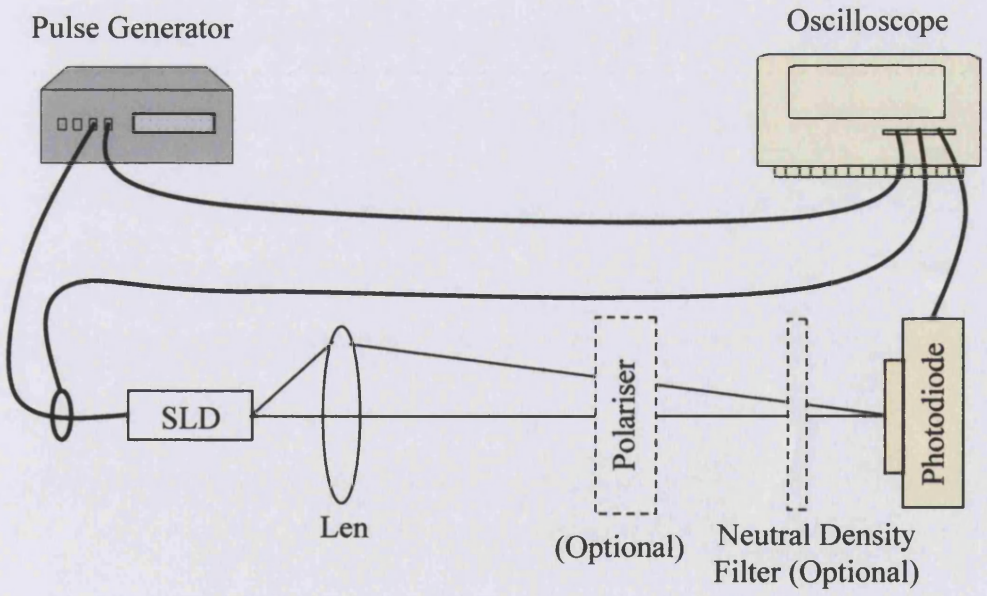

Figure 3B.1 Diagram of apparatus used to measure output power and polarisation of a SLD.

However, at high currents, i.e. when output power from the SLD is too large, the photodiode saturates. In this case a Neutral Density Filter is needed to measure the output power from the SLD. A Neutral Density Filter is used because it attenuates the optical signal evenly over the whole wavelength range of interest. The filter is introduced between the SLD and the photodiode, as show in Figure 3B.1. Here a lens is used to collect the diverging light form the SLD, which then focuses it down to a spot at the detector. Note, the overall attenuation of the lens/filter system must be measured for each SLD in order to correctly evaluate the laser output power. Ideally, two lenses should be employed such that the beam passing through the filter is collimated. However, if the distance between the lens and photodiode is sufficiently large then the beam will be nearly collimated and this is then unnecessary.

To obtain the degree of polarisation (DOP) of a SLD, it is necessary to measure the L-I characteristics of both the TE and TM polarisations. In this case a polariser is placed in front of the photodiode after the lens, as shown in Figure 3B.1. The polariser is first calibrated with a laser diode by allowing light to pass through, which is TE polarised. This is to determine the position of the polariser for the TE transmission. The position of the polariser for the TM transmission is at right angles to this.

3B.2 Near – Field Intensity Distribution Measurement

The experimental apparatus for the measurement of the near field profile is shown in Figure 3B.2. In the experiment a lens is used to form an image of the laser facet at the camera, which is then recorded and stored in a computer. When the intensity becomes too high and the camera saturates the Neutral Density Filter is once again used to attenuate the optical signal.

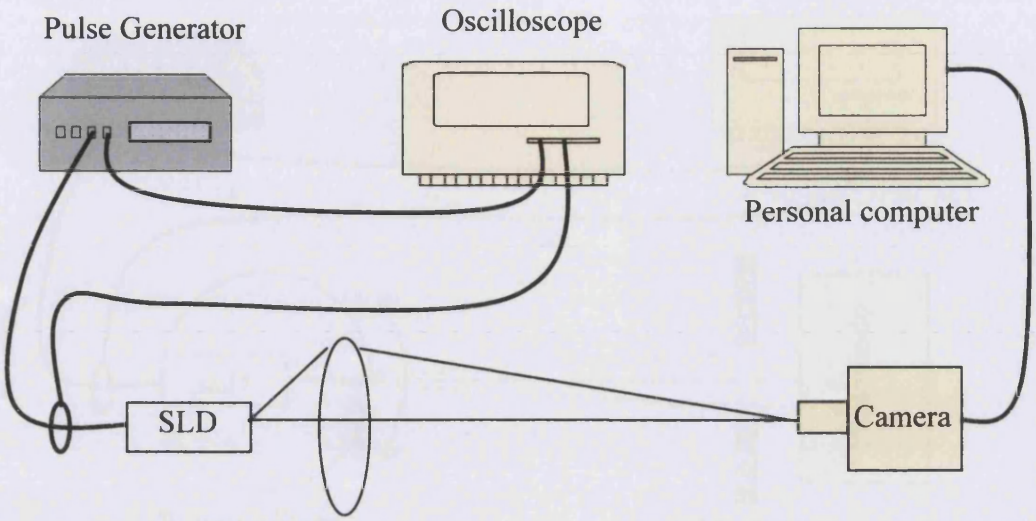

Figure 3B.2: Diagram of apparatus used to measure the near-field intensity profile of a SLD.

3B.3 Far-Field Intensity Distribution Measurement

The apparatus used to measure the far-field intensity distribution of the SLD is illustrated in Figure 3B.3. In this measurement the SLD is mounted onto a rotary stage in order to measure the angular spread of the output field. The photodiode is placed some distance away form the device with an aperture slit positioned close to the photodiode. A 0.5mm wide aperture slit was used and the distance between the device and the aperture slit was kept to about 70mm, which subtends an angle of less than 0.5°. The angular resolution of the measurement is set either by the smallest division on the rotating stage or by the width of the aperture and its distance from the SLD facet. The smallest division on the rotating stage used in this work was 0.5° hence in this case the angular resolution is set by the rotating stage.

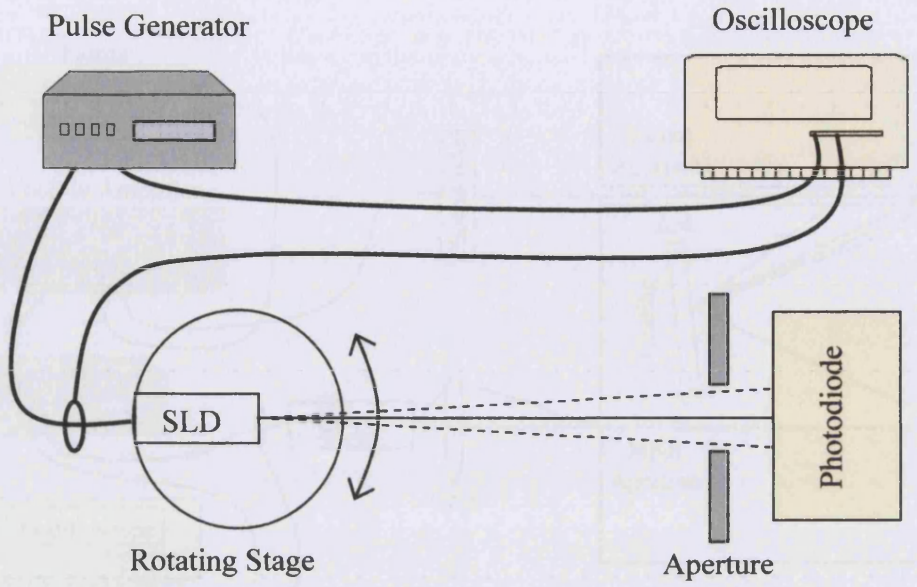

Figure 3B.3: Diagram of apparatus used to measure the far-field intensity profile of a SLD.

3B.4 Spectral Measurement

Figure 3B.4 show the experimental apparatus used to measure the spectral distribution of a device. The light output is focussed onto the input aperture of the monochromator. The transmitted beam is then reflected by the curve mirror onto a planar reflection grating. This grating is angled such that the first order diffraction peak is incident on a further curved mirror and reflected onto the output aperture. Any optical power transmitted through this aperture is then collected and measured on a photodiode. Since different wavelengths are diffracted by different amounts hence the output aperture for a given grating angle will only transmit a small range of wavelengths. Scanning the grating through a range of angels then allows a measurement of intensity variation with wavelength to be made.

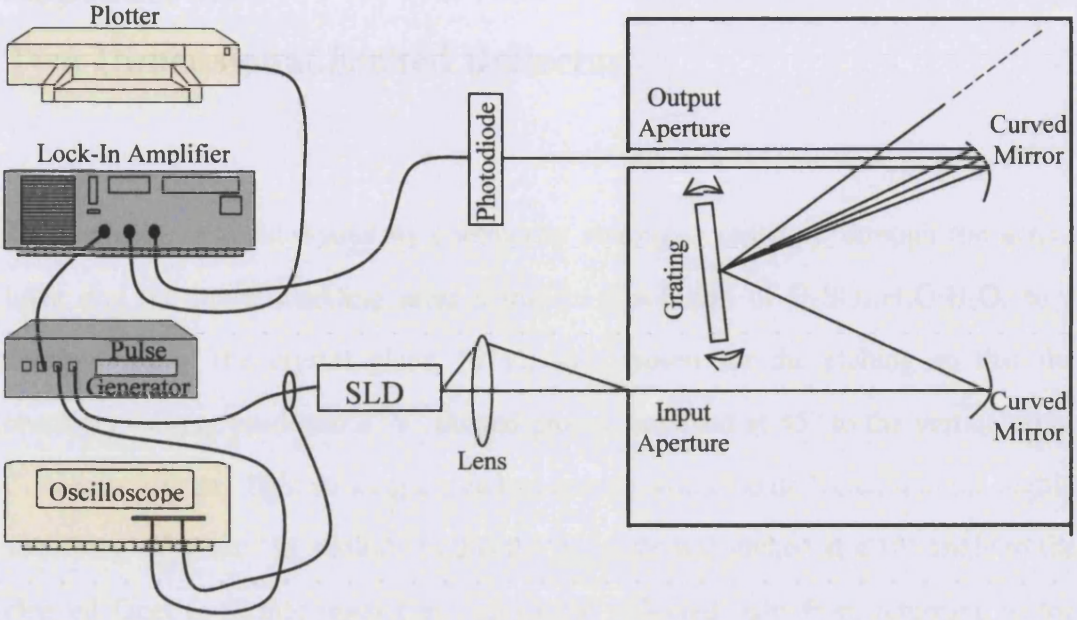

Figure 3B.4. Diagram of apparatus used to measure the output spectrum of a SLD.

In this experiment it was necessary to use a photodiode with a lock-in amplifier because very small signals were seen at the output. From figure 3B.4, the signal from the photodiode was fed into a lock-in amplifier, which was synchronised with the pulse generator driving the laser. The output signal from the lock-in amplifier was then sent to an X-Y plotter and plotted against time while the monochromator scanned the grating through a range of angles giving a plot of output power against wavelength for the device.

The resolution of the monochromator is controlled by the width of the input and output aperture slits. The maximum resolution is 0.1nm with the slits closed to less than 50nm. However, as the slits are narrowed the output is reduced until the signal becomes too noisy and therefore a compromise between resolution and signal strength is required for some low power devices.

Appendix 4A
Two Dimensional Etched Deflector

The deflector was fabricated by chemically etching completely through the active layer and the lower cladding layer using 8:1:1 solution of H_2SO_4:H_2O:H_2O_2 to a depth of 6μ. The crystal plane, (011), was chosen for the etching so that the chemical etching produced a 'V' shaped groove, inclined at 45° to the vertical axis. Consequently, any light striking the etched groove would be deflected into the highly absorbing substrate. In addition to this the deflector was etched at a 10° angle to the cleaved facet to further restrict any unwanted reflected light from returning to the gain region. The effect that etching at a 10° angle to the $(01\bar{1})$ plane had on the 'V' shaped groove wad examined with a microscope and the angle to the normal was found to be 45° for the first 2.5μm etched and 55° or the next 3.5μm.

The solutions H_2SO_4 and H_2O_2 are mixed in a running water bath at 17°C. The H_2SO_4 is slowly added to the water and reaches over 40°C very rapidly. This is allowed to cool before the peroxide is slowly added while constantly stirring. The solution is allowed to cool again before it is used for etching.

The etch rate of the solution depends on the agitation of the solution while in use. With gentle stirring the first 15 seconds produces a 0.1μm etch, slowing to a 0.3μm etch after 60 seconds at 17°C.

Appendix 5A

Spontaneous Emission Spectrum

5A.1 Measured Spontaneous Emission Curves

The measured spontaneous emission spectrum at several currents from a TSLD made form material QT543R is given below as a reference.

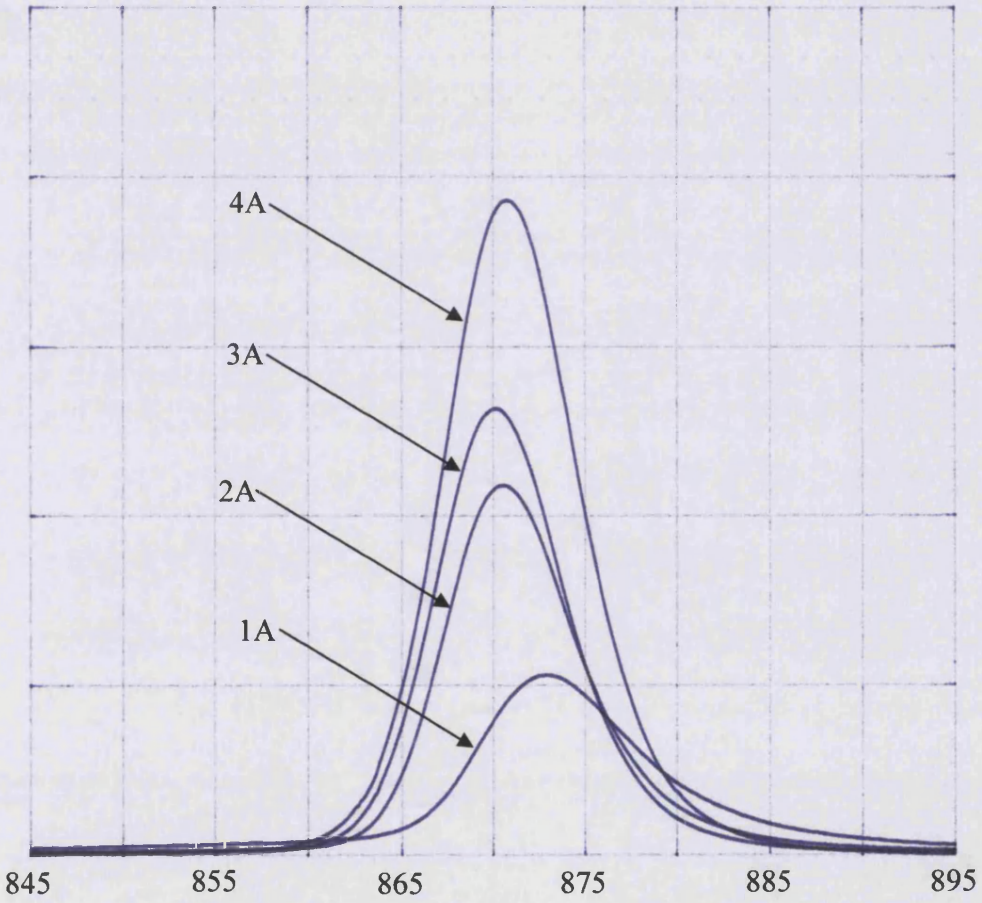

Appendix 6A

Journal and Conference Publications from Research Work

[1] *I.Middlemast, J. Sarma, S. Yunus*, **'Design and Development of High Power Tapered Superluminescent Diodes'**, Semiconductor and Integrated Optoelectronics Conference (SIOE'97), Cardiff, Wales, April 1997.

[2] *I.Middlemast, J. Sarma, S. Yunus*, **'High Power Tapered Superluminescent Diodes using Novel Etched Deflectors'**, Electronic Letters, Vol.33, No.10, pp.903-904, 1997.

[3] *S. Yunus, J. Sarma*, **'Ray Model of Angled Tapered Superluminescent Diodes'**, Photonics 1998, International Conference on Fibre Optics and Photonics, Delhi, India, December 1998.

[4] *S. Yunus, J. Sarma, F. Causa*, **'Spectrally Resolved Near-Field Intensity Distribution of Angled-Tapered-SLDs'**, Semiconductor and Integrated Optoelectronics Conference (SIOE'2000), Cardiff, Wales, April 2000.

[5] *S. Yunus, J. Sarma, F. Causa*, **'Study of Tapered Superluminescent LEDs (TSLEDs)'**, Photonics 2000, International Conference on Fibre Optics and Photonics, Calcutta, India, December 2000.

[6] *S. Yunus, F. Causa, J. Sarma*, **'Intensity Profiles of Parallel and Tapered Geometry Superluminescent Light Emitting Diodes (SLEDs)'**, Semiconductor and Integrated Optoelectronics Conference (SIOE'2001), Cardiff, Wales, April 2001.

[7] *Federica Causa, Jayanta Sarma, Sharina Yunus*, **'Characterization of Angled Tapered Superluminescent LEDs'**, Applied Optics-LP, Volume 41, Issue 24, pp. 5045-5050, August 2002